Title
Study of Instability and transition in MHD flows as applied to liquid metal blankets

Author
Vetcha, Naveen

Publication Date
2012

Peer reviewed|Thesis/dissertation

UNIVERSITY OF CALIFORNIA

Los Angeles

Study of instability and transition in MHD flows as applied to liquid metal blankets

A dissertation submitted in partial satisfaction

of the requirements for the degree

Doctor of Philosophy in Mechanical Engineering

by

Naveen Vetcha

2012

ABSTRACT OF THE DISSERTATION

Study of instability and transition in MHD flows as applied to liquid metal blankets

by

Naveen Vetcha

Doctor of Philosophy in Mechanical Engineering

University of California, Los Angeles, 2012

Professor Mohamed Abdou, Chair

In this study, flow phenomena associated with inflectional and boundary-layer instabilities, as well as a mixed instability mode are accessed with the help of a parametrical model, which describes a family of quasi-two-dimensional (Q2D) magnetohydrodynamic (MHD) flows in a rectangular duct, where the near-wall jet is produced by imposing an external flow-opposing force. By varying this force, various instability modes and transition scenarios are reproduced via changes in the basic velocity profile. First, linear stability analysis is performed and then nonlinear effects are studied using DNS for Hartmann numbers 100 and 200 and Reynolds numbers from 1800 to 5000. A special attention is paid to the location of the inflection point with respect to the duct wall. A more complex flow dynamics, including various vortex-wall and vortex-vortex interactions, and even negative turbulence production are observed and analyzed as the inflection point approaches the wall. The obtained results as well as their qualitative

comparisons with previous experimental and numerical data for the flows with the "M-shaped" velocity profile give a deeper look into what is usually called "jet instability", which, in fact, appears to be a complex integrated phenomenon that involves both linear and nonlinear mechanisms.

We also consider MHD rectangular duct flows with volumetric heating. The flows are upward, subject to a strong transverse magnetic field perpendicular to the temperature gradient, such that the flow dynamics is Q2D. The internal volumetric heating imitates conditions of a blanket of a fusion power reactor, where a buoyancy-driven flow is imposed on the forced flow. Studies of this mixed-convection flow include analysis for the basic flow, linear stability analysis and DNS-type computations. The parameter range covers the Hartmann number (*Ha*) up to 500, the Reynolds number (*Re*) from 1000 to 10,000 and the Grashof number (*Gr*) from 10^5 to 10^9. The linear stability analysis predicts two primary instability modes: (i) bulk instability associated with the inflection point in the velocity profile near the "hot" wall and (ii) side-wall boundary layer instability. A mixed instability mode is also possible. An equation for the critical Hartmann number has been obtained as a function of *Re* and *Gr*. Effects of *Ha*, *Re* and *Gr* on turbulent flows are addressed via non-linear computations that demonstrate two characteristic turbulence regimes. In the "weak" turbulence regime, the induced vortices are localized near the inflection point of the basic velocity profile, while the boundary layer at the wall parallel to the magnetic field is slightly disturbed. In the "strong" regime, the bulk vortices interact with the boundary layer causing its destabilization and formation of secondary vortices that may travel across the flow, even reaching the opposite wall. In this regime, the key phenomena are vortex-wall and various vortex-vortex interactions.

The dissertation of Naveen Vetcha is approved.

Jonathan Aurnou

Jeff Eledredge

Adrienne Lavine

Sergey Smolentsev

Mohamed Abodu, Committee Chair

University of California, Los Angeles

2012

To my parents….

without whose hard work and sacrifices

I would not have come this far

TABLE OF CONTENTS

LIST OF FIGURES

LIST OF TABLES

ACKNOWLEDGEMENTS

I would like to express my sincere gratitude to Professor Mohamed Abodu for giving me an opportunity to pursue a graduate degree at UCLA, for acting as my supervisor and providing me with financial support.

I would also like to express my gratitude to my advisor Dr. Sergey Smolentsev for his unwavering support, constant guidance, patience and encouragement during my stay at UCLA. His knowledge, work ethic and optimistic attitude toward solving complex problems has been very inspiring and has immensely helped me grow as a researcher as well as a person. Special thanks to Professor Rene Moreau for providing his insightful suggestions to improve this work.

I also want to thank Prof. Jonathan Aurnou, Prof. Jeff Eldrdge and Prof. Adrienne Lavine for serving as my doctoral committee members.

Thanks also to Dr. Ramakanth Munipalli and Dr. Peter Huang of Hypercomp Inc. for helping me in using the HIMAG solver for three dimensional numerical simulations reported in this work.

I would also like to thank my colleagues at Fusion Science and Technology Center (Dr. Karim Messadak, Dr. Alice Ying, Dr. Neil Morley, Dr. Haibo Liu, Tom Sketchley, Dr. Manmeet Narula, Dr. Junichi Takeuchi, Dr. Alberto Beltran, Dr. Ryan Hunt, Christian Di Sanzo, Alexandre Jousse, Hongjie Zhang, Jack Young, Sheida saeidi, Damien Sutevski, Aanchal Kohli, Jon Van Lew). I have enjoyed and learned a lot while working with members of my research group. A special thanks to Jack Young for proof reading this manuscript. I also appreciate all the kind help I received from the office staff: Karl Holmes, Arnaud Larousse, Allison Ross and Samantha Townsend. I have also been very fortunate to have number of close friends during my

stay in Los Angeles. I will always be indebted to friends like Arunabh, Sridhar, Albert, Maziar, David and Samir who helped me in a lot of different ways.

I wish to acknowledge that this research is supported by the US Department of Energy (DOE) and TITAN program under DOE Grant No. 00072621.

Finally, I owe everything I have achieved in life to my family. My parents always emphasized on my studies, worked tirelessly and made sacrifices to avail me the opportunities they could not have. I will forever be indebted to them for their love, support and teaching me good values in life. I am also grateful for the joy and emotional support provided by my sister Neelima, brother-in-law Nagesh and brother Prashant over the years. Finally, but most importantly, I want to thank my wife, Sindhu, for her understanding and love. Her support and encouragement was in the end what made this dissertation possible.

VITA

2005	B.E. in Mechanical Engineering Osmania University, Hyderabad, India
2005-2007	Project Assistant Dept. of Mechanical Engineering Indian Institute of Technology, Kanpur, India
2007	M.Tech. in Mechanical Engineering Indian Institute of Technology, Kanpur, India
08/2007-11/2007	Senior Project Associate Dept. of Mechanical Engineering Indian Institute of Technology, Kanpur, India
2009	M.S. in Mechanical Engineering University of California, Los Angeles
Winter-2010 Spring-2011 Winter-2012	Teaching Assistant Dept. of Mechanical and Aerospace Engineering University of California, Los Angeles
2008-Present	Graduate Student Researcher Fusion science and technology center University of California, Los Angeles

JOURNAL PUBLICATIONS

N. Vetcha, S. Smolentsev, M. Abdou, and R. Moreau, "Study of instabilities and quasi-two-dimensional turbulence in volumetrically heated MHD flows in a vertical rectangular duct," *Physics of Fluids (under consideration).*

N. Vetcha, S. Smolentsev, and M. Abdou, "Stability analysis for the Hartmann flow with interfacial slip," *Magnetohydrodynamics*, 48(1), 147 (2012).

S. Smolentsev, **N. Vetcha**, and R. Moreau, "Study of instabilities and transitions for a family of quasi-two-dimensional magnetohydrodynamic flows based on a parametrical model", *Physics of Fluids*, 24, 024101 (2012).

N. Vetcha, S. Smolentsev, and M. Abdou, "Stability analysis for buoyancy-opposed flows in poloidal ducts of the DCLL blanket", *Fusion Science and Technology*, 60(2), 518 (2011).

N. Vetcha, S. Smolentsev, and M. Abdou, "Theoretical study of mixed convection Poloidal flows of DCLL blanket", *Fusion Science and Technology*, 56(2), 851 (2009).

CONFERENCE PRESENTATIONS

N. Vetcha, S. Smolentsev, and M. Abdou, "Stability analysis for the Hartmann flow with interfacial slip", 8th pamir Intl. conference on fundamental and applied MHD, Borgo, Corisca-France, 5-9 September 2011.

S. Smolentsev, **N. Vetcha**, and R. Moreau, "MHD mixed convection in a rectangular duct: 3D, 2D and 1D solutions", 8th pamir Intl. conference on fundamental and applied MHD, Borgo, Corisca-France, 5-9 September 2011.

N. Vetcha, S. Smolentsev, and M. Abdou, "Stability of mixed convection flows in poloidal ducts of DCLL blanket", 63rd Annual meeting of the APS Division of Fluid Dynamics, Long Beach, 21-23 November 2010.

N. Vetcha, S. Smolentsev, and M. Abdou, "Stability analysis for buoyancy-opposed flows in poloidal ducts of the DCLL blanket", 19th Topical meeting on the technology of fusion energy, Las Vegas, Nevada, 11-15 November 2010.

N. Vetcha, S. Smolentsev, and M. Abdou, "Theoretical study of mixed convection poloidal flows of DCLL blanket", 18th Topical meeting on the technology of fusion energy, San Francisco, California, 28-30 September 2008.

CHAPTER 1

Introduction

1.1 Context of the Problem

Magnetic confinement fusion is an approach to generating fusion power that uses magnetic fields to confine the hot fusion fuel in the form of plasma. The fuel, a mixture of Deuterium and Tritium is heated to temperatures in excess of one hundred million degrees Kelvin. At these extereme conditions they undergo fusion and release vast amount of energy. Deuterium can be extracted from the sea water. Tritium however, is not available in nature hence it needs to be produced inside the reactor. The plasma is made to levitate inside a doughnut shaped vessel (tokamak) using super conducting magnets. Blanket, is the structural component which surrounds the plasma and provides shielding to the other components of the reactor and super conducting magnets from the heat and neutron fluxes of the fusion reaction. The neutrons are slowed down in the blanket where their kinetic energy is converted into heat and collected by liquid metal coolants. By including Li in some form in these coolants will result in breeding tritium through the interaction of neutrons with Li. As tritium is produced in the coolant, it is very important to understand the flow of liquid metal coolants. In this study we address in depth a particular problem related to motion of liquid metal breeder in a magnetic field. Namely we consider various instabilities and laminar-turbulent transitions associated with non-uniform magnetohydrodynamic (MHD) flows in conditions relevant to poloidal flows in a liquid metal blanket.

1.2 Liquid metal MHD flows in a fusion blanket

When introducing the liquid metal flows as relevant to fusion blankets we mostly follow the discussion in [1]. Flows of electrically conducting fluids, such as liquid metals (LMs), in a magnetic field, called magnetohydrodynamic (MHD) flows, are of considerable use in fusion reactor systems [2]. In a liquid metal blanket, either Lithium (Li) or eutectic alloy lead-lithium (PbLi) circulates as a breeder (*e.g.* helium cooled lead lithium blanket [3]) or as a breeder and a coolant (*e.g.* dual coolant blanket [4], self-cooled blanket [5]). The LM motion in a strong reactor plasma-confining magnetic field induces an electric current, which in turn interacts with the magnetic field, resulting in the volumetric Lorentz force, which has a strong effect on the LM flow field, and through the modifications of the flow, on heat and mass transfer. Such MHD flows and have been the subject of intensive studies for many decades in many practical areas, including metallurgical applications, crystal growth, MHD pumps, MHD flow meters, MHD ship propulsion, *etc.* [6]. As applied to a blanket, MHD flows occur in a complex fusion environment, including strong multi-component spatially and time varying magnetic fields, complex geometry and multi-material domains. The magnetic field has a primary effect on the blanket performance and its thermal efficiency via changes in velocity/electric current distribution, pressure drop and heat and mass transport. Above all, the MHD phenomena in a LM blanket owe their uniqueness to the presence of a highly-intensity neutron flux, causing volumetric heating and associated buoyancy effects.

A comparison of these two (Self-cooled and separately-cooled) concepts is performed by Reimann *et. al.* [7] within the European projects. In the self-cooled concept high velocities are required to remove the heat; thus, the flow must be strongly forced, which is expressed by relatively large pressure losses induced by MHD effects. Under these conditions, the buoyancy

effects are negligible. In the case of separately-cooled devices, a weak forced flow is required for tritium extraction, and relevant temperature gradients occur: therefore the flow is mainly buoyancy driven.

At present, understanding the underlying physics of MHD flows and their impact on the blanket performance is not complete even at a quantitative level. Addressing MHD phenomena under blanket-relevant conditions is difficult due to their non-linearity, multi-scale nature, and complex blanket geometry. Numerical simulations for real geometry flows are often limited to relatively low values of operation parameters. The experimental limitations are caused by requirements of large magnetic workspace, strong prototypic magnetic fields and prototypic neutron sources, the conditions that can be hardly be met at the same time in non-fusion devices. All these make studying phenomena in the blanket conditions very challenging.

In the past, several reviews of LM MHD flows in fusion-relevant conditions were presented, focusing on the blanket issues common to all types of LM blankets, such as the MHD pressure drop, flow distribution, electrical insulation, complex geometry flows, effects due to magnetic field non-uniformity, multi-channel effect, and heat transfer [2, 8-10].

1.3 US DCLL blanket

The DCLL (dual coolant lead lithium) blanket concept evolved from the original ARIES [11] is considered in the US for testing in ITER (Fig. 1.1) and as a primary candidate for a DEMO reactor (Fig. 1.2) [12,13]. In the DCLL blanket, eutectic alloy PbLi circulates slowly (~ 10 cm/s) for power conversion and tritium breeding. Reduced activation ferritic steel is used as the structural material and helium (He) is used to cool the first wall and blanket structure. The overall geometry of the blanket modules in ITER and DEMO is similar but the number of

poloidal ducts and cross-sectional dimensions are different. The poloidal length in both cases is about 2 m, while the radial depth is smaller in ITER TBM. The liquid metal enters the inlet manifold at the bottom of the blanket module from the annulus of the concentric pipe and from there is distributed into 3 (in ITER blanket) or 4 (in DEMO blanket) poloidal ducts where it flows upwards. At the top of the module, the PbLi makes a 180^{o} turn and then flows downwards through the return ducts at the back of the module. At the bottom of the module, the liquid is collected and leaves the module from the outlet manifold through the internal tube of the concentric pipe.

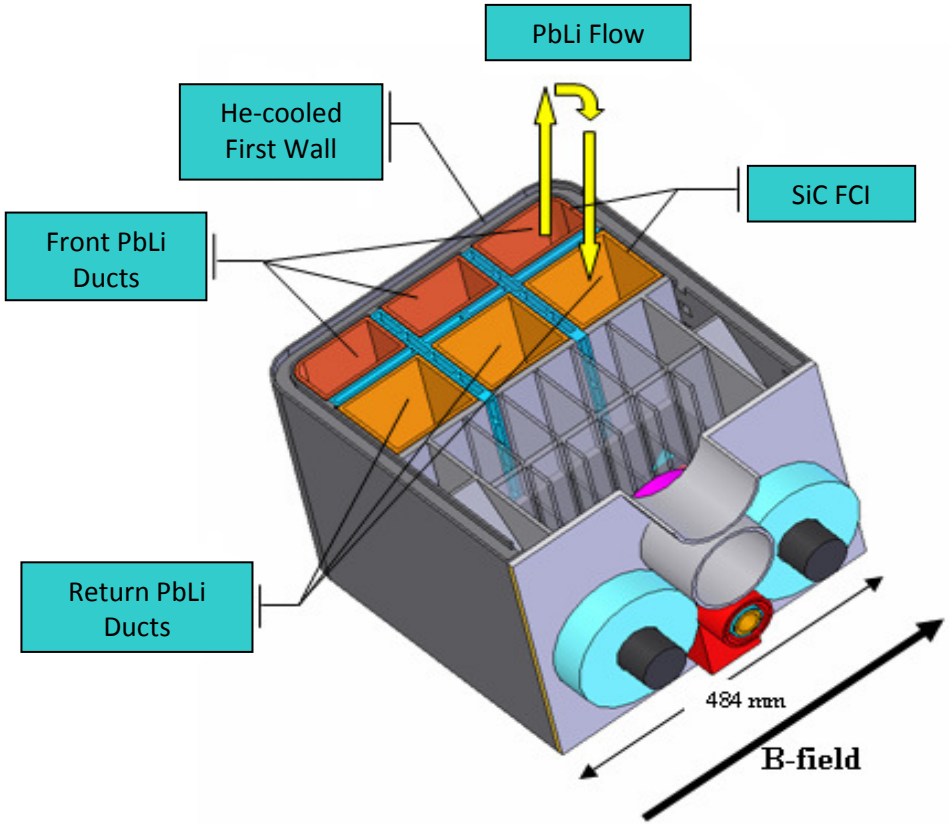

Fig. 1.1: Sketch of the US ITER DCLL Test Blanket Module.

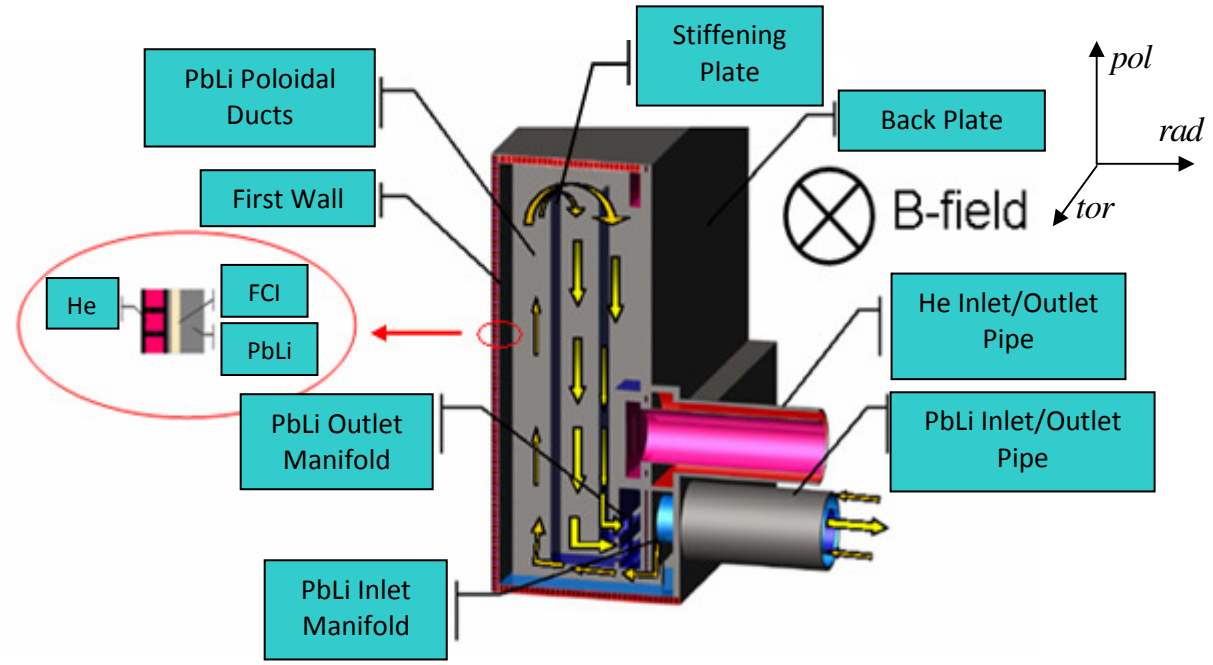

Fig. 1.2: Sketch of the US DCLL DEMO blanket module.

A key element of the DCLL concept is the flow channel insert (FCI) made of silicon carbide (SiC), either as a composite or as foam, which serves as electrical insulator to reduce the impact from the MHD pressure drop of the circulating liquid metal, and as thermal insulator to separate the high temperature PbLi from the ferritic structure. Using FCIs allow for high exit temperature (700^{o} C or even higher) and may lead to high blanket efficiency [14].The FCI is separated from the ferritic wall by a thin (~ 2 mm) gap also filled with PbLi. Both the gap flow and that inside the FCI box (bulk flow) are driven by the same pressure head. The gap and the bulk flows can be connected through small openings in one of the FCI walls (either holes or a slot). The opening may be needed for equalizing the pressure on both sides of the FCI. The blanket thermal efficiency is strongly dependent on insulating properties (electrical and thermal) of the FCI. The desirable blanket configuration requires minimization of heat leakages from the PbLi flows into

He streams as well as minimization of the MHD pressure drop, while keeping the interface temperature between the PbLi and the ferritic structure and the temperature drop across the FCI below the allowable limits. Meeting all these requirements places special limitations on the FCI design and SiC Properties, such as electrical and thermal conductivities [15]. At present, two FCI designs are underway: a single layer FCI and a double-layer (nested) FCI.

1.4 MHD flows in poloidal ducts of DCLL blanket

The flow in the poloidal ducts is characterized by three dimensionless parameters: the Hartmann number $Ha = B_0 L\sqrt{\sigma/\rho\nu}$ (Ha^2 is the ratio of electromagnetic force to viscous force); the Reynolds number $Re = u_0 L/\nu$ (ratio of inertia to viscous force); Grashof number $Gr = g\beta_t \Delta T L^3/\nu^2$ (ratio of buoyancy and viscous forces). Here B_0, L, u_0 and ΔT are the applied (toroidal) magnetic field, characteristic flow dimension, mean-flow velocity and characteristic temperature difference, while ρ, σ, ν, β_t and g stand for fluid density, electrical conductivity, kinematic viscosity, thermal expansion coefficient and acceleration due to gravity respectively. In the definition of Re and Gr, the duct half-width a (taken in the radial direction) is used as the length scale, while Ha is constructed using Hartmann length b (half width of the duct dimension in the toroidal direction). The characteristic temperature difference is defined through the maximum volumetric heating q_0 as $\Delta T = q_0 a^2/\kappa$, where κ is the fluid thermal conductivity. Some combinations of these parameters such as Stuart number or interaction parameter $N = Ha^2/Re$ can also be useful when characterizing convective flows in the blanket. Typical values of these flow parameters in the poloidal duct flows are given in Table 1.1.

Parameter *Gr/Re* stands for the ratio between buoyancy and inertia forces and hence indicates the relative importance of buoyant flows compared to forced flows. This parameter is very high in the DCLL blanket flows, showing that buoyant flows can be dominating over forced flows. Parameter *Gr/Ha* is also related to buoyant flows. A large value of *Gr/Ha* may indicate that the

Table 1.1 Basic dimensionless flow parameters in the Poloidal flow in ITER and DEMO.

Parameter	ITER	DEMO
Ha	6500	12,000
Re	30,000	60,000
Gr	7.0×10^{9}	2.0×10^{12}
N	1408.33	2400

reduction of buoyancy effects due to Ohmic losses in the MHD boundary layers at the walls perpendicular to the magnetic field (Hartmann layers) is insignificant. Parameter *Re/Ha* is the Reynolds number built through the thickness of the Hartmann layer. This parameter plays a fundamental role in the turbulence transitions. Namely, if *Ha/Re* is below its critical value $(Ha/Re)_{cr} \approx 1/300$ ([16] and [17]), turbulent flows are expected to be transitional from three-dimensional to quasi-two-dimensional (Q2D). In the blanket conditions $Ha/Re >> (Ha/Re)_{cr}$, suggesting that turbulence will be damped or most likely appears in the Q2D form. The underlying physics of Q2D MHD turbulence is related to the predominant electromagnetic dissipation mechanism (Joule dissipation), which enforces a strong flow anisotropy, until the Q2D limit is achieved. In the Q2D MHD turbulent flows, three-dimensional effects and most of

Ohmic and viscous losses occur in the thin Hartmann layers at the duct walls perpendicular to the magnetic field, while the bulk flow is essentially two-dimensional. The turbulent structures appear as big [18] (comparable in size to the duct dimension) columnar-like vortices with their axis aligned with the magnetic field direction. Such Q2D eddies do not induce much electric current and thus are weakly affected by the magnetic field. They persist over many eddy turnovers, until being damped via slow dissipating processes in the Hartmann layers. As applied to a poloidal LM blanket, the turbulent eddies will presumably be stretched in the toroidal direction thus improving radial heat and mass transport. The effect of such eddies on the pressure drop is insignificant while that on heat transfer is pronounced as recent experimental studies show [19].

Typical vortical flow patterns in a Q2D MHD turbulent flow were computed in [20] using a Q2D flow model. It was observed that the instability develops in the symmetrical internal shear layers in the M-shaped velocity profile, this instability results in a double row of counter rotating vortices whose characteristic size is comparable with the duct dimension. The inverse energy cascade nature of the Q2D turbulence was also observed.

Depending on the flow parameters, FCI properties, heating conditions *etc.*, the poloidal flows demonstrate either relatively simple or very complex behavior. Even in the absence of volumetric heating some temperature differences in the flowing LM are possible (due to the applied surface heat flux and heat losses into the helium flows), but they seem to be too small to cause significant buoyancy effects compared with the forced flow. In ITER H-H scenario, the poloidal flows can be treated using a purely forced flow model but in ITER D-T and especially in DEMO, the neutron flux, being responsible for extremely high non-uniform volumetric

heating (Fig. 1.3), will drive buoyant flows whose intensity is comparable or even higher than that of the forced flow.

In the blanket flows, the forced flow is combined with the buoyant flow resulting in mixed flow regime. Buoyancy effects in the liquid metal flow are caused by a non-uniform volumetric heating, whose intensity drops near exponentially in the radial direction as shown in Fig. 1.3. To some degree buoyancy-driven flows in the blanket are similar to the classic case of differential heating when convective flows occur in a gap between two vertical walls, one of which is hot and the other is cold, so that the buoyancy force makes the liquid metal flow upwards near the hot wall and downwards near the opposite wall. Under strong reactor magnetic field, the

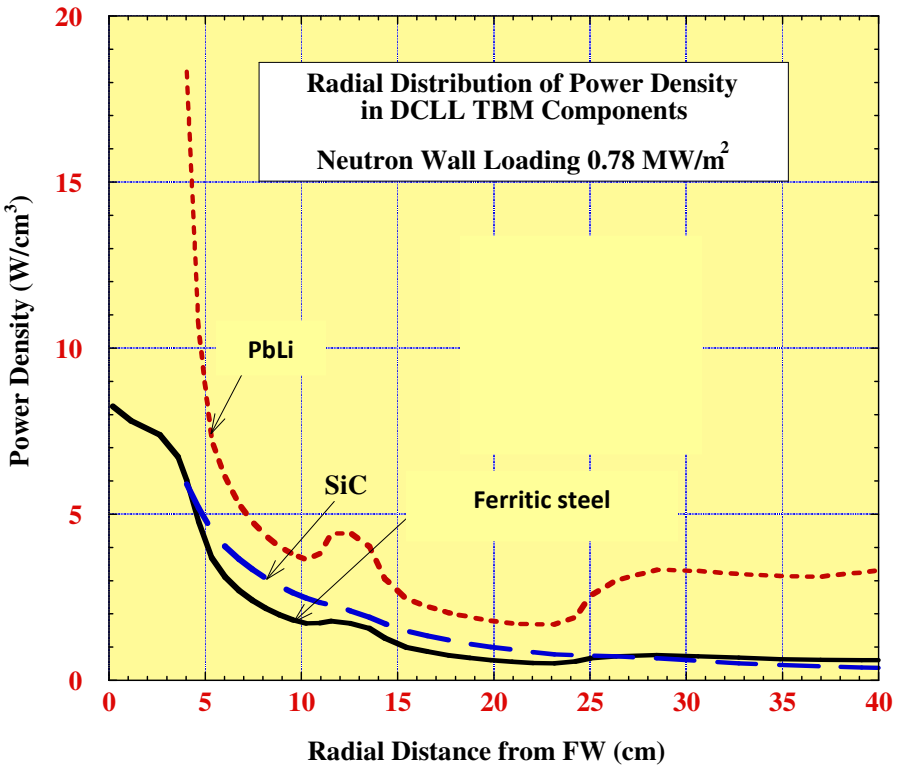

Fig. 1.3: Radial power density distribution in the ITER TBM associated with the high-intensity neutron flux.

convective flows are seen to be essentially Q2D, with 3-D effects localized in the Hartmann layers. This striking feature allows for using the Q2D flow model. The effect of buoyancy forces on the blanket operation manifests itself through better thermal mixing, which can exhibit either laminar or turbulent features. The increase in the effective heat transfer coefficient/Nusselt number due to buoyancy effects may result in higher heat losses from PbLi flow into the cooling helium streams and this will degrade thee thermal blanket efficiency. Such heat transfer intensification associated with turbulent natural convection in the presence of magnetic field has been demonstrated experimentally [21] and numerically [22]. Another concern associated with the buoyancy effects in the blanket is a risk of locally reverse flows and associated "hot spots," which may occur in the return ducts of the blanket module where the liquid flows downwards. There are a lot of studies regarding the buoyant flows under magnetic fields (*e.g.* [21-31]); some of them are relevant to fusion conditions [21, 22, 29-31].

A review of buoyant convective MHD flows is given in [32], one of the examples is the flow confined in a vertical channel formed by two electrically insulating plates of infinite extension. The magnetic field is perpendicular to the plates. The results show that the velocity scales as Gr/Ha^2, describing the intensity of the buoyant forcing and the magnetic damping, respectively. The stability of this basic laminar solution has been analyzed [29]. It is observed that the laminar unidirectional flow becomes unstable at critical values of Grashof numbers Gr_c. The flow is strongly stabilized with higher intensity of the magnetic field. Increasing the Hartmann number by a factor of 4 to $Ha = 8$ increases the Gr_c by three orders of magnitude, but this work does not give results for the values of parameters relevant under fusion conditions and for the mixed convection regime.

In MHD duct flows the boundary layers formed on the walls normal to the magnetic field are called Hartmann layers and the boundary layers formed on the walls parallel to the magnetic field are called side layers. An asymptotic analysis is carried out for laminar buoyant magnetohydrodynamic flow in vertical rectangular ducts [30] and it is observed that presence of thin side layers with high velocity jets show a strong tendency for instability. For high conductivity of walls high velocity jets were observed in the side layers for the lower values of wall conductivity, high current jets occur in the side layers, parallel to the side walls, and velocity jets are no more present. The influence of a static vertical magnetic field on the buoyancy driven convection of liquid metal heated locally at its upper surface is investigated both experimentally and numerically [28] and it is found that the Nusselt number decreases by 20% by changing the *Ha* from 0 to 120. Whereas when the magnetic field is applied perpendicular to the applied temperature gradient, the average heat transfer (Nusselt number) increases due to the transition of the flow from three-dimensional to two-dimensional and velocity and temperature fields become oscillatory [22].

Linear stability analysis is carried for flow of liquid metal through a channel with transverse magnetic field to understand the stability of side layers in case of hydrodynamic case [33]. The flow is assumed to be Q2D and the calculations were carried out for *Ha* as high as 1000. An asymptotic regime was observed for $Ha > 200$ for which $Re_c = 4.83504 \times 10^4 \, Ha^{1/2}$. This shows that in purely hydrodynamic case the side layers stay stable for the values of *Re* and *Ha* relevant to fusion conditions, but due to the internal shear layer there can be formation of vortices inside the channel, if these vortices are near the walls a viscous response is generally provoked in the near wall region [34], the process is initiated by a local concentration of the vorticity field within the boundary layer, which stimulates a rapidly-rising thin spire of fluid that ultimately interacts

strongly with the external flow, so there exist a possibility that due to the buoyant flows (which cause an inflection point in the velocity [31] which in turn results in inflectional instability) the side layers can be destabilized at a much low *Re*. As applied to MHD flows, the effect of vortex-wall interaction is studied using DNS [20]. It appears that this effect can play important role in MHD flows in a blanket.

In the case of mixed convection flows there exist two sources of instabilities – shear production and thermal buoyant potential [35]. For stably stratified flows with constant heat flux imposed on the wall, the type of instability strongly depend on Prandtl number. In the first type, which was found primarily for low Prandtl number fluids (*eg.* liquid metals) , the instability is initiated when the basic state velocity profile is distorted sufficiently to become unstable as a result of increased *Gr* or heating, but most of the kinetic energy for the instability comes from the shear production. This is called *thermal-shear instability.* The second thermal instability, which dominates in higher Prandtl number fluids, obtains its kinetic energy primarily form thermal buoyant potential, this type is called *thermal-buoyant instability.* The thermal-buoyant instability is driven by buoyancy forces due to heating and is more sensitive to thermal effects as a disturbance of the buoyancy force, induced by a temperature fluctuation, causes a disruption in the velocity field. The reason that the lower-Prandtl number fluids do not exhibit thermal-buoyant instability is the lack of temperature fluctuations. In lower-Prandtl number fluids the temperature fluctuations are rapidly smoothed by conduction.

Very little study (both numerically and experimentally) has been done to understand the mixed convection in fusion relevant conditions. For the case of flow (both upward and downward) in a vertical channel assuming Q2D approximation an analytical solution is developed [31] to calculate velocity and temperature variation across the channel, the velocities

for both upward and downward flow posses inflection points in their profiles, the solution shows region of reverse flow near the hot wall in case of downward flow, which may cause hot spots.

1.5 Instabilities and transitions in LM MHD flows

MHD flows in the blanket are known to exhibit pronounced inhomogeneity compared to their hydrodynamic counterparts [36]. One of the typical examples of MHD flows that can exhibit instability and eventually transition to a turbulent state is a fully developed flow of liquid metal in a conducting thin-wall rectangular duct in a uniform transverse magnetic field [37]. In this flow, the induced electric current **j** and the applied magnetic field $\mathbf{B}_0$ are responsible for the electromagnetic Lorentz force **j x** $\mathbf{B_0}$, which eventually leads to the so-called "M-shaped" or "M-type" velocity profile (Fig. 1.4). The distinctive features of the M-shaped profile are the two symmetric high-velocity jets scaling in width with the magnetic field as $1/\sqrt{B_0}$ at the duct walls parallel to the applied magnetic field (side or Shercliff walls), two thin boundary Hartmann layers whose thickness scales as $1/B_0$ at the walls perpendicular to the magnetic field (Hartmann walls), and a core region of almost uniform velocity bounded by the jets and the Hartmann layers. The jets themselves are composed of two legs due to the wall effect on one side and the flow-opposing electromagnetic Lorentz force on the other side. In the wall-side leg of the jet, the velocity exhibits changes from zero at the wall to the maximum without demonstrating any special points, while in the bulk-side leg, the velocity drops from the maximum to the core value exhibiting an inflection point, where the vorticity reaches its maximum. The existence of inflection points in the basic velocity profile suggests instability of the Kelvin-Helmholtz type (also known as "inflectional instability"). However, unlike a purely hydrodynamic case, the

MHD instability of this type and eventually turbulence are known to demonstrate a number of peculiarities. As suggested in [38] the role of the magnetic field is twofold. On the one hand, it is responsible for a potentially unstable basic velocity profile. On the other hand, there is a stabilizing effect of the magnetic field, which manifests itself in the form of Joule dissipation mostly caused by the induced electric currents closing through the Hartmann layers and electrically conducting walls. This additional damping reduces continuously the kinetic energy of the perturbations and thus stabilizes the flow.

The flow in a conducting thin-wall duct is, however, not a unique example of unstable MHD flows with inflection points in the basic velocity profile. Similar features can be seen in other

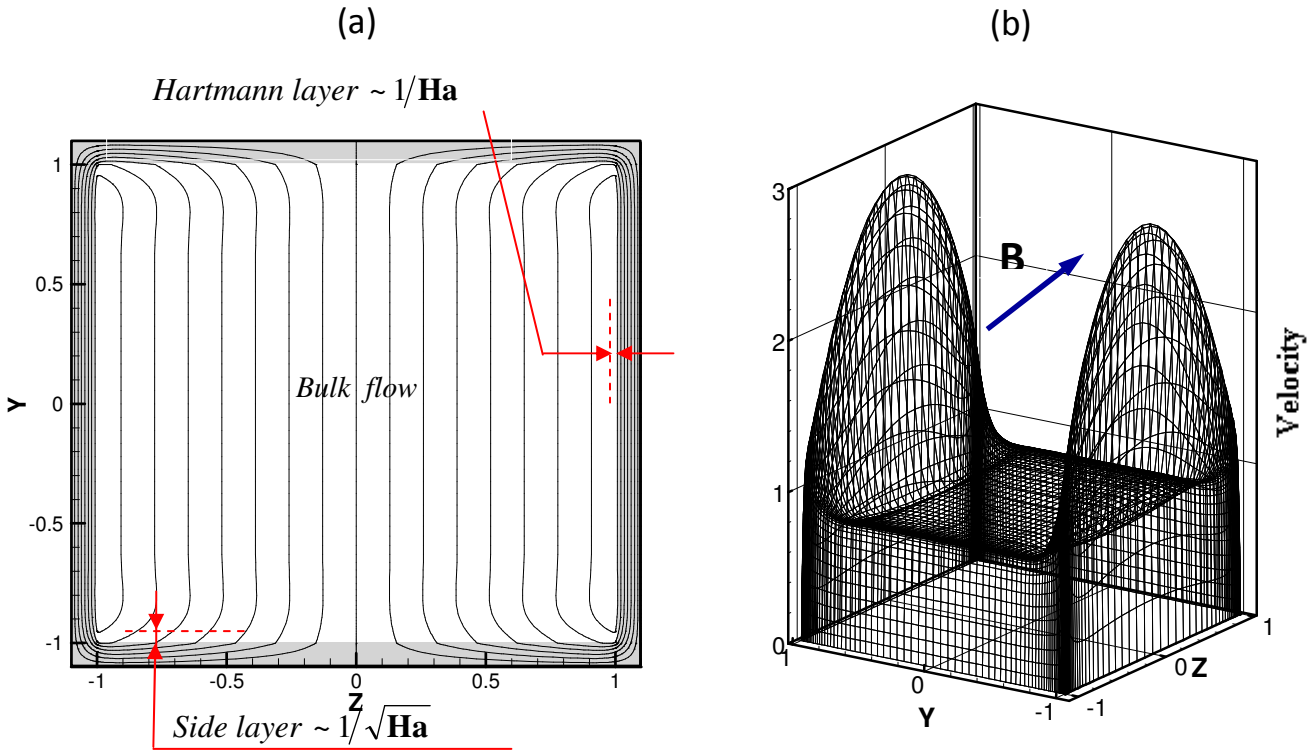

Fig. 1.4: Induced electric current (a) and velocity profile (b) in a fully developed laminar MHD flow in a thin-wall rectangular duct subject to a transverse $\mathbf{B}(0,0,B_0)$ constant magnetic field at *Ha*=200 and c_w=0.5. For definition of the Hartmann number, *Ha*, see Sec. II. The wall conductance ratio c_w is the ratio of the wall electrical conductance to that of the Hartmann boundary layer. The velocity in the figure is scaled by the mean bulk velocity.

MHD duct flows even though the duct walls are electrically insulating or partially conducting. As an example, one can refer to MHD flows in a non-conducting duct with two conducting strips imbedded symmetrically in the two Hartmann walls as turbulence promoters. In this flow studied experimentally in [39], the location of the inflection points in the velocity profile is fully determined by the strip position on the wall. Similar numerical computations are reported in [38] showing development of Kelvin-Helmoltz instability at the strip location. These and other experimental studies have also revealed that the instability is not always of the Kelvin-Helmholtz type. In addition to inflectional instability, another instability mode has been recorded in the experiments [19] for a thin-wall conducting rectangular duct. In accordance with the original author's terminology, in the *Type I* instability, the typical flow pattern is composed of anticlockwise-rotating periodic vortices, whose center of rotation is located in the bulk-side jet leg. The source of energy supply to these vortices is the bulk-side shear layer and the primary instability mode seems to be the inflectional instability. In the *Type II* instability, the near-wall vortices are clockwise-rotating with their center of rotation in the wall-side leg of the jet. These vortices cause a breakdown of the jet structure reducing the maximum velocity and increasing its thickness compared to those in the undisturbed flow. To our best knowledge the nature of this instability has not been understood yet. Recently, the stability problem for a conducting rectangular duct was revisited [40] for a large aspect ratio duct. As in previous experiments [41], the first onset of instability was observed at a critical Reynolds number mostly independent on the magnetic field strength. The measured small fluctuations remain confined to narrow regions close to the side walls, leaving the major part of the core unaffected and laminar. By increasing further the flow rate this behavior persists until a second critical Reynolds number is reached, above which perturbations amplify quickly by one or more orders of magnitude. Similar

behavior (but for lower velocities and lower magnetic field strengths) has also been predicted recently in 3D numerical computations in [42], where a sudden increase in the energy of perturbations by two orders of magnitude was found as the Reynolds number increases. These experimental and numerical observations also indicate that the instability cannot be fully explained in terms of inflectional instability. The linear stability analysis for this type of flows with a side-wall jet was performed in the past [43, 44] and recently in Ref. [45] for the Hunt flow [46], also indicating the possibility of more than one instability modes.

The analysis of instabilities and transitions presented in this paper is based on the idea of a quasi-two-dimensional MHD flow. Following the first experimental observations of the instabilities in MHD flows in conducting rectangular ducts dated back to 1970's, [18, 47] further experiments [41] for a square duct had demonstrated that the nature of the fluctuations differs from ordinary turbulence in its strong periodicity, the lack of small-scale structures and, what is very important, in its quasi-two-dimensional dynamics. As of now, the concept of quasi-two-dimensional (Q2D) turbulent MHD flows in ducts has been matured. In accordance with this concept (*e.g*. Ref. [18]), a strong magnetic field enforces the liquid motion to occur mostly in the planes perpendicular to the applied magnetic field, while the flow along the magnetic field lines is damped. The important 3D effects are still localized within the Hartmann layers, where the most dissipation losses occur. The Q2D turbulent structures appear as columnar-like vortices aligned with the field direction and are subject to the inverse energy cascade. Their intensity is a result of the balance between the Joule and viscous dissipation in the Hartmann layers, on the one hand, and the feeding mechanism associated with the instability on the other hand. Such Q2D eddies can be highly energetic, occupy the whole cross-section of the duct and persist over

many eddy turnovers. In experiments, these striking Q2D properties were first studied in [48] and later in many other laboratory experiments and 3D numerical simulations.

1.6 Study Objectives

The goal of the present research is to understand the instabilities and transitions in MHD duct flows as applicable to the fusion blanket, this knowledge is the necessary basis for further studies of heat and mass transfer. As there are many parameters such as *Re, Ha, Gr,* duct aspect ratio *etc*. which govern the flow, it has to be found that which combination of these parameters may cause the flow to become unstable and thus differentiate the stable and unstable regions. There exist different possible mechanisms of instability (inflectional instability, boundary layer instability) which are relevant to the present case. It is also possible that one type of instability will trigger other type of instability, different regions (depending on the values of the parameters) have to be identified in which each mechanism of instability dominates and finally construct a "flow map." One of the goals is also to study various vortex-vortex and vortex-wall interactions.

The key features of liquid metal flow through poloidal ducts of the DCLL blanket are the presence of inflection points in the base velocity profile and asymmetry of the velocity profile with higher velocities near the hot wall. Due to this there is a possibility of the inflectional instability and generation of a row of vortices in the channel core, it is anticipated that the side layers can be destabilized by these vortices. This interaction between the bulk vortices and boundary layer depends on the location of the inflection point.

In order to understand the effect of location of the inflection point on these interaction mechanisms, we developed a model problem based on Q2Dapproximation. With this model we

can control the location of inflection point with respect to the walls while emulating all features of M-shaped velocity profile observed in MHD duct flows. Chapter 3 will discuss in detail the model problem, analytical solution for the base velocity profile, stability analysis for the base flow and non-linear calculations performed to understand the interaction between the bulk vortices and boundary layer. Linear stability is performed to identify the dominating instability mechanism at various locations of the inflection point with different set of parameter values. We expect that at low values of *Re* the dominating instability is the inflectional instability, while at higher values of *Re* the dominating mechanism should be side layer instability which was observed in a previous study [33]. The non linear DNS like calculations are performed by time marching the governing equations in vorticity-stream function form. With these nonlinear calculations we want to understand various vortex-vortex and vortex-wall interactions, in the MHD wall bounded flows, this phenomenon has not received significant consideration yet. Once the flow reaches a turbulent state, we expect to see the thickening of near-wall jet and reduction of the jet velocity as observed in experiments [40, 41, 49].

Under blanket conditions the asymmetry in the velocity profile is due to the non-uniform volumetric heating, whose intensity drops exponentially in the radial direction as shown in Fig. 1.3. To understand this kind of flows, we considered flow in a rectangular duct with exponentially decaying heating. Chapter 4 discusses the formulation of the problem and methods used to study the instabilities and transitions in this flow. We expect that the instability mechanisms in this flow are similar to that observed in flows with M-shaped velocity profile. Using linear stability, we identified regions where each instability mechanism is dominating. Additionally, we also derived an expression to calculate critical Hartmann number ($\mathbf{Ha_{cr}}$) as a

function of *Re* and *Gr*. The non-linear calculations revealed that there are two turbulent regimes strong and weak. The features of each regime are discussed further in chapter 4.

Lastly, a 3D numerical modeling of mixed convection flow in the DCLL geometry is performed using a finite volume based MHD solver HIMAG. The capabilities of the solver are discussed on chapter 5. These 3D calculations showed that the velocity and temperature field showed a tendency towards two-dimensionaliztion as *Ha* is increased. The 3D results are compared against the 1D analytical solutions obtained by assuming fully developed conditions.

CHAPTER 2

Mathematical Modeling

2.1 Introduction

The numerical modeling of the flows of electrically conducting fluids in the presence of a magnetic field has been the subject of interest in many disciplines. The interaction of moving electrically conducting fluid with a magnetic field gives rise to a wide variety of MHD phenomenon. The study of MHD flows is intriguing not only in its physical and mathematical richness but also in its wide range of technical applicability. The flows of electrically conducting fluids in the presence of a magnetic field occur widely in nature as well as in industrial applications. These range from cosmic phenomenon like stellar plasma dynamics, to geophysical phenomenon like the geodynamo of the earth, to industrial applications like controlled flow of liquid metals for casting etc. In simple terms the governing physics behind MHD phenomenon can be described as follows. The motion of conducting fluid across the magnetic lines of force creates potential differences which, cause electric currents to flow. The magnetic fields associated with these currents modify the magnetic field which creates them. On the other hånd, the flow of electric current across a magnetic field is associated with a body force, the so called Lorentz force, which influences the fluid flow [50]. It is this intimate interdependence of hydrodynamics and electrodynamics which really defines and characterizes magnetohydrodynamics. It is not surprising that a variety of specialized techniques need to be developed to accurately model and understand the diverse range of magnetohydrodynamic

phenomenon. A classification of the magnetohydrodynamic flows according to the dominant phenomenon is helpful in development of modeling techniques specific to each class. One dominant classification is based on the physical state of the conducting medium under study. The medium could be plasma or a weakly ionized gas, which can be differentiated as compressible MHD flows or the medium could be an electrically conducting liquid metal or an electrically conducting molten salt, which fall under incompressible MHD. Even though the numerical modeling challenges brought about by compressible MHD and incompressible MHD are equally arduous, they are very different in nature [50].

There has been a renewed interest in the study and development of numerical modeling techniques for incompressible MHD flows during the past decade due to its immense application in nuclear fusion science and technology [51]. A key component of a magnetic fusion device is the blanket which is located between the plasma and the magnetic field coils. The blanket absorbs neutrons transforming their energy into heat, which is then carried away by a suitable coolant. The blanket also performs the task of breeding tritium to maintain the fuel cycle for the fusion reactions. Most of the advanced blanket concepts that have been proposed employ some form of liquid lithium which acts as the primary heat extraction agent as well as the source for breeding tritium [12]. The electrically conducting liquid metal alloy or molten salt containing lithium flows through complex flow paths within a complex 3D magnetic field topology and 3D thermal field. The performance evaluation of flowing liquid lithium containing blanket requires the modeling of critical MHD phenomenon like mixed convection, developing MHD flow in bends, expansions and contractions, MHD turbulence etc, which are relatively new and unexplored areas. Traditionally the numerical modeling for incompressible MHD has been limited to fully developed flow of liquid metals or molten salts in channels. Also the range of key

non dimensional parameters used in numerical modeling, like the Hartmann number has been quite limited. Liquid metal MHD for magnetic fusion blanket has brought out a series of advances in numerical modeling of incompressible flows at high Hartmann numbers. Apart from incompressible MHD modeling for the liquid metal blanket, there is a significant interest in studying the flow of fast moving thin films of liquid metal to be used as the plasma contact at the divertor of the magnetic fusion device.

Liquid metal flows under the influence of a magnetic field are governed by the Navier-Stokes equations and electrodynamic equations. The equations which are to be solved for numerically simulating these flows are derived from different electrodynamic equations like Maxwell's equations, Ampére's law, Ohm's law and charge conservation. If the induced magnetic field is not strong enough to perturb the imposed magnetic field it is enough to solve Navier-Stokes equations along with a Poisson equation for electric potential but if the induced magnetic field is strong then one should additionally solve a vector equation with solenoidal constraint for the induced magnetic field.

2.2 Governing equations for incompressible magnetohydrodynamics

The governing equations for MHD include electromagnetic equations coupled with fluid flow equations as explained below.

2.2.1 Maxwell's equations

Maxwell's equations are a set of four equations which describe the interrelationship between electric fields, magnetic fields, electric charge, and electric current. In brief they express

1. How electric charges produce electric fields (Gauss's law)

$$\nabla \cdot \mathbf{E} = \frac{\rho_{\mathrm{e}}}{\varepsilon_0}, \tag{2.1}$$

2. The experimental absence of magnetic monopoles (solenoidal nature of **B**)

$$\nabla \cdot \mathbf{B} = 0, \tag{2.2}$$

3. How changing magnetic fields produce electric fields (Faraday's law of induction)

$$\nabla \times \mathbf{E} = -\frac{\partial \mathbf{B}}{\partial t}, \tag{2.3}$$

4. How electric currents and changing magnetic fields produce magnetic fields (Ampère-Maxwell equation)

$$\nabla \times \mathbf{B} = \mu_{\mathrm{m}} \left(\mathbf{j} + \varepsilon_0 \frac{\partial \mathbf{E}}{\partial t} \right). \tag{2.4}$$

Here $\mathbf{E}, \mathbf{B}$ and $\mathbf{j}$ are respectively electric fields, magnetic field and current density vectors; while $\rho_{\mathrm{e}}, \varepsilon_0$ and μ_{m} are the volume charge density, permittivity of free space and magnetic permeability of the medium.

2.2.2 Charge conservation equation

As given in the previous section, the Ampére-Maxwell equation is given in Eq. (2.4). The last term in Eq. (2.4) was introduced by Maxwell as a correction to Ampére's law and is called the displacement current; it is introduced to account for the conservation of charge. However, the contribution of that term to (2.4) is very small in MHD [52]. This is readily confirmed

$$\varepsilon_0 \frac{\partial \mathbf{E}}{\partial t} \sim \frac{\varepsilon_0}{\sigma} \frac{\partial \mathbf{j}}{\partial t} \sim \tau_{\mathrm{e}} \frac{\partial \mathbf{j}}{\partial t} << \mathbf{j},$$

The quantity τ_e is called the charge relaxation time, and for a typical conductor has a value of around 10^{-18} s. Therefore, we can use the pre Maxwell form of (2.4), which is simply the Ampère's law in differential form.

$$\nabla \times \mathbf{B} = \mu_m \mathbf{j}, \tag{2.5}$$

Applying divergence to the above equation leads to

$$\nabla \cdot \mathbf{j} = 0. \tag{2.6}$$

The above equation (2.6) is known as charge continuity equation for MHD.

2.2.3 Poisson equation for electric potential

One another important equation which governs the flow of liquid metal subjected to a magnetic field is Ohm's law which is given as

$$\mathbf{j} = \sigma(\mathbf{E} + \mathbf{u} \times \mathbf{B}), \tag{2.7}$$

where $\vec{\mathbf{u}}$ is the velocity vector and σ is the electric conductivity, replacing $\mathbf{E} = -\nabla\phi$, where ϕ is the electric potential, the equation (2.7) gets modified as

$$\mathbf{j} = \sigma(-\nabla\phi + \mathbf{u} \times \mathbf{B}), \tag{2.8}$$

Using the charge conservation equation (2.6), taking the divergence of Eq. (2.8) yields a Poisson equation for electric potential.

$$\nabla^2\phi = \nabla \cdot (\mathbf{u} \times \mathbf{B}). \tag{2.9}$$

2.2.4 Induction equation

If we combine Ohm's law, Faraday's equation and Ampère's law we obtain an expression relating $\mathbf{B}$ to $\mathbf{u}$.

$$\frac{\partial \mathbf{B}}{\partial t} = -\nabla \times \mathbf{E} = -\nabla \times \left[(\mathbf{j}/\sigma) - \mathbf{u} \times \mathbf{B} \right] = \nabla \times \left[\mathbf{u} \times \mathbf{B} - \nabla \times \mathbf{B}/\mu_{\mathrm{m}}\, \sigma \right],$$

Noting that $\nabla \times \nabla \times \mathbf{B} = -\nabla^2 \mathbf{B}$ (since $\mathbf{B}$ is solenoidal), this simplifies to

$$\frac{\partial \mathbf{B}}{\partial t} = \nabla \times (\mathbf{u} \times \mathbf{B}) + \lambda \nabla^2 \mathbf{B}, \tag{2.10}$$

where $\lambda = (\mu_{\mathrm{m}} \sigma)^{-1}$ is called the magnetic diffusivity. The Eq. (2.10) is also known as the transport or advection-diffusion equation for $\mathbf{B}$, where $\mathbf{B}$ now is the total magnetic field which includes both the imposed and the induced magnetic fields. However, as the former is usually constant, the equation effectively computes the induced magnetic field. As the Eq. (2.10) is linear, the imposed component of $\mathbf{B}$ may be subtracted out of the equation which then could be used to compute only the induced field (with boundary condition for the induced field). Using the fact that $\mathbf{B}$ is solenoidal and the the fluid is incompressible, $\nabla \cdot \mathbf{u} = 0$ we can get the following modified form of the induction equation.

$$\frac{\partial \mathbf{B}}{\partial t} + (\mathbf{u} \cdot \nabla)\mathbf{B} = (\mathbf{B} \cdot \nabla)\mathbf{u} + \lambda \nabla^2 \mathbf{B}. \tag{2.11}$$

The equations for the flow field are as follows:

2.2.5 Continuity equation

The general continuity equation is

$$\frac{\partial \rho}{\partial t} + \nabla \cdot (\rho \mathbf{u}) = 0, \tag{2.12}$$

For constant density the continuity equation (2.12) becomes,

$$\nabla \cdot \mathbf{u} = 0. \tag{2.13}$$

2.2.6 Momentum equation

The balance of linear momentum for an incompressible liquid metal MHD flow is written as

$$\rho\left[\frac{\partial \mathbf{u}}{\partial t}+(\mathbf{u}.\nabla)\mathbf{u}\right]=-\nabla p+\rho\nu\nabla^2\mathbf{u}+\mathbf{f}+\mathbf{j}\times\mathbf{B}, \tag{2.14}$$

Here $\mathbf{u}$ denotes velocity vector, p the pressure, ρ the fluid mass density, ν its kinematic viscosity. As can be seen from the above equation, the temporal evolution of linear momentum of a fluid element is effected by the pressure force, $-\nabla\mathbf{p}$, viscous friction, $\rho\nu\nabla^2\mathbf{u}$, by volumetric forces $\mathbf{f}$ of non-electromagnetic origin such as gravity, buoyancy and by the occurrence of Lorentz, $\mathbf{j}\times\mathbf{B}$. Lorentz forces couple the mechanical and electrodynamic states of the system. In the blanket conditions along with the Lorentz force there is also buoyancy force acting on the fluid element. Using Boussinesq approximation, this force can be written as $\mathbf{f}=(-1)^{\mathrm{n}}\, g\beta_{\mathrm{t}}(T-\overline{T})\mathbf{e}_{\mathrm{x}}$, where g is the acceleration due to gravity, β_{t} is the volumetric expansion coefficient, T is the temperature, $\overline{T}$ is the mean bulk temperature of the liquid. Parameter $n = 1$ corresponds to buoyancy-opposed flows (forced flow is downwards), while $n=2$ to buoyancy-assisted flows (forced flow is upwards).

2.2.7 Energy equation

The balance of the total energy in a volume element leads to a convection diffusion equation for temperature of the form

$$\rho c_p\left[\frac{\partial T}{\partial t}+(\mathbf{u}.\nabla)T\right]=\nabla\cdot(\kappa\nabla T)+\frac{1}{\sigma}\mathbf{j}^2+\Phi+\mathrm{Q} \tag{2.15}$$

where c_p is the specific heat and κ is the thermal conductivity of the fluid. The terms on the right hand side of the above equation represent diffusive flux, joule dissipation, viscous dissipation

and volumetric energy source (*eg.* volumetric heat generation due to neutrons in the blanket) respectively.

The equations of MHD can be non dimensionalized using the characteristic velocity scale (U_0), characteristic value of the magnetic field (B_0), the length scale of the problem (L). Using these scales, three non-dimensional parameters of significance emerge from the equations and these are defined as the magnetic Reynolds number (Re_m), the Hartmann number (Ha) and the interaction parameter (N). The definitions of these non-dimensional parameters are as follows:

$$Ha = B_0 L\sqrt{\frac{\sigma}{\rho\nu}}, \tag{2.16}$$

$$Re_{\mathbf{m}} = \mu_{\mathbf{m}}\sigma U_0 L, \tag{2.17}$$

$$N = \frac{\sigma B_0^2 L}{\rho U_0}. \tag{2.18}$$

The magnetic Reynolds number (Re_m) plays a very important role in developing numerical models for incompressible MHD flows. The parameter $\mathrm{Re}_{\mathbf{m}}$ can be interpreted as the ratio of the magnetic field induced by the electric currents generated by MHD phenomenon, to that of external applied magnetic field. If the MHD flow in question falls in the regime where $Re_{\mathbf{m}} << 1$, the induced magnetic field can be neglected in comparison to the applied magnetic field. In other words the flows in this regime behave in a way that the velocity field does not affect the magnetic field. Most of the liquid metal/molten salt MHD applicable to magnetic fusion fall in this category. This regime of MHD flows with $Re_{\mathbf{m}} << 1$ allows the equations to be simplified in a way as to neglect the induced field and is termed as the indcutionless approximation. The

modeling of incompressible MHD flows in the inductionless approximation leads to solution methodology called the electric potential formulation. Since the induced magnetic field is negligible, if the applied magnetic field $(\mathbf{B}_0)$is steady, the electric field is irrotational and therefore can be represented as the negative gradient of an electric potential ϕ. As shown in section 2.2.3, a Poission equation for the electric potential (Eq. 2.9) can be derived by using the Ohm's law and divergence free property of the electric current.

The solution of the electric potential Poisson equation yields the electric potential field by the use of appropriate boundary conditions, which is in turn used to calculate the induced electric currents in the domain. The induced currents provide the Lorenz force, which is used as a body force in the momentum equations. The electric potential formulation is the most popular methods for solution of the equations of incompressible MHD for problems where magnetic Reynolds number is very small. The main reason behind this is that in this formulation the solution of the vector equation (2.11) is replaced by the solution of a scalar Poisson equation, which is computationally less expensive. While on the subject of solution of equations of incompressible MHD, the next section is devoted to a brief discussion of the various formulations that are available and the particular problems that they are most suited for.

2.3 The solution methodology for equations of incompressible MHD

The ordinary flows of incompressible fluids are generally modeled using the Navier-Stokes equations in several different forms [53]. Other than the traditional primitive variables formulations that solve for the velocity and pressure fields, specialized formulations that make use of a vector potential or still other formulations like vorticity – velocity formulation are

advantageous for modeling certain type of problems. In Incompressible MHD flows, the hydrodynamic variables are calculated along with the electromagnetic ones and this allows for many more choices when formulating the problem. The different formulations for incompressible MHD solve for the scalar electric potential (ϕ), the magnetic vector potential $(\mathbf{A})$, the magnetic field $(\mathbf{B})$, the current vector potential (ζ)or some combinations of these quantities [37, 54]. Depending on the particular MHD problem, selecting the one or the other set of magnetic variables, in combination with the proper numerical technique can result in a higher accuracy and faster convergence. Vice versa an inappropriate choice will lead to unphysical calculations with poor or no convergence at all. The choice of the electromagnetic variables can also affect the size and shape of the computational domain and the way in which the boundary conditions are formulated that ultimately affects the computational cost. The two most commonly used formulations for the solution of incompressible MHD are the electric potential formulation (applicable for $Re_{\mathbf{m}} << 1$) and the formulation based on the solution of the magnetic induction equation. Another formulation that is not much used is based on the electric current density and is called the **j**-formulation. Next we will briefly describe these formulations along with their strengths and weaknesses with regards to modeling of incompressible MHD flows.

The electric potential formulation has been discussed in section 2.2. In modeling of incompressible flows for fusion applications, the associated Hartmann number falls in the range $Ha = 10^3$-10^4. In general the electric potential formulation has been associated with poor convergence at high *Ha*, but recent developments in numerical techniques that have been developed by researchers at UCLA and have been implemented in HIMAG [55, 56] show that the electric potential formulation can give satisfactory results at high Ha, provided that the correct numerical discretization is used. This can be explained by means of a small example. If

we consider fully developed MHD flow in a rectangular channel with the flow velocity in the x direction, all the derivatives with respect to x are zero except for that of pressure, which is a constant in the flow. Magnetic field is applied in the y direction and the electric potential formulation is used, we obtain the following incompressible MHD equations describing this problem:

$$\mu\nabla^2 u - j_z B = \frac{dp}{dx}, \tag{2.19}$$

$$\mathbf{j} = \left(0,\ j_y,\ j_z\right) = \sigma\left(0, -\frac{\partial\phi}{\partial y}, -\frac{\partial\phi}{\partial z} + uB\right), \tag{2.20}$$

$$\nabla^2\phi = \frac{\partial(uB)}{\partial z}. \tag{2.21}$$

In the core of the flow, the MHD velocity profile represents slug flow so the laplacian of velocity is almost zero and hence the Lorentz force is balanced by the pressure gradient alone. If the applied magnetic field is considered to be unity, in a rectangular domain where y and z extents are between -1 and 1, and if a length scale of unity is used for non dimensionalization along with a core velocity close to unity, the above relation gives:

$$-\frac{\partial\phi}{\partial z} + u = -\frac{1}{\mu Ha^2}\frac{dp}{dx}. \tag{2.22}$$

At high *Ha,* the right hand side of the equation is very small. The core velocity being close to 1, we require the gradient of the electric potential above to be also close to 1 in magnitude. We

then have a situation in which current is computed from the difference between two (nearly identical) large numbers. It turns out that this poses some restrictions on the manner in which current is numerically computed from the electric potential and is the leading source of errors at high *Ha.* In HIMAG steps have been taken to alleviate this problem by ensuring that the electric current calculation is carried out while preserving the required order of accuracy by means of correct discretization.

The second formulation of interest for incompressible MHD is the formulation that is based on the solution of the induction equation (2.11). Alternative to Ohm's law, the electric current can also be calculated from Ampere's law as:

$$\mathbf{j} = \frac{1}{\mu_{\mathrm{m}}} \nabla \times \mathbf{B}_{\mathrm{i}}, \tag{2.23}$$

From the point of view of numerical computations, equation (2.23) has some advantages over equation (2.7). Even with some numerical inaccuracy with the numerical computation of the induced magnetic field $(\mathbf{B}_{\mathrm{i}})$, the electric current calculated with (2.23), by virtue of the vector identity, will always be divergence free (within the numerical accuracy of the divergence operator). Unlike the electric potential formulation, which has a distribution in the conductor only, the induced magnetic field diffuses from the flow domain to far outside zones. Strictly speaking the vanishing boundary condition for the induced magnetic field should be applied at 'infinity' which means that large computational domains have to be handled. Also when solving for the induction equation, it is necessary to impose the divergence free constraint on the induced magnetic field in the numerical computations.

2.4 General magnetohydrodynamic concepts

Before discussing the instabilities and transition mechanisms of the liquid metal MHD flows, it is necessary to understand some basic concepts of these flows. The magnetic field is able to influence the behavior of a conducting fluid flow via the Lorentz force $\mathbf{F} = q(\mathbf{u} \times \mathbf{B})$, where q is the charge of a particle. This force causes the positive holes and negative electrons to move in opposite directions, perpendicular to both the velocity and magnetic field vectors. This charge separation will set up an electric field opposing the further motion of the charges. As seen from the Ohm's law (Eq. 2.7) a net current will result as the balance of these two effects. However, this induced current is still perpendicular to $\mathbf{B}$, and thus produces an additional Lorentz force on the moving charges which is transmitted to the surrounding fluid. This force is represented by the body force term $\mathbf{j} \times \mathbf{B}$ in the momentum equation 2.14.

According to Ampère's law (Eq. 2.5) current density produces an associated magnetic field that encircles it. Thus the current induced by the movement of a fluid in a magnetic field will in turn produce its own magnetic field, where the total field is the sum of the applied and induced magnetic fields. In most laboratory situations, this induced magnetic field is considerably smaller than the applied magnetic field. In all cases considered in this study, $|\mathbf{B_i}| << |\mathbf{B}_0|$.

One introductory MHD problem of particular relevance to the liquid metal MHD duct flows is the so-called Hartmann problem, which is a MHD analogy of the plane Poiseuille flow. The geometry of the problem is shown in Fig. 2.1 where t_w and $\sigma_\mathbf{w}$ are the thickness and electrical conductivity of the channel walls perpendicular to the field. The channel is assumed to extend infinitely in the z direction. The equations describing this problem are the x component of the momentum equation (Eq. 2.14) and the x component of the induction equation (Eq. 2.11).

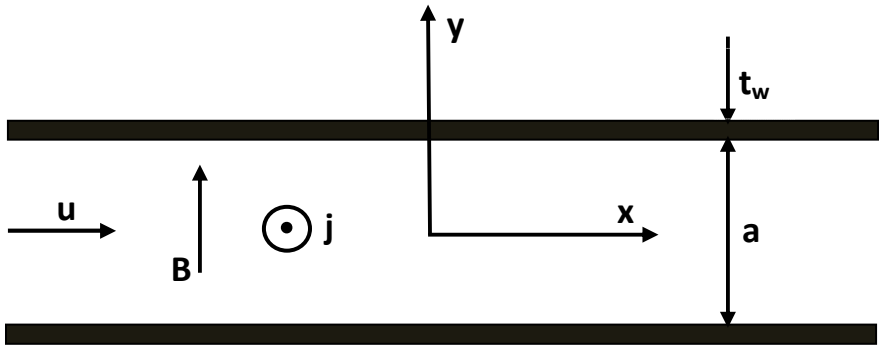

Fig. 2.1: Geometry of the Hartmann flow.

$$\frac{\partial^2 u}{\partial y^2} + Ha\frac{\partial B_x}{\partial y} = -1, \tag{2.24}$$

$$\frac{\partial^2 B_x}{\partial y^2} + Ha\frac{\partial u}{\partial y} = 0. \tag{2.25}$$

The constant pressure gradient is assumed to be the driving force. Since the applied field is in the y direction, B_x is the only resultant induced field. The details of the boundary conditions and the solution of the above equations are given in [36].

The resulting forms of the velocity and induced magnetic field are:

$$u(y) = \hat{u}\left[1 - \frac{cosh(Hay)}{cosh(Ha)}\right], \tag{2.26}$$

$$B_x(y) = \hat{u}\frac{sinh(Hay)}{cosh(Ha)} - \frac{y}{Ha}. \tag{2.27}$$

with the characteristic magnitude of velocity

$$\hat{u} = \frac{1}{Ha}\frac{\Sigma + 1}{\Sigma Ha + tanh(Ha)}, \tag{2.26}$$

The term $\Sigma = \frac{\sigma_w t_w}{\sigma(a/2)}$, is known as the wall conductance ratio and represents the conductivity of the wall relative to that of fluid. The walls perpendicular to the applied magnetic field are called Hartmann walls.

Fig. 2.2 shows the variation of velocity and induced magnetic fields obtained from Eqs. 2.26 and 2.27 for different Hartmann numbers. With the increasing Hartmann number we see the formation of a constant core region in the interior of the channel, and Hartmann boundary layers near the channel walls. This layer forms due to wall friction and acts as a return path for the induced electric current. Their thickness is typically of the order $\frac{a/2}{Ha}$.

The overall magnitude of the electromagnetic force on the fluid depends heavily on the conductivity of the walls. If the walls conduct very little, all current must return in the thin Hartmann layers resulting in greater resistance of the return current path as compared to the case of highly conducting wall. This greater resistance allows a buildup of charge, and thus a larger electric field opposing the induced currents in the core region. This results in less overall current flow, and therefore less electromagnetic force retarding the flow. For the case of insulating walls, all current returns through the fluid Hartmann layers and there is zero net electromagnetic force acting on the fluid. However, the viscous drag is increased from the parabolic case (Ha = 0) due

to the modifications of the velocity profile and increased friction acting through the thin layers at the walls with large velocity gradients. On the other hand, highly conducting walls short out the charge separation and prevent large electric fields from forming. Thus the induced currents are large and the flow is more heavily affected.

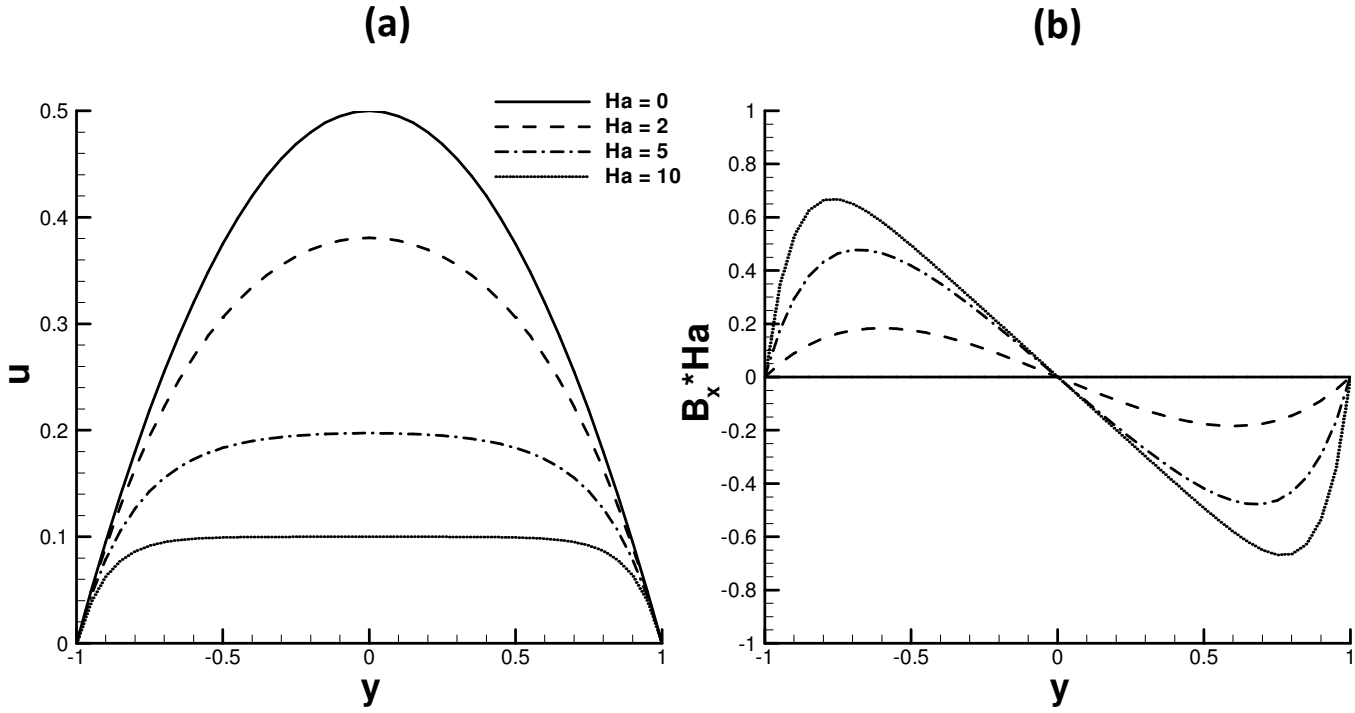

Fig. 2.2: Hartmann (a) velocity and (b) induced magnetic field profiles for $\sigma_w = 0$ and $Ha = 0$, 2, 5, and 10.

In addition to this notion of Hartmann layers, we must also briefly consider the behavior of the currents at the other set of walls parallel to the field (removed to ∞ in Fig. 2.1). Close to these walls the currents induced in the core region must turn and move along field lines to the Hartmann walls. As the currents turn, they no longer interact with the field to produce a retarding

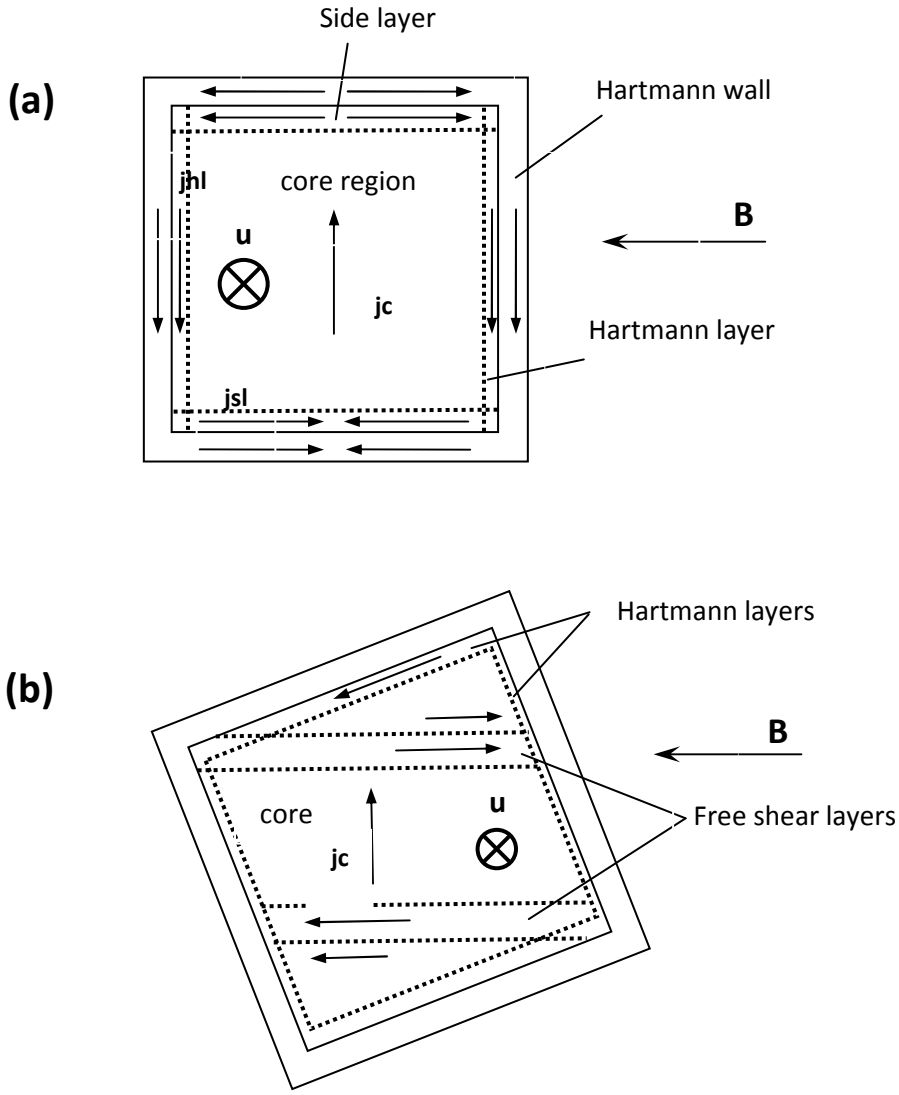

Fig. 2.3: Flow regions and current paths for a rectangular duct (a) perfectly aligned (b) not perfectly aligned with the magnetic field.

effect on the local flow. This allows surge in the velocity to develop which helps match the constant electric potential distribution (along the field) in the core region to a parabolic one that forms in the parallel layer. The potential in the boundary layer is parablocially varying since the current is linearly increasing as the core current enter the layer along the width of the duct. In these regions, the jets of fluid that form can carry a large portion of the total flow. These layers

are called side layers or parallel layers and have a typical thickness of $\frac{a/2}{\sqrt{Ha}}$. Unlike Hartmann layers, when the field is exactly aligned with the walls of a rectangular duct the parallel layers detach from the wall and form a type of free shear layer protruding from corner wall regions of discontinuous electrical conductivity. These shear layers mark the point of the flow where core currents again start to flow parallel to the field though the layers themselves are not necessarily high current carriers. Fig. 2.3 depicts the flow regions and current paths for a typical rectangular duct.

This idea of active boundary layers is pivotal in the understanding of the MHD flow. Unlike the passive viscous boundary layers of ordinary hydrodynamics, Hartmann and side layers exert a significant effect on the core floe due to the fact that they control the amount of current flowing in the core. Even when the walls are removed a good distance from the core region of interest, they still cannot be ignored.

2.5 Q2D approximation

In a strong magnetic field, flow perturbations along the magnetic field lines tend to be inhibited by the action of the magnetic field due to a kind of "magnetic diffusion" [18] and a quasi-two-dimensional (Q2D) flow is promoted. In the analysis of this kind of flows it is usual to split the flow domain into core and boundary layers (e.g. [36]). In a strong transverse magnetic field, the Hartmann layers are very thin ($O(Ha^{-1})$) and the core variables present no or slight variation (compared with those in the Hartmann layers) along the magnetic field lines. Under these conditions it is reasonable to reduce the computational effort of solving a three-dimensional problem to a two-dimensional flow formulation for the core variables. Such an approach, originally established by Sommeria and Moreau [18] in the context of turbulent flows in ducts

with insulating walls, has been successfully applied to a number of MHD duct flows by integration (averaging) of the equations along the magnetic field lines [57-59]. Such a turbulent MHD flow in a strong magnetic field is described by SM82 [18] model in which the equation of motion 2.14 takes the following form:

$$\frac{\partial \mathbf{u}}{\partial t} + (\mathbf{u}.\nabla)\mathbf{u} = -\frac{1}{\rho}\nabla p + \nu\nabla^2\mathbf{u} + \frac{1}{\rho}\mathbf{f} - \frac{\mathbf{u}}{\tau}, \tag{2.29}$$

Here $\mathbf{u}[U(x,y,t),V(x,y,t),0]$ is the two-dimensional velocity field, and $\tau = \frac{L}{B_0}\sqrt{\frac{\rho}{\sigma\nu}}$ is the so-called "Hatmann braking time", which is a time-scale of vortex damping due to ohmic and viscous losses in the Hartmann layers. The characteristic length L is the half width of the duct in the direction of the applied magnetic field. In the present work, to carry out the non-linear DNS type calculations we considered the vorticity-streamfunction form of equation 2.29. Following the standard definition of vorticity ω $\left(\omega = \frac{\partial V}{\partial x} - \frac{\partial U}{\partial y}\right)$, and streamfunction $\psi\left(U = \frac{\partial \psi}{\partial y}, V = -\frac{\partial \psi}{\partial x}\right)$ the equations of motion are given by the following two equations:

$$\frac{\partial \omega}{\partial t} + \frac{\partial \psi}{\partial y}\frac{\partial \omega}{\partial x} - \frac{\partial \psi}{\partial x}\frac{\partial \omega}{\partial y} = \nu\left(\frac{\partial^2 \omega}{\partial x^2} + \frac{\partial^2 \omega}{\partial y^2}\right) - \frac{\omega}{\tau} \tag{2.30}$$

$$\frac{\partial^2 \psi}{\partial x^2} + \frac{\partial^2 \psi}{\partial y^2} = -\omega \tag{2.31}$$

CHAPTER 3

MHD flows with M-shaped velocity distribution

3.1 The model problem

The main assumption we make here is that in a strong magnetic field the MHD duct flow is essentially Q2D, as described in Section 1.2.1. The Hartmann layers are assumed to be passive, not producing turbulence, while the flow in the side layers and eventually the bulk flow can become unstable and turbulent. Such flows with passive Hartmann and active turbulent side layers have recently been observed in DNS studies even at relatively low *Ha* numbers [60].

A mathematical model for Q2D flows in a strong uniform magnetic field in a duct with insulating walls was first proposed in Ref. [18] by neglecting inertial effects in the Hartmann layers, which is also known as an "SM82" model. A variant of the SM82 model that takes into account the inertial effects was also developed in Ref. [61]. In the particular case of a very strong magnetic field this model reduces to the original one. At present, the applicability of the SM82 model to MHD duct flows in a strong magnetic field seems to be well justified in general, although some departure from the Q2D behavior can be observed in some situations, [62, 63] for example in complex geometry ducts, even though the applied magnetic field is strong. Relevance of SM82 in the case of simple rectangular duct flows has been verified against 3D results showing that the difference is less than 10% [61]. Such vortices do not induce much electric current and also experience lower viscous dissipation compared to their 3D counterparts, and thus can persist over many eddy turnovers, until being damped via slow dissipating processes. There are several examples of applying the SM82 model or its modifications to various MHD

flows in ducts (see, *e.g.* Ref. [38, 57-59, 61, 64]). In practice, the SM82 model describes a 2D bulk flow at the duct mid-plane, but it includes a linear drag term associated with the Hartmann layers. There have been some efforts to extend the SM82 model to the case of electrically conducting Hartmann walls [38, 65] but these models are not capable of reproducing the near-wall jets and, in fact, are limited to particular cases like that in Ref. [38]. Therefore, these modified models don't comply with the goals of the present study.

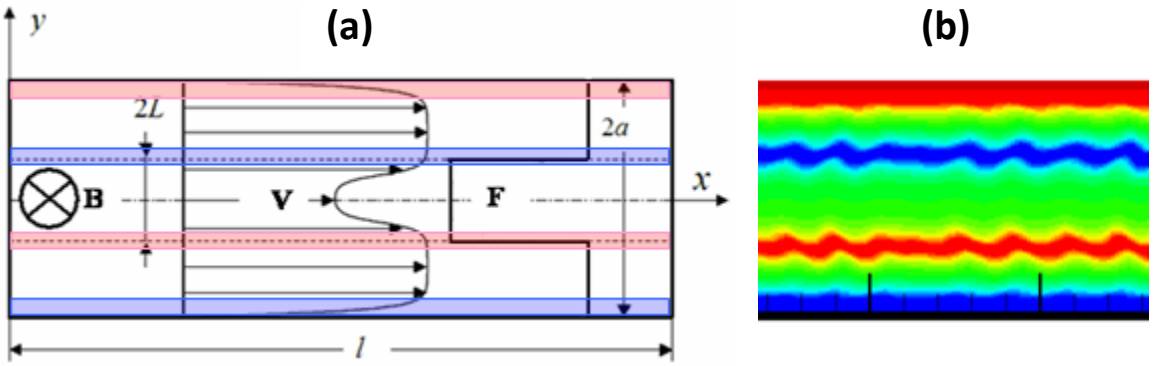

Fig. 3.1: Model MHD problem for a Q2D flow in a rectangular duct with the flow- opposing force: (a) mid-plane flow sketch, and (b) inflectional instability pattern.

A mid-plane sketch of the suggested model Q2D MHD flow in a rectangular duct with insulating walls, whose cross-sectional dimensions are 2*b* in the magnetic field direction and 2*a* in the perpendicular direction, submitted to a strong transverse uniform magnetic field $\mathbf{B}(0,0,B_0)$, is shown in Fig. 3.1. The flow is driven by a pressure gradient and is also opposed by a given volumetric force $\mathbf{F}(-F_x,0,0)$ applied over the whole duct length *l*:

$$F_x = \frac{F_0}{1+\left[\sinh\left(\frac{y}{L}\right)\Big/\sinh(1)\right]^{2m}}. \tag{3.1a}$$

Parameter m in Eq. (3.1a) is responsible for the steepness of the forcing profile, where it changes from zero in the wall region to the constant bulk value F_0 at $y = \pm L$. A particular case of $m \to \infty$ is of special interest as this forcing term turns into a simple piecewise function:

$$F_x = \begin{cases} F_0 & for \quad -L \le y \le L, \\ 0 & for \quad -a \le y < L, \quad L < y \le a \end{cases} \tag{3.1b}$$

as also sketched in Fig. 3.1. The latter is used in analytical derivations of the basic velocity profile, while its counterpart Eq. (3.1a) is utilized in the numerical computations and in the linear stability analysis to avoid singularities at $y = \pm L$. In fact, the reference flow is a plane analog of the flow in the MATUR experiment [66], where a Q2D turbulent flow is enforced in the horizontal cylindrical cell of mercury by the action of a steady vertical magnetic field and an applied voltage between two electrodes. Similar to the MATUR experiment, an additional electromagnetic body force in the reference duct flow can be produced with a couple of line or point electrodes located at each Hartmann wall symmetrically with respect to the duct mid-plane as suggested in Fig. 3.2. In the case of a fully developed undisturbed flow, this electrode configuration will lead to the volumetric flow opposing force resembling that given by Eq. (3.1a) or (3.1b).

The distributions shown in Fig. 3.2 have been computed for illustrative purposes using a finite-volume MHD code [67], which utilizes a mathematical formulation based on the induced magnetic field B'. In the computations, the duct walls are ideally insulating: $dB'/d\tau = 0$, except for the electrodes where the boundary condition is written in the form $dB'/d\tau = \pm Par$, where the distance τ is taken along the wall and the parameter Par of either plus or minus sign is used to

specify the electric current entering or leaving an electrode. In experiments, this parameter can be varied by changing the applied voltage or/and the resistance of the external circuit. Similar to the MATUR experiment, the inflection point in the basic velocity profile appears at the electrode location (Fig. 3.2b). When the suggested parametrical model is used as a mathematical description for such a flow, the electrode location can be varied via the parameter *L*.

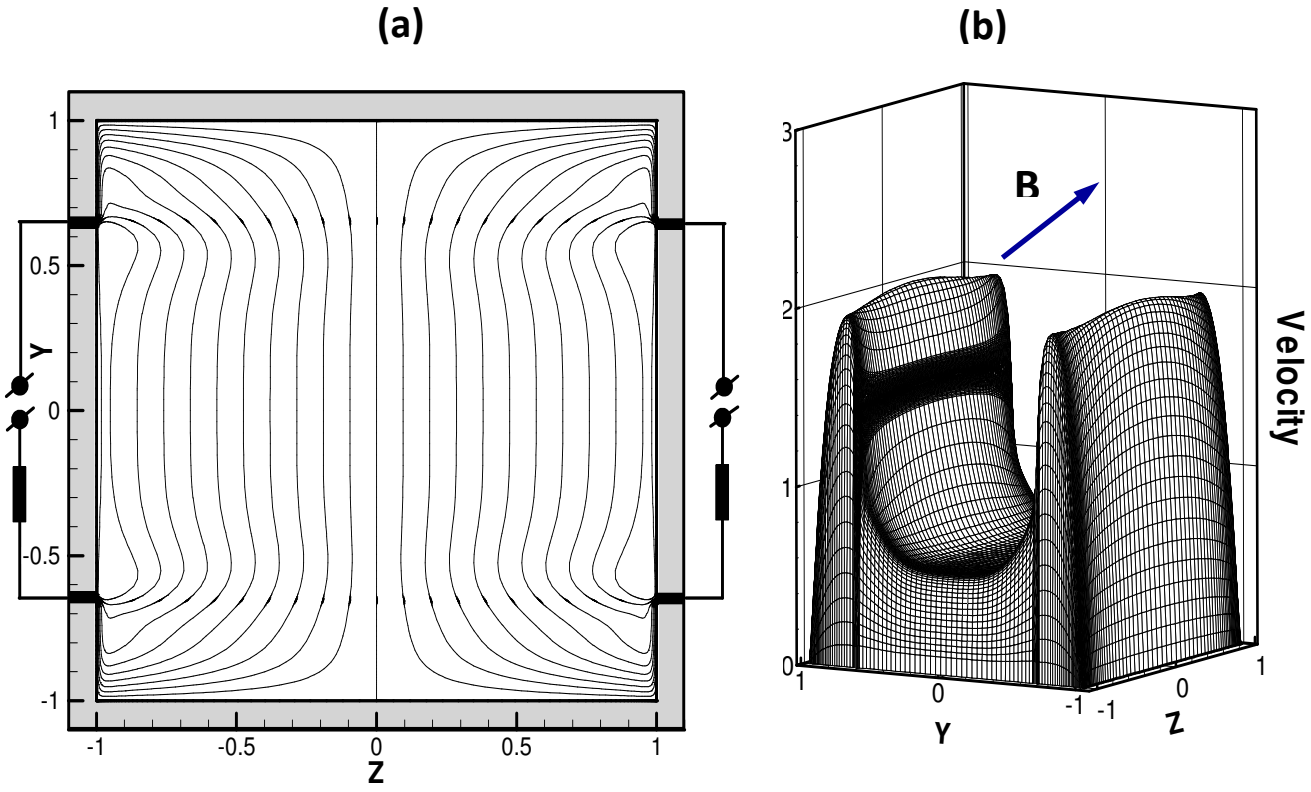

Fig. 3.2. Fully developed laminar MHD flow in a non-conducting duct with the line electrodes in the wall, *Ha*=100: (a) induced electric current distribution, (b) velocity profile.

Once the velocity profile with inflection points is formed, the flow can become unstable (Fig. 3.1b) and eventually turbulent, providing stabilizing effects in the flow due to dissipation losses are smaller compared to the destabilization mechanism. Such a turbulent MHD flow in a strong

magnetic field is described here with the SM82 model [18], which in the conditions of the reference Q2D flow shown in Fig. 3.1 is written in terms of the core flow velocity $\mathbf{V}[U(x,y),V(x,y),0]$ and the pressure $P(x,y)$ using dimensionless variables as follows:

$$\partial_t \mathbf{V} + (\mathbf{V}.\nabla)\mathbf{V} = -\nabla P + \frac{1}{Re}\Delta \mathbf{V} - \frac{Ha}{Re}\left(\frac{a}{b}\right)^2 \mathbf{V} + \mathbf{F}, \tag{3.2}$$

$$\nabla.\mathbf{V} = 0. \tag{3.3}$$

The momentum equation (3.2) includes the classic linear Hartmann damping term as well as the external force **F**. In the particular case of a piecewise forcing term [Eq. (3.1b)] its axial component, being written in the dimensionless form, is as follows:

$$F_x = \begin{cases} \dfrac{1}{Fr} & for \quad -L \le y \le L, \\ 0 & for \quad -1 \le y < L, \quad L < y \le 1. \end{cases} \tag{3.4}$$

In Eqs. (3.2)-(3.4) the half width **a** is used as the length scale, the mean bulk velocity U_m as the velocity scale, a/U_m as the time scale, and ρU_m^2 as a scale for the pressure. The Reynolds number $Re = U_m a/\nu$ and the Froude number $Fr = U_m^2/F_0 a$ are both written through dimension a, while the Hartmann number $Ha = B_0 b\sqrt{\sigma/(\rho\nu)}$ is written through dimension b. The physical properties of the fluid: density, kinematic viscosity and the electrical conductivity, are denoted by ρ, ν and σ.

To derive an analytical solution for the basic flow, the unsteady and convective terms in momentum equation (3.2) are dropped and then the equation is solved separately in the inner (

$F_x \neq 0$) and outer ($F_x = 0$) domains using approximation (3.1b). This solution is given in **Appendix A**. The most distinctive feature of the basic flow solution is that the thickness δ (scaled by dimension a) of the two bulk shear layers at $y = \pm L$ at high Ha is

$$\delta = \frac{2}{\sqrt{Ha\left(\frac{a}{b}\right)^2}} \tag{3.5}$$

which depends only on the square root of the Hartmann number and on the duct aspect ratio a/b, but does not depend on the applied force, Reynolds number and the location of the inflection point. The whole velocity profile, itself, is fully determined by the modified Hartmann number $M = Ha\left(\frac{a}{b}\right)^2$, which controls the thickness of the side and internal shear layers and by two other parameters: the ratio Re/Fr and the distance L, both having a small impact on the side-layer solution. Three M-shaped velocity profiles with distinctive bulk shear layers and associated vorticity distributions are obtained by changing the location of the inflection point as shown in Fig. 3.3. In these three cases, the ratio Re/Fr and the Hartmann number are kept unchanged so that all variations in the basic flow are due to changes in L. These three locations are chosen to depict three particular situations when the inflection point is far from the wall (Fig. 3.3a), close to it (Fig. 3.3c), and about equally distanced from the wall and the duct centerline (Fig. 3.3b). As shown below, the location of the inflection point has a tremendous effect on the onset of instability and also affects the flow dynamics in the non-linear phase.

To conclude this section, we would like to summarize the main properties of the proposed parametrical model. The model mimics a basic symmetric M-shaped velocity profile with the near-wall jet composed of two legs and two inflection points located on the bulk side of the jet.

The width of the undisturbed internal shear layer at the inflection point is scaled as $1/\sqrt{Ha}$. This scaling law is predicted by the laminar theory for a typical MHD free shear layer (e.g. Ref. [66]), for example that in the thin-wall conducting duct flow or in the duct flow with embedded wall

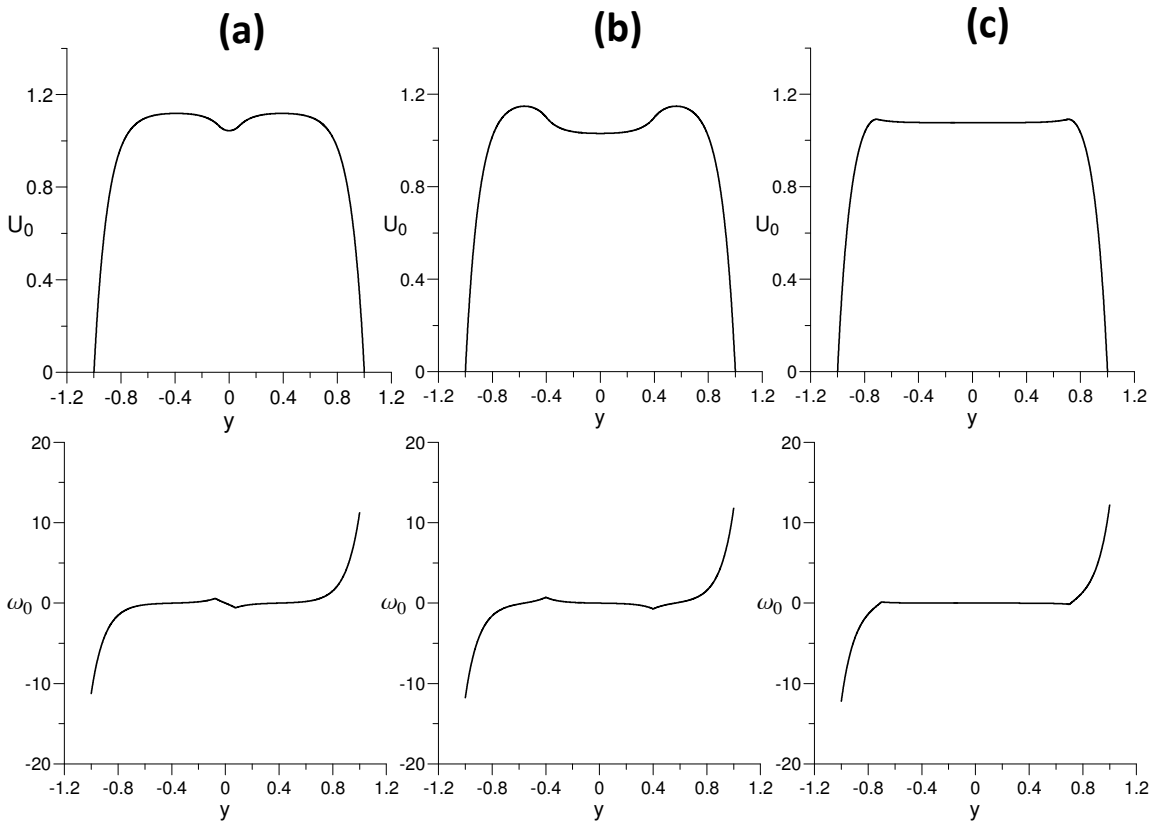

Fig. 3.3: "M-shaped" velocity profiles (top) and vorticity distributions (bottom) in the basic flow at *Ha*=100, *a*/*b*=1 and *Re*/*F*r=15: (a) *L*=0.075, (b) *L*=0.4, (c) *L*=0.7.

electrodes. It also reproduces the exponential near-wall velocity distribution in the Shercliff layers at the side walls. The Hartmann damping effect on the flow associated with the induced electric currents closing in the Hartmann layers is adequately reproduced with the linear friction term on the right-hand-side of Eq. (3.2). As shown, the model is not just a "mathematical toy" but an adequate description of an MHD flow in a rectangular duct with the wall electrodes and in

fact the reference flow, which is described by the model, is a plane analog of the cylindrical cell MHD flow in the MATUR experiment. One of the advantages of the proposed model is that it allows for changing the location of the inflection point via the parameter *L*. In practice, such a change could be made by changing the electrode location on the wall. In thin-wall conducting ducts such a possibility is limited since the basic velocity profile is fully determined by the Hartmann number.

3.2 Linear Stability Analysis

Equations (3.2) and (3.3) are first rewritten using the vorticity ω ($\omega = \frac{\partial V}{\partial x} - \frac{\partial U}{\partial y}$) and the streamfunction ψ ($U = \frac{\partial \psi}{\partial y}, V = -\frac{\partial \psi}{\partial x}$) to eliminate the pressure, and then the time-dependent solution is expanded in normal modes such that

$$[\psi(x,y,t), \omega(x,y,t)] = [\psi_0(y), \omega_0(y)] + [\psi_1(y), \omega_1(y)]\mathbf{e}^{\mathbf{i}(\alpha x - \beta t)}. \tag{3.6}$$

Here, $\psi_0(y), \omega_0(y)$ are the solutions for the basic flow, while $\psi_1(y), \omega_1(y)$ are the infinitesimal amplitudes of the flow perturbations. The wavelength of the disturbance λ is related to the wavenumber α, which is real, as $\lambda = 2\pi/\alpha$. The parameter β as well as the ratio $s = \beta/\alpha$ are complex: $\beta = \beta_{\mathbf{r}} + i\beta_{\mathbf{i}}$ and $s = s_r + is_i$. The real part s_r is the phase velocity of the disturbance in the axial direction. The imaginary part s_i determines whether the perturbation is amplified or damped with time, if $s_i > 0$ or $s_i < 0$, respectively. The forcing term in this analysis utilizes Eq. (3.1a) with the parameter *m* large enough to guarantee that the width of the transitional region at

the inflection point, where the applied volumetric force changes from zero to F_0, is thin enough compared to the shear-layer thickness given by Eq. (3.5). The same approach is used in non-linear computations to avoid singularities at $y = \pm L$.

After substituting solution (3.6) into the linearized streamfunction-vorticity equations and combining them into one, the following fourth order ordinary differential equation is obtained:

$$i\alpha Re\left[(U_0 - s)(\psi_1'' - \alpha^2\psi_1) - U_0''\psi_1\right] = \psi_1^{(IV)} - 2\alpha^2\psi_1'' + \alpha^4\psi_1 - Ha\left(\frac{a}{b}\right)^2(\psi_1'' - \alpha^2\psi_1), \tag{3.7}$$

which, along with the no-slip boundary conditions

$$y = \pm 1 : \psi_1 = \psi_1' = 0, \tag{3.8}$$

constitute an eigenvalue problem for the complex parameter $\mathbf{s}$. For a pure hydrodynamic flow, $Ha = 0$, Eqs. (3.7) and (3.8) transform to the classical OS problem for the plane Poiseuille flow. The main goals of the linear stability analysis are then to find conditions where $s_i = 0$ to determine the stability limit, and to find the wavelength giving the highest amplification rate. It is also useful to derive an equation for the kinetic energy of the pulsating motion, $K = 0.5\left\langle U_1^2 + V_1^2 \right\rangle$ ("$\langle\ \rangle$" denotes averaging), and then to look at production and dissipation terms on its right-hand-side:

$$\frac{\partial K}{\partial t} + U_0\frac{\partial K}{\partial x} + V_0\frac{\partial K}{\partial y} = P_K + D + \varepsilon_\nu + \varepsilon_{Ha}. \tag{3.9}$$

The first term on the right-hand-side of Eq. (3.9) is the production term, the second is diffusion. The two last terms stand for dissipation losses: ε_ν represents viscous dissipation in the bulk flow, while ε_{Ha} ohmic and viscous losses at the Hartmann walls, which are specific to Q2D MHD flows. The two terms P_K and D are either positive or negative while the two dissipation terms are always negative.

A pseudospectral MATLAB code, which eliminates spurious eigenvalues (unphysical, numerically-computed eignvalues with large positive real parts) [68], is used to solve the present OS problem. The code has been validated against available literature results, including linear stability of a plane Poiseuille flow [69] as well as stability of the Hartmann [70] and Shercliff layers [33].

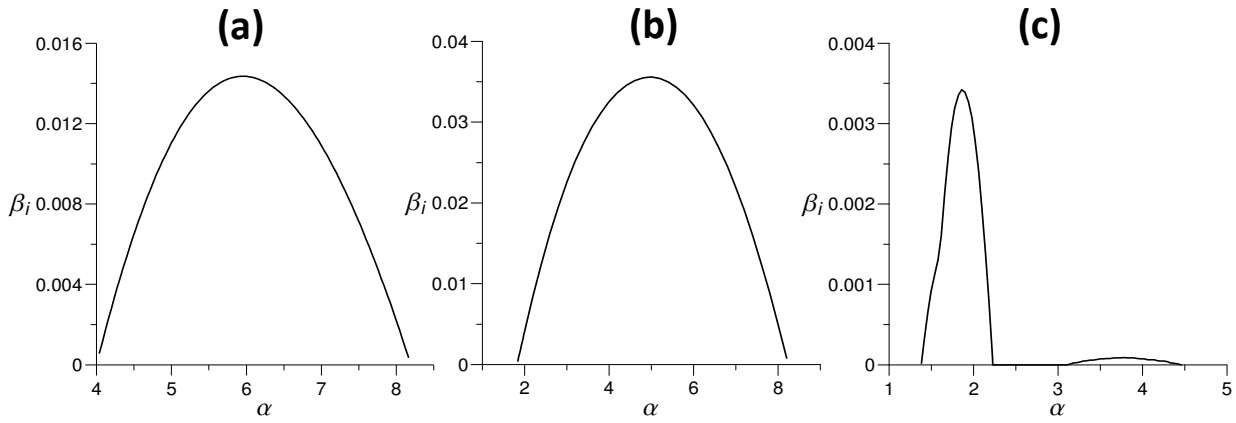

Fig. 3.4: Dispersion curves for three basic flows shown in Fig. 4: (a) L=0.075, Ha=100, a/b=1, Re/Fr=15, Re=2500, (b) L=0.4, Ha=100, a/b=1, Re/Fr=15, Re=4500, (c) L=0.7, Ha=100, a/b=1, Re/Fr=15, Re=450,000.

Linear stability analysis has been performed for the basic flows shown in Fig. 3.3, which all demonstrate the M-shaped velocity profile and associated shear layers, but amongst the three cases both the jet amplitude and the maximum vorticity in the shear layer at the bulk-side leg of

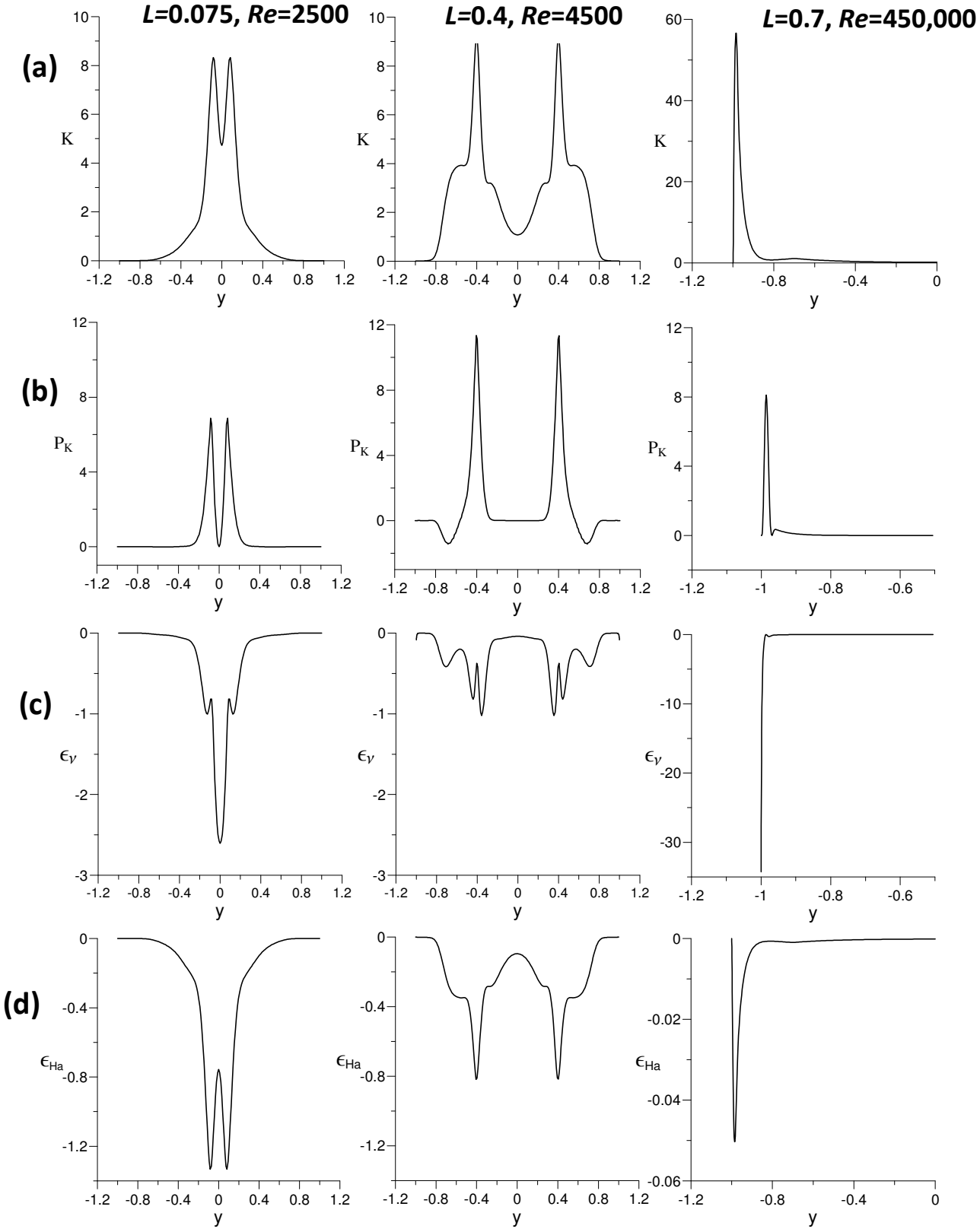

Fig. 3.5: Results of linear stability analysis for the reference MHD flow at Ha=100, a/b=1, Re/Fr=15 for the most amplified instability mode. From top to bottom : (a) kinetic energy, (b) production rate, (c) viscous dissipation, (d) dissipation in the Hartmann layers.

the jet are significantly different. The Reynolds number, which doesn't enter the basic flow solution but enters the equations in the linear analysis, was chosen in each case individually, after many trials, to demonstrate all possible instability modes and associated linearized flow details as observed in the computations. In the analysis, the most amplified instability modes were identified first by plotting the dispersion curves (Fig. 3.4), and then the terms entering Eq. (3.9) were calculated for each case using the wavenumber of the most amplified perturbation (Fig. 3.5). Two basic types of instability and a mixed instability mode have been identified depending on the flow parameters.

The first type is associated with the inflection point and thus represents the well-known Helmholtz-type, inflectional instability. This instability can be observed in the two cases for $L=0.075$ and $L=0.4$, where maximum kinetic energy of the perturbations (Fig. 3.5a) and maximum production of the kinetic energy (Fig. 3.5b) both occur at the location of the inflection points. Another distinctive feature of this instability type is that the two dissipation terms, the viscous dissipation (Fig. 3.5c) and the dissipation in the Hartmann layers (Fig. 3.5d) are comparable in magnitude. In spite of the same instability mechanism, significant qualitative differences can be observed between these two cases, as seen for instance, from the distribution of the production term, which in the case of $L=0.4$ demonstrates positive peaks at the inflection points and two adjacent zones where production of the kinetic energy is negative. In contrast, the case of $L=0.075$, exhibits only positive production over the whole duct width. This difference is further seen in Fig. 3.6, which shows the vorticity distribution of the perturbed motion. In each of the two cases, the observed configuration of the processing vortices is different from the classic von Karman's street as there is more than one row of vortices in the vicinity of each inflection point. The case of $L=0.075$ demonstrates a central row of vortices, plus two

additional rows of adjacent vortices. In the case of $L=0.4$, a row of secondary two-centered vortices appears between the wall and the row of primary vortices. These secondary vortices cannot be explained by instability of the side layer since their centers as well as the negative peak in the production term are both far from the wall. The negative production is consistent with the spin of the secondary vortices and the basic flow velocity gradient (Fig. 3.3). From the physical point of view, negative production can be interpreted as a result of energy transfer from the primary vortices to the surrounding liquid layer causing its instability [71].

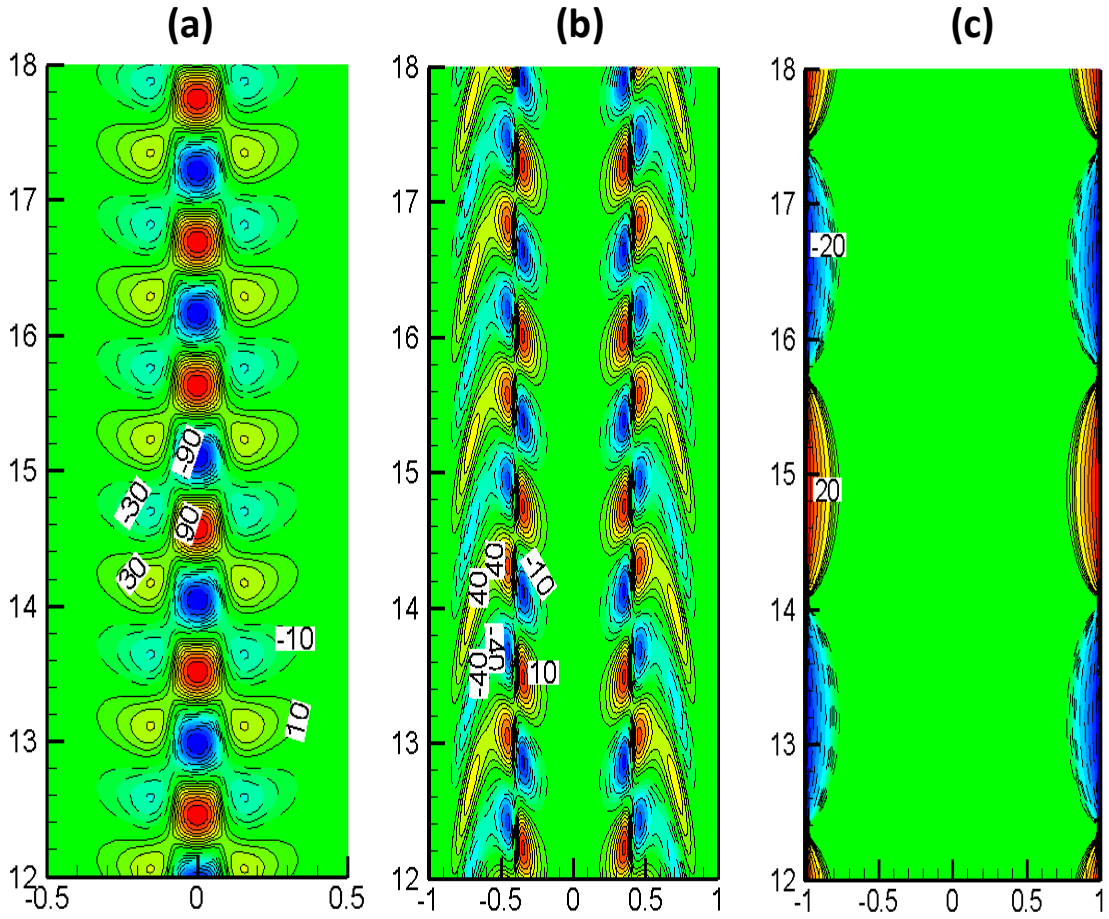

Fig. 3.6: Vorticity distribution in the reference flow based on the linear analysis for the most amplified perturbation mode. There can be either inflectional (a) and (b) or side-layer (c) instability: (a) L=0.075, Ha=100, a/b=1, Re/Fr=15, Re=2500, (b) L=0.4, Ha=100, a/b=1, Re/Fr=15, Re=4500, (c) L=0.7, Ha=100, a/b=1, Re/Fr=15, Re=450,000.

The other instability type is seen in the case of $L = 0.7$ at a much higher Reynolds number, where the flow in the vicinity of the inflection point is stable but a high peak in both the kinetic energy (Fig. 3.5a) and the production term (Fig. 3.5b) occur within the side layer. This type of instability is thus the boundary layer instability associated with the Tollmien–Schlichting waves (see also vorticity distribution in Fig. 3.6c). The other difference with the case of inflectional instability is significantly higher (by a few orders of magnitude) viscous dissipation (Fig. 3.5c) compared to dissipation losses in the Hartmann layer (Fig. 3.5d), which can be explained by the proximity of the vortices to the wall. The two instability types are also indicated on the "flow map" (Fig. 3.7) where the neutral stability curves are plotted in the $\alpha - Re$ plane. The flow inside the zone bounded by the neutral curve on the map is unstable and it is stable outside. The case of $L = 0.7$ exhibits either the side-layer (lower branch of the curve) or inflectional (upper branch) instability, while the other two cases, $L = 0.4$ and $L = 0.075$ demonstrate only the inflectional instability. These neutral stability curves show a very strong effect of the position of the inflection point on the stability threshold as well as dominating instability type. The flow map also suggests that in the certain range of the flow parameters, two instability modes can coexist in the form of a mixed instability mode as seen from Fig. 3.7c. The computed data are also presented in 3D in Fig. 3.8, showing a "neutral surface," above which the flow is linearly unstable. As seen from this figure, the side-layer instability and the mixed instability mode can be observed when the inflection point is close enough to the wall (L is around 0.7).

As the dispersion curves show (Fig. 3.4), the side-layer instability (Fig. 3.4c) is characterized by a smaller wavenumber (larger wavelength) and a significantly smaller amplification rate compared to the inflectional instability (Fig. 3.4a and 3.4b). The difference in the wavelength between the two types of instability for the most amplified perturbations is also seen in Fig. 3.6.

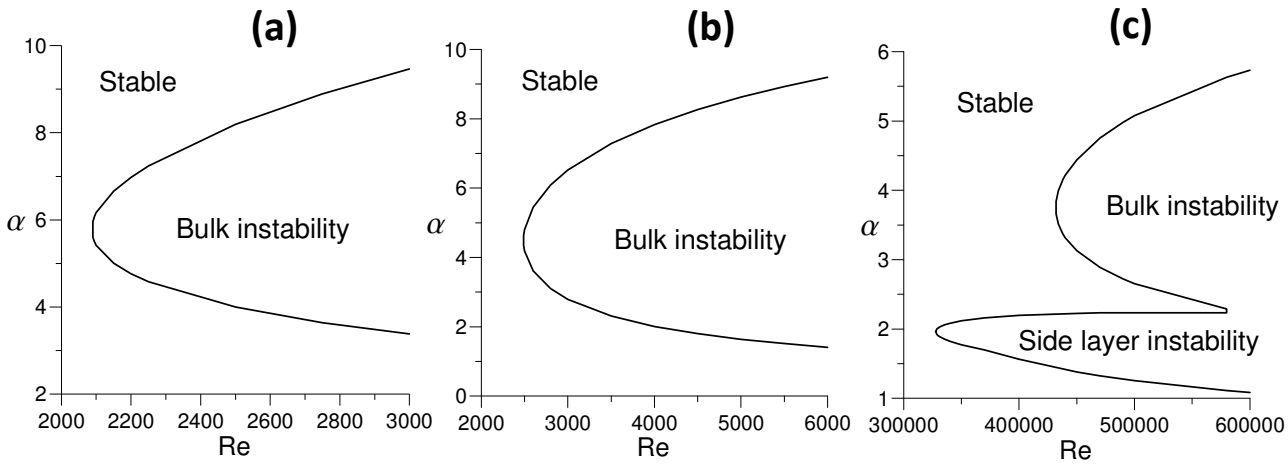

Fig. 3.7: Flow maps (neutral stability curves) at *Ha*=100, *a*/*b*=1, *Re*/*Fr*=15: (a) *L*=0.075, (b) *L*=0.4, (c) *L*=0.7.

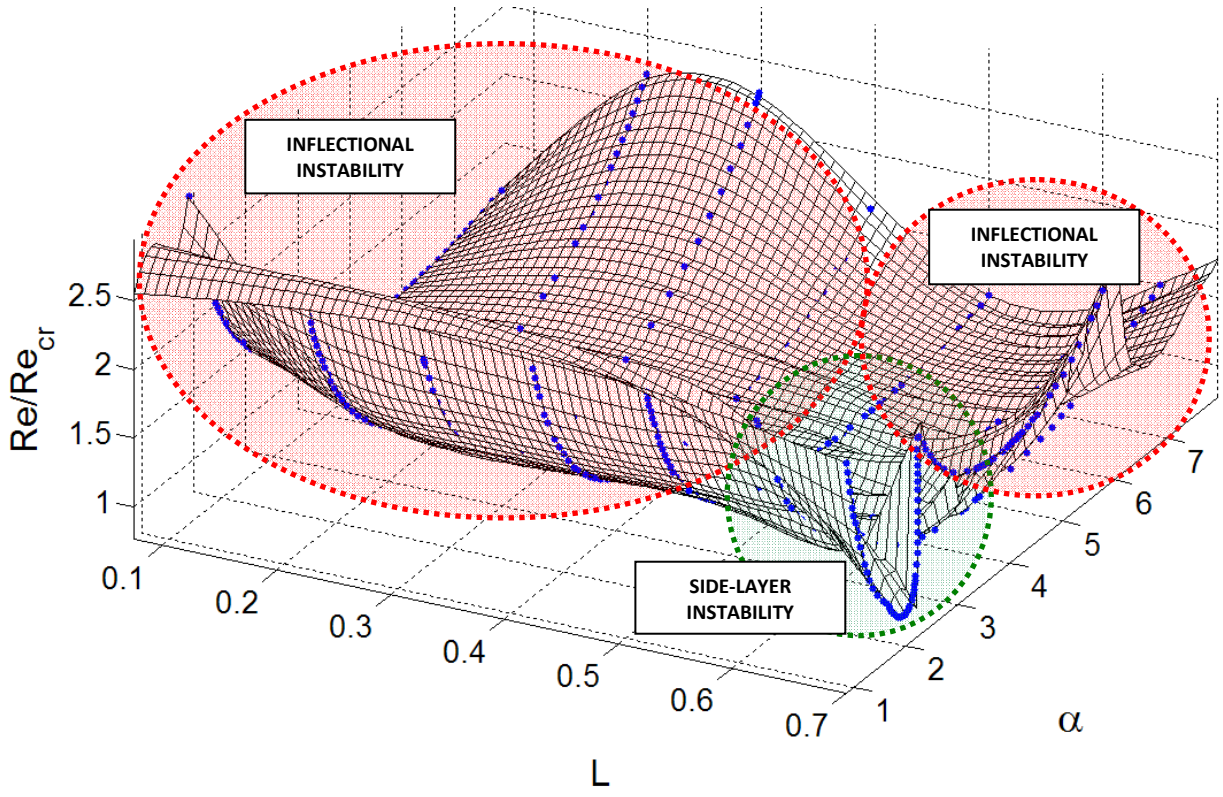

Fig. 3.8: Neutral stability surface at *Ha*=100, *a*/*b*=1, *Re*/*Fr*=15 and 0.05<*L*<0.8. The flow is linearly unstable in the space above the surface.

The flow behavior becomes, however, different from that predicted by the linear analysis, once the flow reaches the nonlinear stage as shown in the next section based on full numerical computations.

3.3 Nonlinear computations

All non-linear results are based on the numerical solution of the full set of the Q2D equations written in the streamfunction-vorticity $\psi-\omega$ form and applying periodic boundary conditions. A computer code solves the equations using a time-marching procedure that extends the standard $\psi-\omega$ approach for hydrodynamic flows (see, *e.g.* Ref. [53]) to the reference case. Since the numerical procedure is standard, only basic ideas are summarized here. The governing equations are approximated with finite-volume formulas on a mesh, which is uniform in the axial and non-uniform in the wall-normal direction. The mesh clusters the points near the wall within the side layers and also in the vicinity of the two inflection points at $y=\pm L$. At least ten points are placed within each side layer and within two internal shear layers, whose thickness based on Eq. (3.5) is scaled as $1/\sqrt{Ha}$. The discretization is of second-order accuracy in time and space. Advancing in time is performed using Adams-Bashfort scheme. Central-difference formulas are used for the discretization of the diffusive terms in both ω- and ψ-equation. For the convective terms in the vorticity transport equation, a conservative scheme proposed by Arakawa [72] is used. This scheme, which conserves the basic quadratic quantities, such as the mean kinetic energy and the mean enstrophy, allows for accurate computations of the non-linear terms in 2D turbulent flows. Periodic boundary conditions are applied at the flow inlet and outlet $x=0,l$, while no-slip boundary conditions are used at the duct walls $y=\pm 1$. Using periodic boundary conditions when solving the elliptic equation for the streamfunction allows for implementation of a direct

algorithm based on the Fast Fourier Transform (FFT), which is much faster and accurate compared to most of the relaxation techniques. On the other hand, the physical reason for using periodic boundary conditions is to avoid flow distortions due to any entry/exit effects, which are not essential for the purposes of the present nonlinear analysis and also to approach conditions of the linear stability analysis, where a plane wave propagates in an infinitely long domain.

The computations have been performed for two Hartmann numbers 100 and 200, the Reynolds numbers ranging from 1800 to 5000, and for several values of L from 0.075 to 0.90 to address the effect of the position of the inflection point on the flow. These choices of Re and Ha are explained by computational limitations, on the one hand and, on the other hand, by limitations of the Q2D model itself, first of all based on the conditions when the Hartmann layer is laminar, *i.e.* when $Re < Re_{cr} = 380Ha$ [73].It seems to be appropriate, however, to extrapolate observed tendencies in the flow behavior to higher values of Re and Ha (for example, those relevant to blanket conditions), providing the major limitations of the Q2D theory are still met. Based on the linear stability analysis, in the chosen range of flow parameters, the only instability mechanism is inflectional instability, while the side layers are predicted to be stable. As shown in the present computations, the flow can demonstrate both linear and non-linear features. The non-linear results are, in fact, very different from those predicted by the linear analysis and involve instabilities both in the bulk-side and wall-side leg of the near-wall jet.

In all computations, the flow domain is as long as $l = 20$, which is sufficiently large to accommodate many wavelengths as computed with the linear stability analysis for the most amplified modes. As a result of mesh sensitivity tests, a 512 (along the flow) by 201 (across the flow) mesh was chosen. Such a mesh resolves all flow details of both the basic velocity profile and the fluctuating motion. The integration time step is also evaluated in several trials by looking

at the characteristic frequency of the fluctuations. Changing Δt within $0.0001 < \Delta t < 0.001$ does not affect the results so that the computations were performed at $\Delta t = 0.0005$. At the initial moment the flow is disturbed by small perturbations imposed on the basic flow streamfunction without disturbing the vorticity field:

$$\psi|_{t=0} = \psi_0(y)[1 + \varepsilon_0 \times RND(x,y)], \quad \omega|_{t=0} = \omega_0(y) \tag{3.10}$$

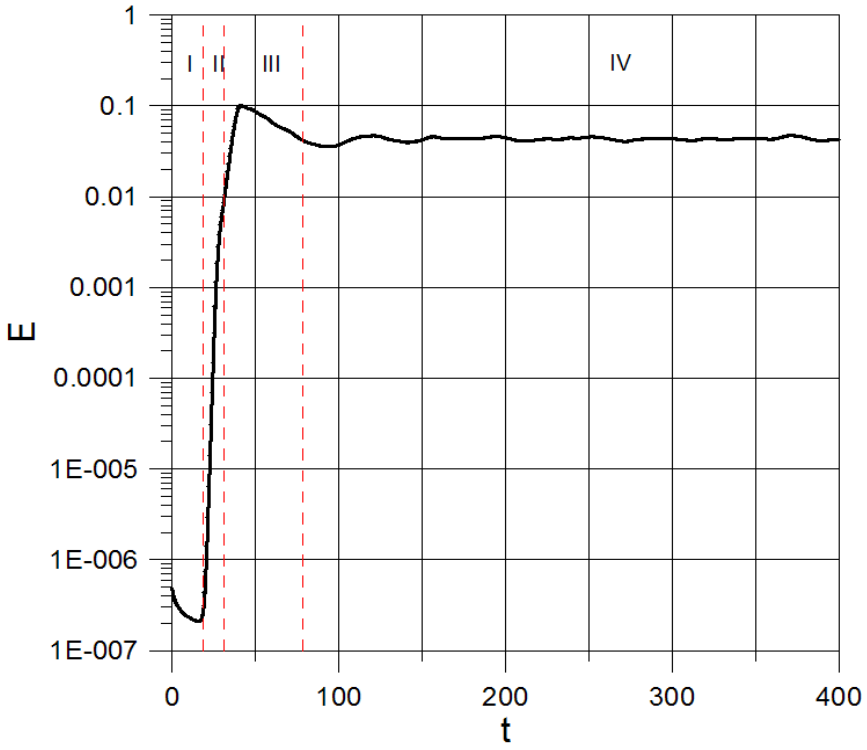

Fig. 3.9: Changes in the kinetic energy of the fluctuating flow versus time at *Ha*=100, *a*/*b*=1, *Fr*=50, *Re*=5000.I – initial phase, II – linear phase, III – transitional phase, IV – nonlinear saturation phase.

Here, the function $RND(x,y)$ generates random numbers in the flow domain in the range from zero to unity, and ε_0 is a small perturbation amplitude. Note that even without disturbing the basic flow, instabilities occur as a result of amplification of small errors, either round-off or

truncation. However, applying initial condition (3.10) allows for faster computations, which are, in some cases, require tens of hours using a PC to reach a nonlinear saturation state. Typical transitions in the flow starting from the initial state given by Eq. (3.10) are shown in Fig. 3.9, where the mean kinetic energy of the whole flow $E(t)=\frac{1}{2l}\int_0^l dx\int_{-1}^{1} 0.5\left[(U-U_0)^2+V_1^2\right]dy$ is plotted versus the computational time.

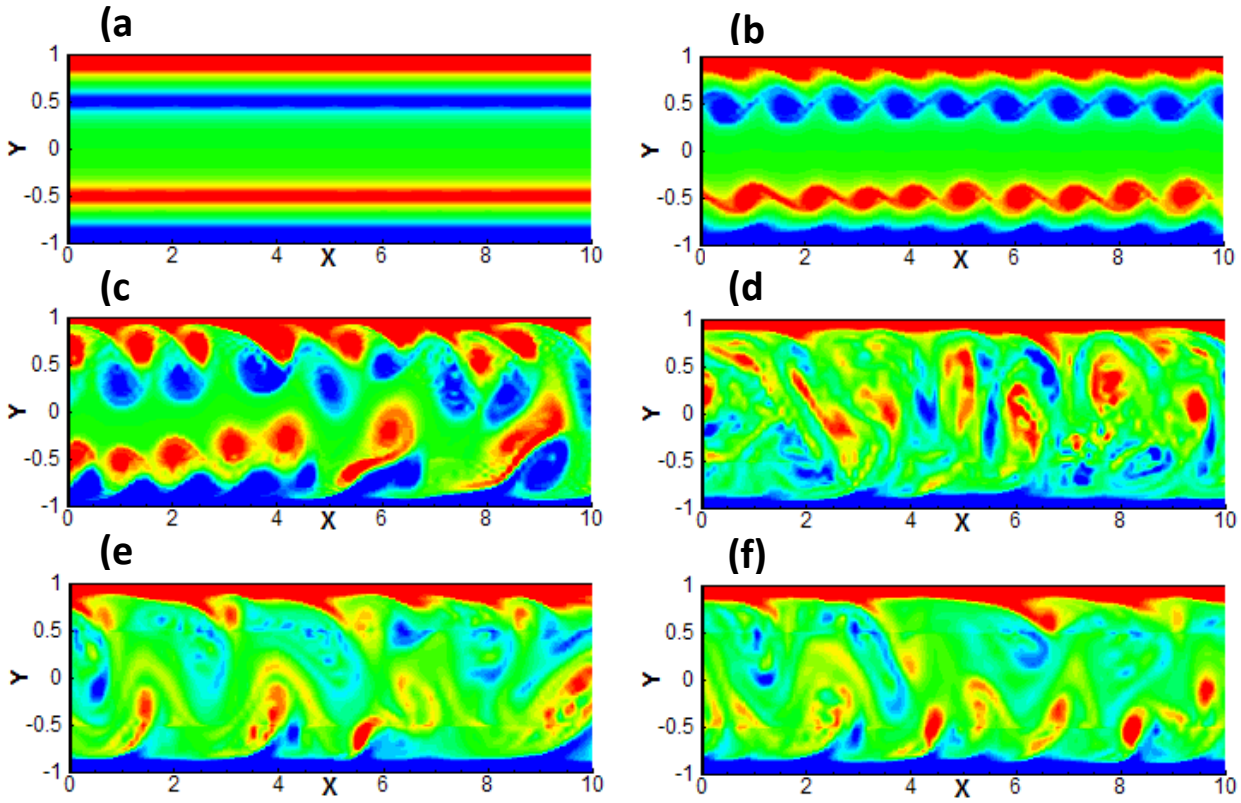

Fig. 3.10: Vorticity snapshots in the reference flow at *Ha*=100, *a*/*b*=1, *Fr*=50, *Re*=5000, *L*=0.5: (a) *t*=20 (initial phase), (b) *t*=28 (linear phase), (c) *t*=37 (early transitional phase), (d) *t*=50 (late transitional phase), (e) *t*=150 and (f) *t*=200 (nonlinear saturation phase).

The supplementary flow snapshots are shown in Fig. 3.10. During a short *initial phase I*, most of the applied random perturbations are damped, such that the total kinetic energy of the fluctuating motion slightly decreases. In the next *linear phase II* the logarithm of *E* increases

linearly with time, indicating exponential growth of perturbations as predicted by the linear theory. In this phase, formation of two rows of isolated vortices occurs from the two shear layers in the bulk-side leg of the near-wall jets.

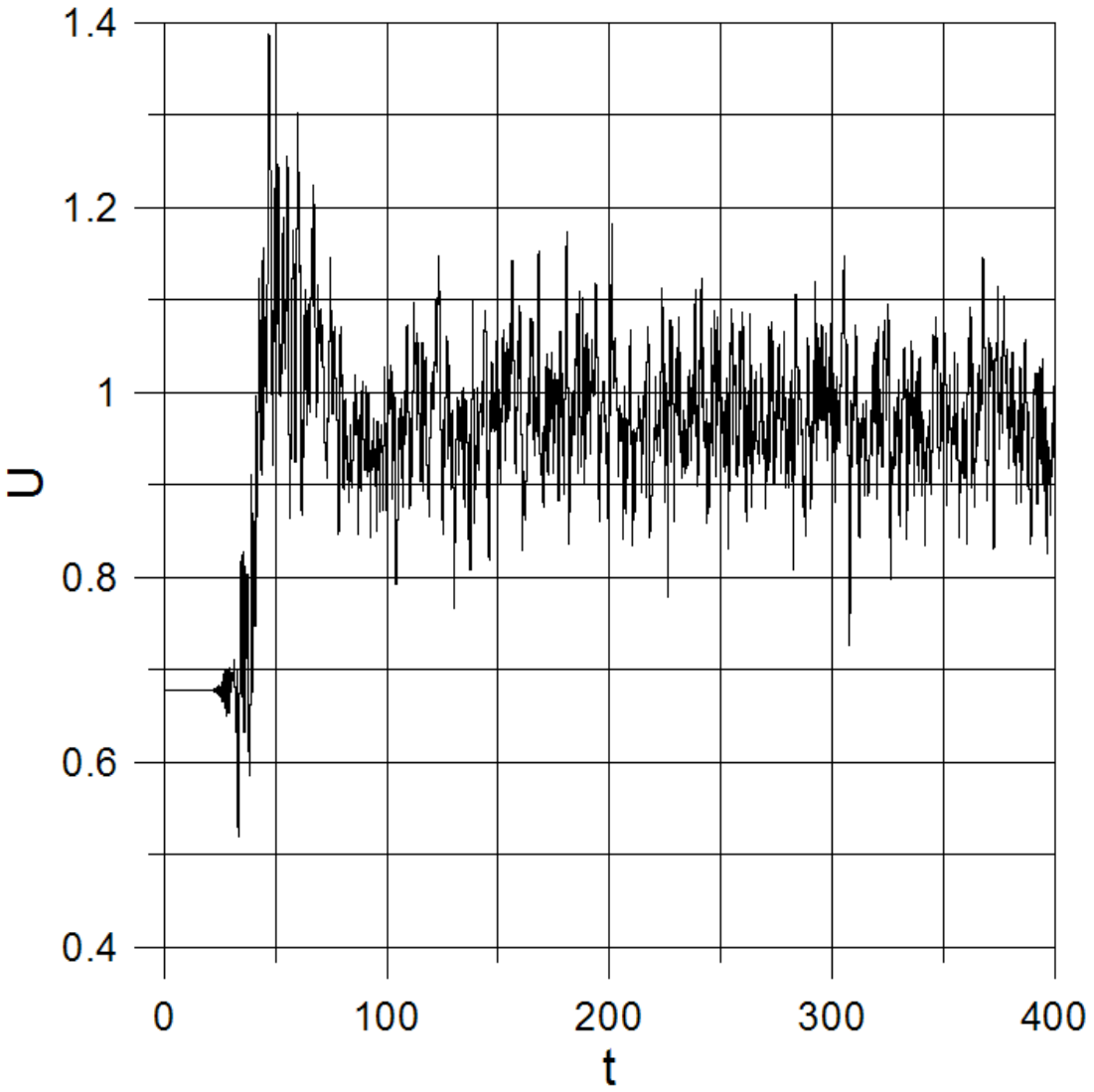

Fig. 3.11: Velocity fluctuations at the duct axis at *Ha*=100, *a*/*b*=1, *Fr*=50, *Re*=5000, *L*=0.5.

There is a good match between the slope of the energy curve in Fig. 3.9 and the growth rate of the most amplified perturbation calculated with the linear theory. Also, the wavelength of the train of processing vortices in Fig. 3.10b is in a good agreement with the results of the linear

analysis. In this phase, all the flow perturbations remain localized within the shear layer region, while the near-wall and bulk flow regions don't experience any significant disturbances. This linear flow behavior in phase II is followed by a *transitional phase III*, where nonlinear effects become more and more pronounced as seen, for example, from various vortex-vortex and vortex-wall interactions. An essential flow feature in this phase is the interaction between the primarily bulk vortices and the side layers, which causes the boundary layer destabilization and eventually their detachment from the wall at several locations along the flow path. Another peculiarity is pairing between the primary vortices, as required by the inverse energy cascade, typical to Q2D turbulent flows. In this non-linear stage, an intensive vortex formation occurs in the bulk-side shear layers and also as a result of the boundary layer detachment. The formed vortices can travel from their original locations across the whole duct, often approaching the opposite wall. Finally, as a result of intensive vortex formation and their interactions, the flow reaches a *nonlinear saturation phase IV*, where energy E remains at about the same level, whereas the flow demonstrates near-periodic behavior in both time and space (Fig. 3.10e and 3.10f). This regime can be considered as a new dynamic equilibrium state in which the averaged flow doesn't vary with time anymore but is very different from that in the linear phase. Among the most distinctive features, here, is the formation of complex vortical structures in the near-wall region, originally occupied by the near-wall jet, that comprise of streaky-like boundary-layer vortices as well as groups of isolated vortices (often paired) of the opposite sign in the flow bulk. The associated wavelength is typically few times larger than the original wavelength of the sinusoidal-like structures in the linear phase. The streaky-like vortices ejected from the wall region, become tangled as they enter the bulk region of the flow. The whole flow becomes

densely populated by vortices of different sizes and opposite spin resulting in completely irregular, Q2D turbulent, flow as indicated in Fig. 3.11.

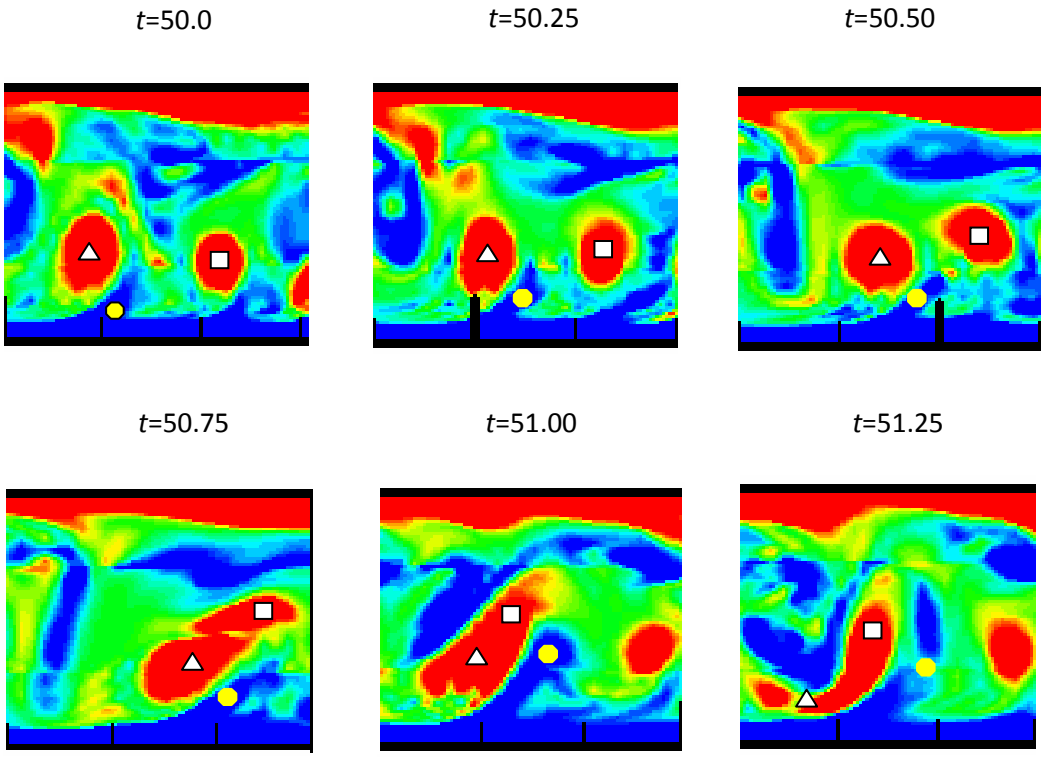

Fig. 3.12: Vortex-vortex and vortex-wall interactions in transitional phase (*phase III*) at Ha = 100, a/b = 1, Fr = 50, Re = 5000, L = 0.4. Two interacting bulk-side vortices of the same sign are marked with Δ and □. A boundary-layer vortex of opposite sign is marked with ⬡ .

The vortex-vortex and vortex-wall interactions, which are important elements of the transition to the nonlinear saturation state, are further illustrated in Fig. 3.12, where the same group of vortices is snapshoot as they move downstream. The vortex-wall interactions [34] are not new in ordinary hydrodynamics but in the specific context of the MHD wall-bounded flows in a strong magnetic field, this phenomenon has not received significant consideration yet. As seen, the interactions between the primary vortices and the near-wall liquid typically involve a

few characteristic stages. The process is initiated first by a local concentration of the vorticity field within the boundary layer as a single bulk vortex or a group of vortices move along the wall. This stimulates rapidly-rising thin spires (streaks) of fluid that ultimately interact strongly with the external flow. These structures typically contain concentrated vorticity and often roll up into new, secondary, vortex structures. These newly-developed vortices can travel far from their original location, interacting with other vortices of the same or opposite sign. When two or more vortices of the same sign are brought together they form a bigger compound vortical structure as also seen in Fig. 3.12.

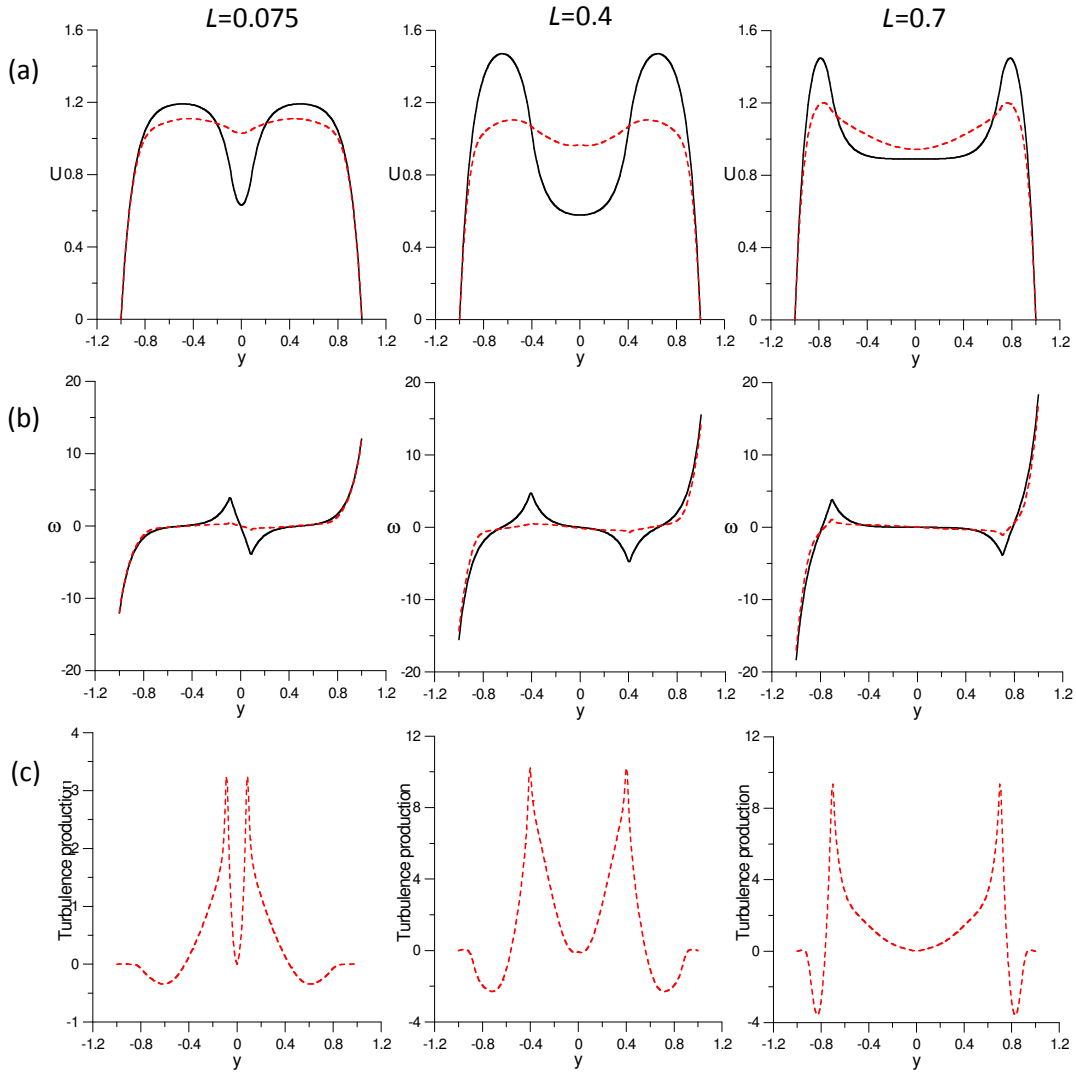

Fig. 3.13: Distribution of basic (solid line) and averaged turbulent (dotted line) flow quantities: (a) axial velocity, (b) vorticity, (c) turbulence production. *Re*=5000, *Ha*=100, *Fr*=50, *a/b*=1.

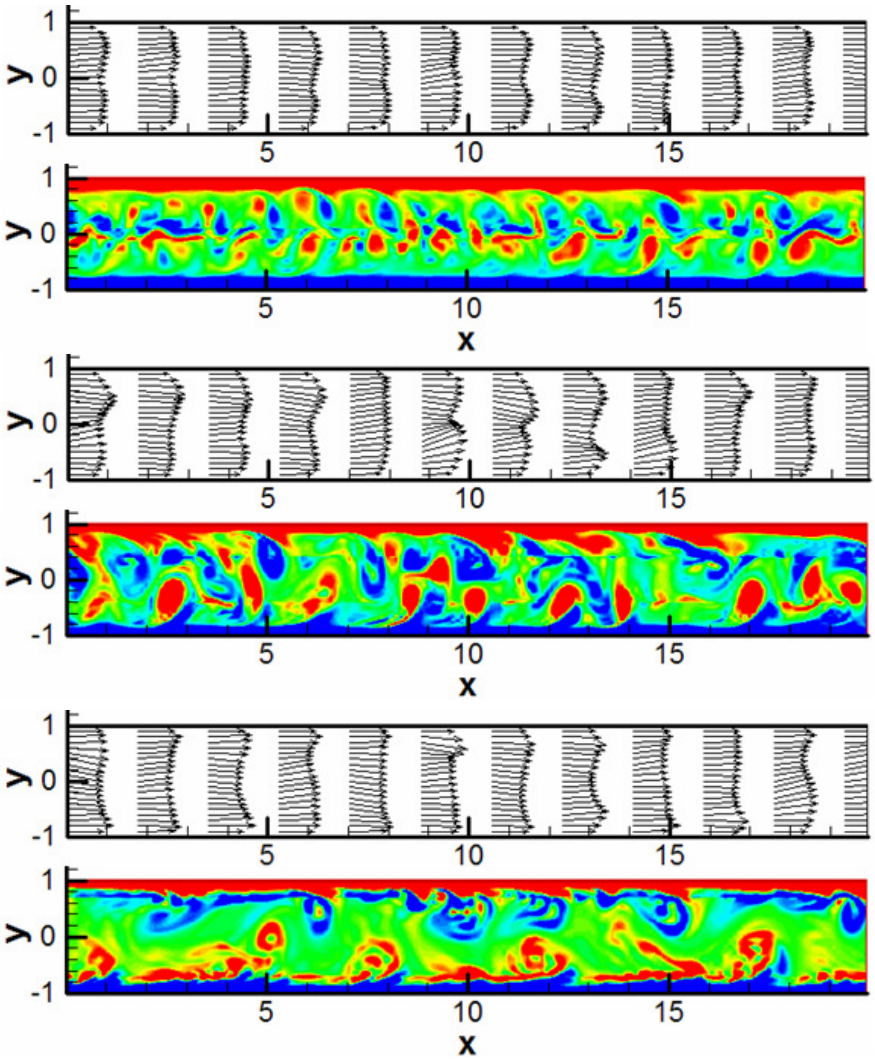

Fig. 3.14: Instantaneous distributions of velocity (upper) and vorticity (lower) at *Ha*=100, *Re*=5000, *a*/*b*=1, *Fr*=50: (a) *L*=0.075, (b) *L*=0.4, (c) *L*=0.7.

More interpretations of the flow in the nonlinear saturation phase are based on the statistically averaged data obtained via the Reynolds decomposition followed by ensemble averaging. Such data are shown in Fig. 3.13 for three locations of the inflection point already introduced in Sec. III, and the supplementary flow snapshots are shown in Fig. 3.14. In all cases, the original velocity profiles experience significant changes, including thickening of the near-wall jet and reduction of its velocity due to intensive formation of new vortices and their transport across the flow. These observations are, however, not new and have been reported in

many experimental papers [40, 41, 49]. One of the important conclusions of the present analysis is thus a demonstration of ability of the suggested Q2D model to reproduce realistically the most important flow features. Amongst new results is the effect of the inflection point location. As shown in the linear analysis, the location of the inflection point has a strong influence on the instability threshold and may even affect the instability mechanism. In the nonlinear phase, this parameter doesn't seem to lead to qualitative changes in the perturbed flow as seen from the distributions of the production term in Fig. 3.13c but quantitative variations are significant. A remarkable feature is a negative turbulence production in the flow sub-region between the wall and the inflection point. This region, as shown above, is a place of special nonlinear effects, where intensive vortex-wall interaction occurs resulting in injections of liquid from the near-wall region and formation of secondary vortices. Similarly with the linear regime, the phenomenon of negative turbulence production can be interpreted in terms of energy transfer from the primary bulk vortices to the near-wall liquid followed by its destabilization. Remarkably, a negative turbulence production can be seen in the earlier experimental data [19] (was not noticed by the authors themselves).

CHAPTER 4

MHD flows with buoyancy forces

4.1 Introduction

In this study we focus on instability and turbulence phenomena in rectangular duct flows of viscous, incompressible, electrically conducting fluid with volumetric heating subject to a strong uniform transverse magnetic field, such that a quasi-two-dimensional (Q2D) flow regime (see, *e.g.*, [18]) is enforced. Such Q2D instabilities and transition to turbulence are likely to occur in conditions of a liquid metal blanket, in particular, in poloidal ducts of the so-called dual-coolant lead-lithium (DCLL) blanket (see, *e.g.*, [1]), where eutectic alloy lead-lithium circulates as breeder/coolant in the presence of a strong plasma-confining magnetic field. The reference flow is sketched in Fig. 4.1, which also shows the volumetric heating profile, the coordinate axes and the direction of the applied magnetic field $\mathbf{B}_0$. Present considerations are limited to vertical upward flows (buoyancy-assisted flows) in a duct with ideally insulating walls, both thermally and electrically. The distribution of the volumetric heat imitates the exponentially decaying heating profile typical to blanket conditions, due to the slowing down of plasma neutrons, in the form:

$$q''' = q_0 e^{-(y+a)/l} \tag{4.1}$$

where a is half of the duct width in the direction perpendicular to the applied field, l is the decay length, and q_0 is the maximum volumetric heating at the "hot" wall y=-a. This distribution of the volumetric heat is responsible for buoyancy forces in the liquid, which result in asymmetric velocity profiles with a higher velocity at the "hot" wall and lower velocity at the "cold" wall y=a as shown in Fig. 4.1. The reference flow is the superposition of a forced flow with the mean bulk velocity U_m and a buoyancy-driven flow, a regime known as a mixed-convection flow. In this regime, the velocity profile has one or more inflection points and thus the flow is subject to Kelvin-Helmholtz (inflectional) instability and eventually can transition to turbulence, which in the reference conditions takes a special Q2D form as described in section 2.5.

4.2 Problem formulation

Present analysis of instabilities and transitions in the reference MHD mixed-convection flow sketched in Fig. 4.1 is based on the idea of a Q2D MHD flow, which in the most complete form is formulated in [18]. In accordance with this concept, a strong magnetic field enforces the liquid motion to occur mostly in the planes perpendicular to the applied magnetic field, while the flow along the magnetic field lines is damped. The important 3D effects are still localized within the thin Hartmann layers at the duct walls perpendicular to the applied magnetic field, where most of the dissipation losses occur. The Q2D turbulent structures appear as columnar-like vortices aligned with the field direction and are subject to an inverse energy cascade. Their intensity is a result of the balance between the Joule and viscous dissipation in the Hartmann layers, on the one hand, and the energy feeding mechanism associated with the instability, on the other hand. Such Q2D eddies can be highly energetic, occupy the whole cross-section of the duct and persist

over many eddy turnovers. In experiments, these striking Q2D properties were first studied in [48] and later in many other laboratory experiments and 3D numerical simulations.

A model for Q2D buoyancy-driven MHD flows for the case when the applied magnetic field is perpendicular to the temperature gradient has been formulated in Ref. [22] and is also adopted here. Providing the applied magnetic field is strong enough, the reference mixed-convection flow is governed by the following four equations (4.2-4.5) written in terms of the bulk velocity

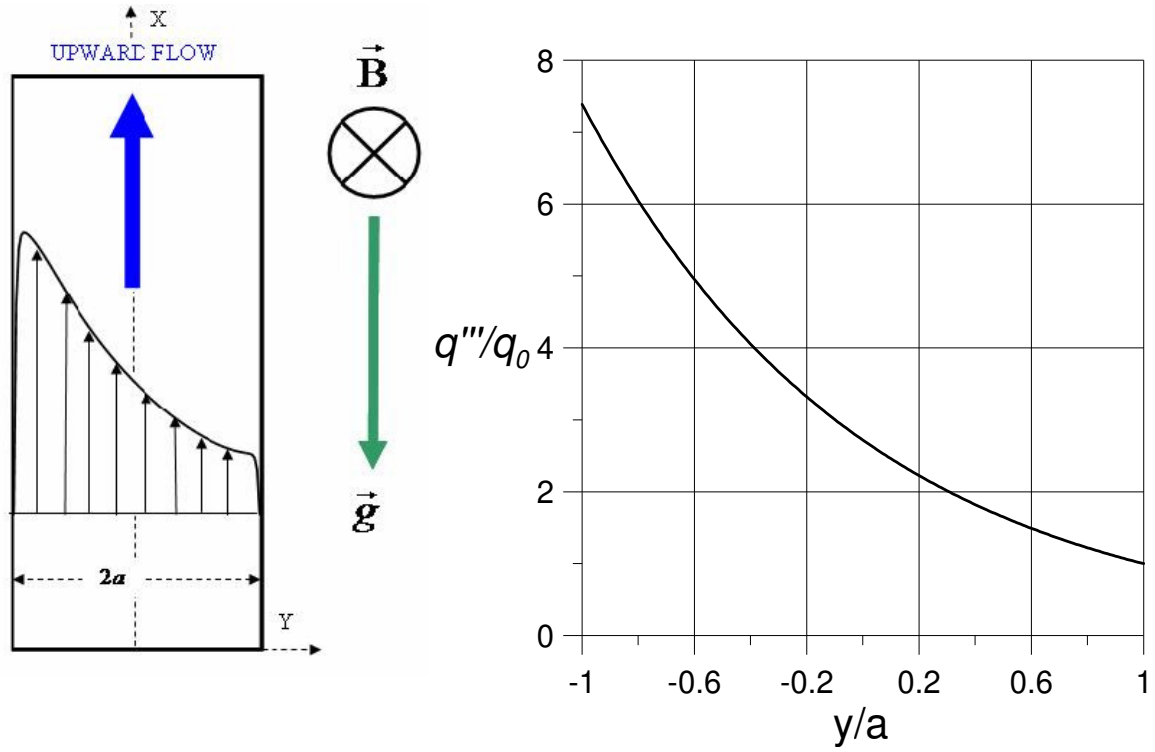

Fig. 4. 1: Sketch illustrating the forced flow direction with respect to the gravity vector and magnetic field (left) and volumetric heating profile (right).

components $U(x,y)$ and $V(x,y)$, pressure $P(x,y)$, and the temperature $T(x,y)$ using the Boussinesq approximation for the buoyant force:

$$\frac{\partial U}{\partial t}+U\frac{\partial U}{\partial x}+V\frac{\partial U}{\partial y}=-\frac{1}{\rho}\frac{\partial P}{\partial x}+\nu\left(\frac{\partial^2 U}{\partial x^2}+\frac{\partial^2 U}{\partial y^2}\right)+g\beta_t\left(T-\overline{T}\right)-g-\frac{U}{\tau}, \tag{4.2}$$

$$\frac{\partial V}{\partial t}+U\frac{\partial V}{\partial x}+V\frac{\partial V}{\partial y}=-\frac{1}{\rho}\frac{\partial P}{\partial y}+\nu\left(\frac{\partial^2 V}{\partial x^2}+\frac{\partial^2 V}{\partial y^2}\right)-\frac{V}{\tau}, \tag{4.3}$$

$$\frac{\partial U}{\partial x}+\frac{\partial V}{\partial y}=0, \tag{4.4}$$

$$\frac{\partial T}{\partial t}+U\frac{\partial T}{\partial x}+V\frac{\partial T}{\partial y}=\frac{\kappa}{\rho c_p}\left(\frac{\partial^2 T}{\partial x^2}+\frac{\partial^2 T}{\partial y^2}\right)+\frac{1}{\rho c_p}q'''. \tag{4.5}$$

Here $\rho,\nu,\sigma,\kappa,c_p,\beta_t$ are the fluid density, kinematic viscosity, electrical conductivity, thermal conductivity, specific heat, and the volumetric thermal expansion coefficient correspondingly, g is the gravitational acceleration, $\overline{T}(x)=\frac{1}{2a}\int_{-a}^{a}T(x,y)dy$ is the mean temperature in the liquid, and $\tau=bB_0^{-1}(\rho/\sigma\nu)^{1/2}$ is the so-called "Hartmann braking time" [18], which is a time-scale of vortex damping due to ohmic and viscous losses in the Hartmann layers. The dimension b is half of the duct width in the direction of the applied magnetic field. The five dimensionless parameters that characterize the problem are: the Hartmann number $Ha=B_0 b\sqrt{\frac{\sigma}{\rho\nu}}$ (Hartmann number squared is the ratio of the electromagnetic to viscous force), the hydrodynamic Reynolds number $Re=\frac{U_m a}{\nu}$ (the ratio of the inertia to viscous force), the Grashof number $Gr=\frac{g\beta_t\Delta T a^3}{\nu^2}$ (represents the ratio of the buoyancy to viscous force), the duct aspect ratio a/b and the Prandtl number $Pr=\rho\nu c_p/\kappa$. Three more dependent parameters are also used: the interaction parameter (Stuart number) $N=Ha^2/Re$, the Peclet number $Pe=RePr$ and the Rayleigh number $Ra=GrPr$. The

temperature scale is defined here through the average volumetric heating $\overline{q} = (2a)^{-1} \int_{-a}^{a} q'''(y) dy$ as $\Delta T = \overline{q} a^2 / \kappa$. The applicability of this model to unsteady vortical MHD flows generally depends on the difference between the time needed to establish two-dimensionality and the characteristic eddy turnover time. Generally, transition from 3D to Q2D flow occurs if the magnetic field is strong enough. For forced convection MHD flows, this requires $N >> 1$ (Ref. [18]), and for natural-convection MHD flows the requirement is $Ha^2 > 4\sqrt{Gr}$ as suggested in Ref. [22]. One more limitation is related to the Hartmann layer, which is required to be laminar to assure a simple exponential velocity distribution near the wall adopted in the model. In accordance with the experimental data in Ref. [17], the Hartmann boundary layer remains laminar providing *Ha/Re*>150-250. In all non-linear DNS-type computations shown below in Section V, the goal was to keep all the parameters in the range where the Q2D model is valid. The dominance of Q2D flow dynamics in the reference flow was also directly confirmed for several combinations of *Ha*, *Re* and *Gr* numbers via comparisons with the full 3D numerical solutions in Ref. [74].

4.3 Basic flow solution

In a fully-established mixed-convection flow, the velocity component V is zero and both the pressure and the velocity component U are independent of the cross-axial coordinate *y*, so that the mathematical model can further be simplified by decomposing the temperature field into the mean $\overline{T}(x)$ and cross-axial $\theta(\mathbf{y})$ components:

$$T(x, y) = \overline{T}(x) + \theta(y). \tag{4.6}$$

In turn, the mean temperature can be deduced from the global energy balance in the flow as $\overline{T}(x) = T_0 + \frac{\overline{q}}{\rho c_p U_m} x$, where T_0 is the temperature at the flow inlet at $x = 0$. In addition, the pressure term can be written as

$$P(x) = P_0 - \rho(G + g)x, \tag{4.7}$$

where P_0 is the inlet pressure and G is a constant, which needs to be determined. After substitution of Eqs. (4.6) and (4.7) into Eqs. (4.2) and (4.5), the two equations can be combined into one forth-order ordinary differential equation as follows:

$$\theta^{IV} - Ha\left(\frac{a}{b}\right)^2 \theta'' + \frac{Gr}{Re}\theta = -G_* + \frac{2m}{1-e^{-2m}} e^{-m(y+1)} \left[Ha\left(\frac{a}{b}\right)^2 - m^2 \right]. \tag{4.8}$$

Equation (4.8) is written in a dimensionless form, using ΔT as a temperature scale and the duct dimension a as a length scale. Here, $G_* = Ga^2/(vU_m)$ and $m = a/l$ are also dimensionless. Once the temperature $\theta(y)$ is known, the velocity can be found using the following formula:

$$U = \theta'' + \frac{2m}{1-e^{-2m}} e^{-m(y+1)}, \tag{4.9}$$

where U_m is used as a velocity scale. The boundary conditions come from the no-slip and ideal thermal insulation conditions:

$$\theta'\big|_{y=\pm 1} = 0,\ \theta''\big|_{y=-1} = -\frac{2m}{1-e^{-2m}},\ \theta''\big|_{y=+1} = -\frac{2m}{1-e^{-2m}}e^{-2m}. \tag{4.10}$$

4.3.1 Full solution

In accordance with the common theory, a general solution for Eq. (4.8) is of the form:

$$\theta(y) = -\frac{Re}{Gr}G_* + \frac{2m/\left(1-e^{-2m}\right)\left[Ha(a/b)^2 - m^2\right]}{m^4 - Ha(a/b)^2 m^2 + Gr/Re}e^{-m(y+1)} + \sum_{i=1}^{4} A_i f_i(y+1). \tag{4.11}$$

In this solution, the two first terms represent a particular solution, while f_i (i=1-4) are linearly-independent solutions of the uniform equation obtained from Eq. (4.8). The four coefficients A_i need to be found from boundary conditions (4.9). In turn, the four solutions f_i depend on the roots of the biquadratic characteristic equation:

$$\lambda^4 - Ha\left(\frac{a}{b}\right)^2 \lambda^2 + \frac{Gr}{Re} = 0. \tag{4.12}$$

The roots themselves depend on the sign of the discriminant $D = Ha^2\left(\frac{a}{b}\right)^4 - 4\frac{Gr}{Re}$, which is built of two characteristic length scales: $1/\sqrt{Ha}$ stands for the dimensionless thickness of the side

layer in a purely MHD flow, and $(Re/Gr)^{1/4}$ characterizes the thickness of the boundary layer in a mixed-convection flow without a magnetic field. In the case $D>0$, all roots are real:

$$\lambda_{1,2}=\pm\left[\frac{1}{2}\left(Ha\left(\frac{a}{b}\right)^2+\sqrt{Ha^2\left(\frac{a}{b}\right)^4-4\frac{Gr}{Re}}\right)\right]^{1/2},\ \lambda_{3,4}=\pm\left[\frac{1}{2}\left(Ha\left(\frac{a}{b}\right)^2-\sqrt{Ha^2\left(\frac{a}{b}\right)^4-4\frac{Gr}{Re}}\right)\right]^{1/2},$$

so that $f_1=e^{\lambda_1(y+1)}$, $f_2=e^{\lambda_2(y+1)}$, $f_3=e^{\lambda_3(y+1)}$, $f_4=e^{\lambda_4(y+1)}$. In the case $D = 0$, there are two double real roots $\lambda_{1,2}=\pm\sqrt{\frac{Ha}{2}}\frac{a}{b}$ and the four solutions are: $f_1=e^{\lambda_1(y+1)}$, $f_2=e^{\lambda_2(y+1)}$, $f_3=(y+1)e^{\lambda_1(y+1)}$, $f_4=(y+1)e^{\lambda_2(y+1)}$. In the case $D < 0$, there are four complex roots $\lambda_{1,2}=\alpha\pm i\beta\beta\,\lambda_{3,4}=-\alpha\pm i\beta\ell$ where $\alpha=\sqrt{\frac{1}{4}Ha(a/b)^2+\frac{1}{2}\sqrt{Gr/Re}}$, $\beta=\sqrt{\frac{4\,Gr/Re-Ha^2\,(a/b)^4}{8\sqrt{Gr/Re}+4Ha(a/b)^2}}$, so that

$$f_1=e^{\lambda_1(y+1)}cos[\beta_1(y+1)],\ f_2=e^{\lambda_1(y+1)}sin[\beta_1(y+1)],$$
$$f_3=e^{\lambda_2(y+1)}cos[\beta_2(y+1)],\ f_4=e^{\lambda_2(y+1)}sin[\beta_2(y+1)].$$

The coefficients A_i have been evaluated using Wolfram's Mathematica [75] and the constant G_* (not shown here) is calculated using the condition $\int_{-a}^{a}\theta(y)dy=0$.

4.3.2 Approximate solution

At high Hartmann numbers Eq. (4.7) can be simplified by neglecting the fourth-order derivative θ^{IV}. Based on the relation between U and θ [see Eq. (4.9)] neglecting this derivative is

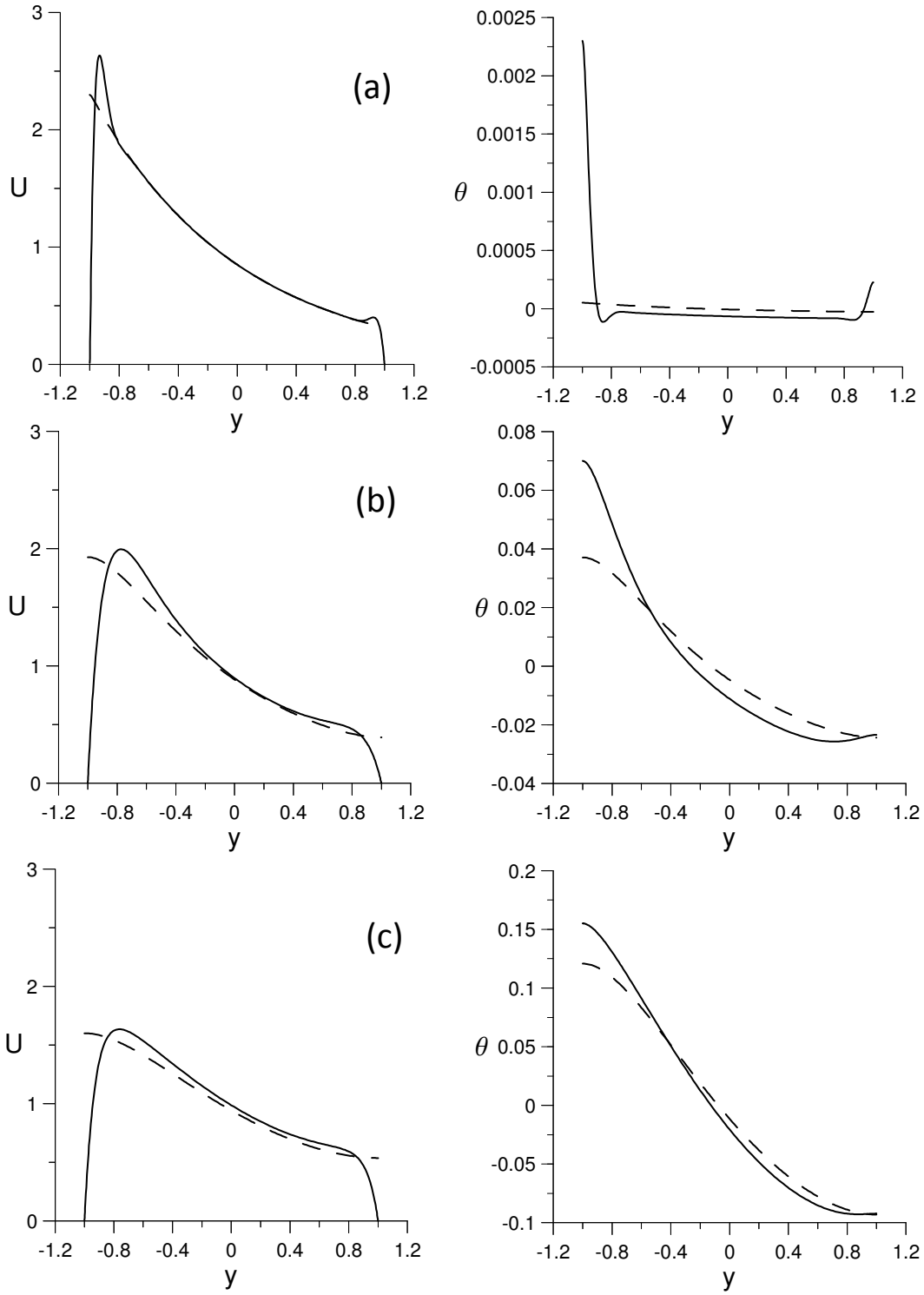

Fig. 4.2: Comparison of velocity and temperature profiles calculated with the full (solid line) and simplified (dashed line) solutions: (a) $D << 0$: Ha=40, Gr =10^9, Re =1000, r=158.1; (b) $D = 0$: Ha = 100, Gr = 2.5x10^7, Re = 10,000, r=5; and (c) $D >> 0$: Ha = 200, Gr = 10^7, Re = 10,000, r=2.23.

equivalent to neglecting the second derivative U'' in the momentum equation. The physical reason for dropping these terms is the small thickness of the side-wall boundary layer such that the flow rate carried by the boundary layer is insignificant compared to the bulk flow, and also due to the fact that the viscous friction here is negligible compared to that in the Hartmann layer. Solving the obtained simplified problem is straightforward:

$$\theta(y)=\frac{2m^2}{r\left(r^2-m^2\right)\left(1-e^{-2m}\right)}\left(\frac{e^{-2m}cosh\left[r\left(y+1\right)-cosh\left[r\left(y-1\right)\right]\right]}{sinh\left(2r\right)}\right)+\frac{2me^{-m(y+1)}}{\left(r^2-m^2\right)\left(1-e^{-2m}\right)}-\frac{1}{r^2}, \quad (4.13)$$

$$U(y)=1+r^2\theta(y) \quad (4.14)$$

It is notable that the approximate solution includes only two dimensionless parameters: $r=\sqrt{\frac{Gr}{HaRe(a/b)^2}}$, and m. The shape parameter m affects the steepness of the heating profile. In the blanket conditions it is fully determined by the interaction of neutrons with the liquid metal. Parameter r is more related to the liquid metal flow itself as it carries information on the contribution of various forces acting on the flow. In the particular DCLL blanket design, $m\approx 1$ and r=5-40 (Ref. [1]). These values are used in all further computations. Also, a/b=1 is assumed in all computations. In accordance with the obtained solution, higher velocity occurs at the hot wall, where volumetric heating reaches its maximum, often in the form of a high-velocity near-wall jet. The difference between the maximum velocity at the hot wall U_{max} and the minimum one at the cold wall U_{min} increases with $\mathbf{r}$ approaching the asymptotic value when $\mathbf{r} >> 1$:

$$U_{max}-U_{min}=2m \quad (4.15)$$

Typical velocity and temperature profiles calculated with the full and simplified solutions are shown in Fig. 4.2 for three special cases: $D>>0$, $D=0$ and $D<<0$. If $D>>0$, the solution in the near-wall region is dominated by the exponential term $\mathbf{e}^{\sqrt{\mathbf{Ha}}(\mathbf{a/b})(\mathbf{y}+1)}$, which represents the well-known distribution in the MHD Shercliff layer. In this case, distinctive Shercliff layers can be seen with the thickness scaled as $1/\sqrt{Ha}$. In the bulk, the velocity and the temperature both drop in a similar manner. The velocity profiles demonstrate two inflection points located in the flow bulk. In the opposite case $D<<0$, the solution near the wall is described by the exponential term $e^{0.5\sqrt{2}(Gr/Re)^{1/4}(y+1)}$ such that the thickness of the boundary layer is scaled as $(Re/Gr)^{1/4}$. In this case, a distinctive high-velocity jet can be seen near the hot wall and a smaller jet near the cold wall. The number of inflection points in this case can vary from 2 to 6. The major inflection point, where the vorticity is maximum, is always located on the bulk-side leg of the larger jet. The temperature profile demonstrates an almost flat distribution in the bulk and two asymmetric peaks near the walls. The case $D=0$ demonstrates intermediate features between the cases $D<<0$ and $D>>0$. Taking into account that the nature of the boundary layer is not necessarily fully controlled by MHD effects, in what follows we will refer to this layer as just a boundary layer or a side-wall boundary layer rather than side or Shercliff layer, which applies to purely MHD flows. In all three cases, there is a fair match between the simplified and the full solutions in the bulk. This allows for using the simplified solution for a kind of express analysis since it is much more compact compared to the lengthy full solution. The importance of the simplified solution is also in a reduction of four dimensionless parameters into one dimensionless group *r*.

The location of the major inflection point *d* where the vorticity is maximum with respect to the wall and associated maximum vorticity $\omega_{\max}$ are of particular interest since these two parameters can affect flow stability and, as shown in Ref. [76], be responsible for the transition

scenario. The associated data are plotted in Fig. 4. 3 to illustrate the effect of *Gr*, *Re* and *Ha*. The increase in *Re* results in shifting the inflection point from the wall towards the axis and reduces the vorticity. The effect of the Hartmann number on vorticity is similar. The position of the inflection point itself is however only slightly affected by *Ha*. Increasing the Grashof number results in a significant increase of vorticity while the inflection point moves from the axis vicinity towards the wall.

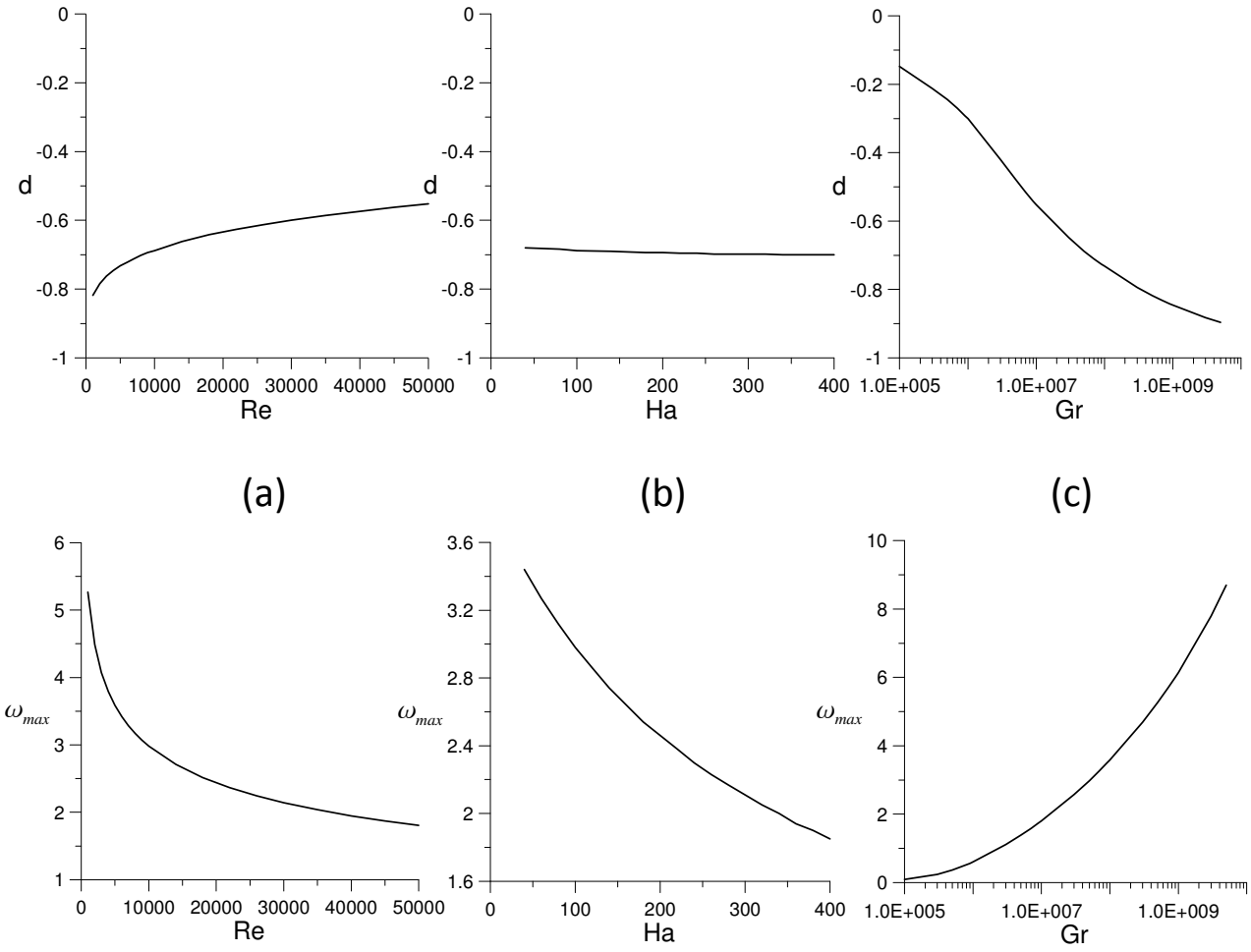

Fig. 4. 3: Effect of the flow parameters on the location of the major inflection point (top row) and the vorticity (bottom row): (a) effect of *Re*: *Ha* = 100, *Gr* = 10^8; (b) effect of *Ha*: *Gr* = 10^8, *Re* = 10,000; and (c) effect of *Gr*: *Ha* = 100, *Re* = 5000.

4.4 Linear Stability analysis

Equations (4.2), (4.3) and (4.5) are changed to the equivalent form using the vorticity ω ($\omega = \frac{\partial V}{\partial x} - \frac{\partial U}{\partial y}$), the streamfunction ψ ($U = \frac{\partial \psi}{\partial y}, V = -\frac{\partial \psi}{\partial x}$) and the cross-axial temperature θ $\left(\theta = T - \bar{T}\right)$. Written in a dimensionless form, these equations are as follows:

$$\frac{\partial \omega}{\partial t} + \frac{\partial \psi}{\partial y}\frac{\partial \omega}{\partial x} - \frac{\partial \psi}{\partial x}\frac{\partial \omega}{\partial y} = \frac{1}{Re}\left(\frac{\partial^2 \omega}{\partial x^2} + \frac{\partial^2 \omega}{\partial y^2}\right) - \frac{Ha}{Re}\left(\frac{a}{b}\right)^3 \omega - \frac{Gr}{Re^2}\frac{\partial \theta}{\partial y}, \tag{4.16}$$

$$\frac{\partial^2 \psi}{\partial x^2} + \frac{\partial^2 \psi}{\partial y^2} = -\omega, \tag{4.17}$$

$$\frac{\partial \theta}{\partial t} + \frac{\partial \psi}{\partial y}\frac{\partial \theta}{\partial x} - \frac{\partial \psi}{\partial x}\frac{\partial \theta}{\partial y} = \frac{1}{RePr}\left(\frac{\partial^2 \theta}{\partial x^2} + \frac{\partial^2 \theta}{\partial y^2} - U\right) + \frac{1}{RePr}\frac{2m}{1 - e^{-2m}}e^{-m(y+1)} \tag{4.18}$$

The time-dependent solution can be expanded in normal modes such that

$$[\psi(x,y,t), \omega(x,y,t), \theta(x,y,t)] = [\psi_0(y), \omega_0(y), \theta_0(y)] + [\psi_1(y), \omega_1(y), \theta_1(y)]e^{i(\alpha x - \beta t)} \tag{4.19}$$

Here, $\psi_0(y), \omega_0(y), \theta_0(y)$ are the basic solutions, while $\psi_1(y), \omega_1(y), \theta_1(y)$ are the infinitesimal amplitudes of the perturbations. The wavelength of the disturbance λ is related to the wavenumber α, which is real, as $\lambda = 2\pi/\alpha$. The parameter β as well as the ratio $s = \beta/\alpha$ are complex: $\beta = \beta_r + i\,\beta_i$ and $s = s_r + is_i$. The real part s_r is the phase velocity of the disturbance in the axial direction. The imaginary part s_i determines whether the perturbation is amplified or damped with time, if $s_i > 0$ ($\beta_i > 0$) or $s_i < 0$ ($\beta_i < 0$), respectively. After substituting solution

(4.19) into the linearized streamfunction-vorticity-energy equations, the following two ordinary differential equations are obtained:

$$i\alpha Re\left[(U_0 - s)(\psi_1'' - \alpha^2\psi_1) - U_0''\psi_1\right] = \psi_1^{(IV)} - 2\alpha^2\psi_1'' + \alpha^4\psi_1 - Ha\left(\frac{a}{b}\right)^2(\psi_1'' - \alpha^2\psi_1) - \frac{Gr}{Re}\theta', \tag{4.20}$$

$$i\alpha\alpha ReP\left[(U_0 - s)\theta_1 - \theta_0'\psi_1\right] = \theta_1'' - \alpha^2\theta_1 - \psi_1'. \tag{4.21}$$

which along with the no-slip and thermal insulation boundary conditions

$$y = \pm 1 : \psi_1 = \psi_1' = \theta_1' = 0 \tag{4.22}$$

constitute an eigenvalue problem for the complex parameter s. For a pure hydrodynamic isothermal flow Eqs. (4.20-4.22) transform to the classical OS problem for the plane Poisseuille flow. The main goals of the linear stability analysis are then to find conditions where $s_i = 0$ to determine the stability limit, and to find the wavelength giving the highest amplification rate. It is also useful to derive an equation for the kinetic energy of the pulsating motion, $K = 0.5\left\langle U_1^2 + V_1^2 \right\rangle$ ("$\langle\ \rangle$" denotes averaging), and then to look at different terms on its right-hand-side:

$$\frac{\partial K}{\partial t} + U_0\frac{\partial K}{\partial x} + V_0\frac{\partial K}{\partial y} = P_{K1} + P_{K2} + D + \varepsilon_v + \varepsilon_{Ha}. \tag{4.23}$$

The first term P_{K1} represents the shear production of kinetic energy, which is the product of the Reynolds stress and the mean flow strain rate. This shear production is identical to that in isothermal flows. The second term P_{K2} , whose main part is $\langle U'\theta' \rangle$, is another production term associated with temperature pulsations. The third term D is diffusion. The two last terms stand for dissipation losses: ε_v represents viscous dissipation in the bulk flow, while ε_{Ha} represents ohmic and viscous losses at the Hartmann walls, which are specific to Q2D MHD flows. In relation to the two production terms, in hydrodynamic buoyancy-driven flows, there have been identified two instability types (for references see Ref. [35]). In the first type, which was found primarily for lower-Prandtl-number fluids, the instability is initiated when the basic velocity profile is distorted sufficiently by buoyant forces to form an inflection point such that most of the kinetic energy for the instability comes from the shear production. This mode is termed as *thermal-shear instability*. The second type, which dominates in higher-Prandtl-number fluids, obtains its energy primarily from temperature fluctuations. This type is called *thermal-buoyant instability*. The reason that lower-Prandtl-number fluids don't exhibit thermal-buoyant instability is damping of temperature fluctuations due to high thermal conductivity of the fluid. In liquid metals, which are primarily coolants in fusion applications, $Pr \ll 1$. This suggests domination by thermal-shear instability in the blanket flows. All results computed in this paper are in fact limited to a particular value of the Prandtl number (0.01) typical to most liquid metals. For such a low Prandtl number both linear and non-linear computations have confirmed that the dominating instability type is thermal-shear instability.

A pseudospectral MATLAB code, which eliminates spurious eigenvalues (Ref. [68]), is used to solve the present OS problem. The code has been validated against available literature results, including linear stability of a plane Poiseuille flow (Ref. [69]) as well as stability of the

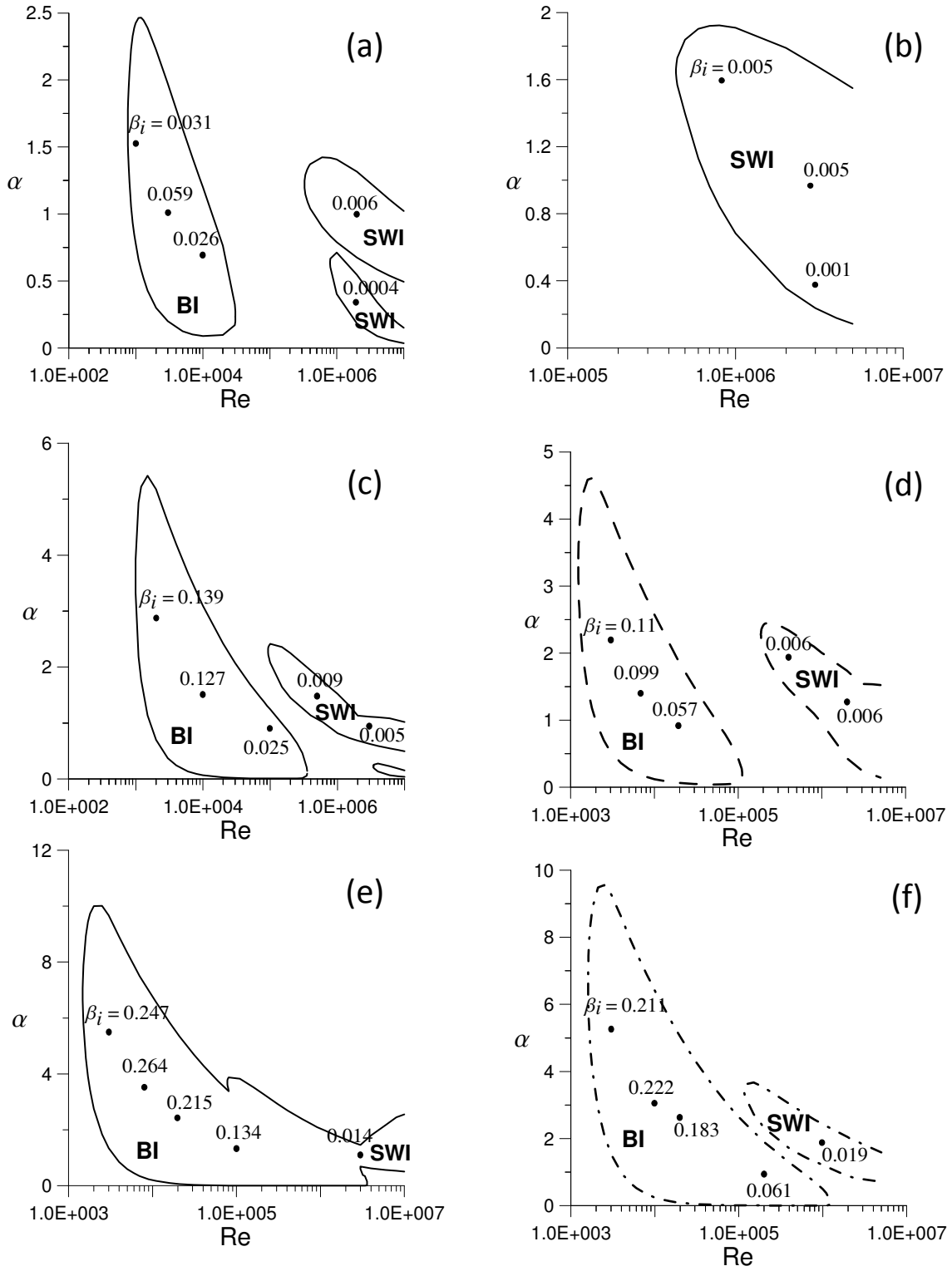

Fig. 4. 4: Neutral stability curves with indication of bulk (BI) and side-wall (SWI) instabilities at: (a) Ha=50, Gr=10^7; (b) Ha=100, Gr=10^7, (c) Ha=50, Gr=10^8; (d) Ha=100, Gr=10^8; (e) Ha=50, Gr=10^9; (f) Ha=100, Gr=10^9.

Hartmann (Ref. [70]) and Shercliff layers (Ref. [33]). A similar code was also used in our previous work Ref. [76]. The neutral stability curves for two Hartmann numbers (50 and 100) and three Grashof numbers (10^7, 10^8 and 10^9) are shown in Fig. 4.4. Depending on *Ha* and *Gr* there can be one, two or even three branches of the neutral curve. The flow is linearly unstable within the area bounded by the neutral curves and linearly stable outside. The figure also shows values of the amplification factor β_i inside each instability area. Similarly to Ref. [74], two instability modes have been observed that are associated either with the inflection point in the basic velocity profile in the flow bulk (*bulk instability, BI*) or with the boundary layer at each side wall (*side-wall instability, SWI*). The bulk instability is of the Kelvin-Helmholtz type (also known as inflectional instability), whereas the side-wall instability is related to propagation of Tollmien–Schlichting waves. The SWI branches in Fig. 4.4 are always situated to the right of the BI branch. This means that SWI starts at higher Reynolds numbers compared to BI when the basic velocity profile is only slightly deformed by buoyancy effects such that there are no inflection points, or if such points are nevertheless formed, the vorticity level at the inflection points is not high enough for inflectional instability to form. The two branches in Fig. 4.4a located at $Re \sim 10^6$ stand for the SWI mode. The lower branch of these two exhibits longer wavelengths (smaller α) but a smaller amplification rate compared to the other SWI branch. This branch fully disappears at higher Hartmann or Grashof numbers. The observed two SWI branches are consistent with similar observations in Ref. [33], where the case of purely Shercliff layers was studied using the same linear approach.

The differences between BI and SWI modes are well seen, for instance, in the vorticity distribution shown in Fig. 4. 5. In the case of the side-wall instability, there is just one row of counter-rotating vortices, all localized at the wall within the boundary layer. This instability

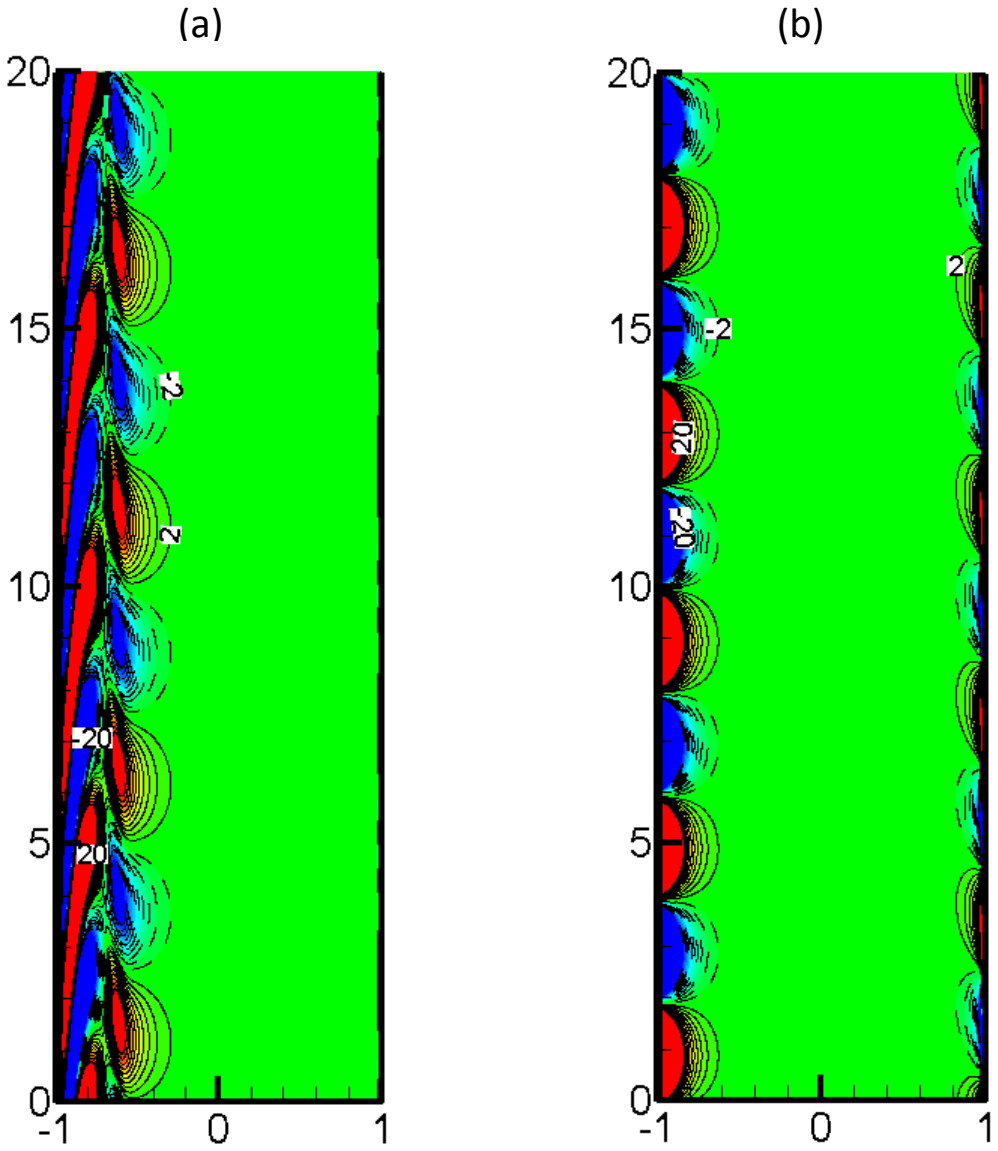

Fig. 4. 5: Vorticity distribution in the reference mixed-convection flow based on the linear analysis for the most amplified perturbation mode: (a) bulk instability at *Ha* =100, *Gr* = 1e+08, *Re* = 1e+04, and (b) side-wall instability at *Ha* = 100, *Gr* = 1e+08, *Re* = 1e+06.

typically occurs at higher Reynolds numbers and has about one order of magnitude lower amplification factor compared to the bulk instability. In the case of the bulk instability, there are two rows, one to the right and one to the left of the inflection point. Usually, the inflection point

is located on the bulk side of the velocity jet, close to the wall, such that the outer row of vortices is located in the near-wall region, where the velocity changes from zero at the wall to the maximum. Figure 4. 5 also shows significant asymmetry in the vorticity distribution. Typically, instability happens at both the hot and cold walls but it is always more intensive at the hot wall in both SWI and BI cases.

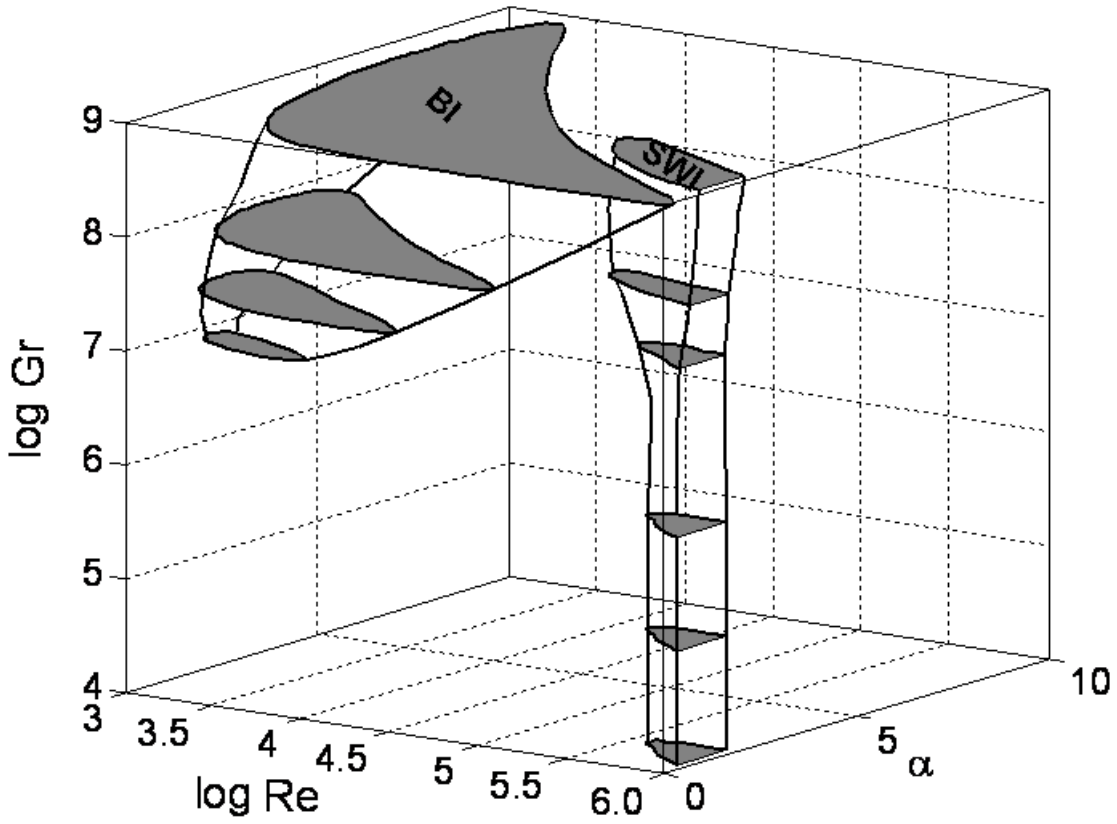

FIG. 4. 6: Neutral surfaces (instability balloon) at *Ha*=100 showing two types of instability regions (BI and SWI). The flow is linearly unstable inside each balloon and stable outside.

As seen in Fig. 4. 4, the BI and SWI can happen under the same conditions, for example at the same Reynolds number. In such cases, the SWI mode always exhibits shorter wavelengths. This suggests that in real flows, these two instability modes can co-exist since original disturbances can be of any frequency. In some cases, however, the two neutral curve branches are fully separated suggesting only one instability mode as also demonstrated in Fig. 4. 6, where the neutral curves are plotted in the 3D form.

The differences between BI and SWI are further illustrated in Fig. 4.7 in the form of dispersion curves. This figure clearly demonstrates the possibility of either two instability modes happening at the same Reynolds number but at different wavelengths or just one mode.

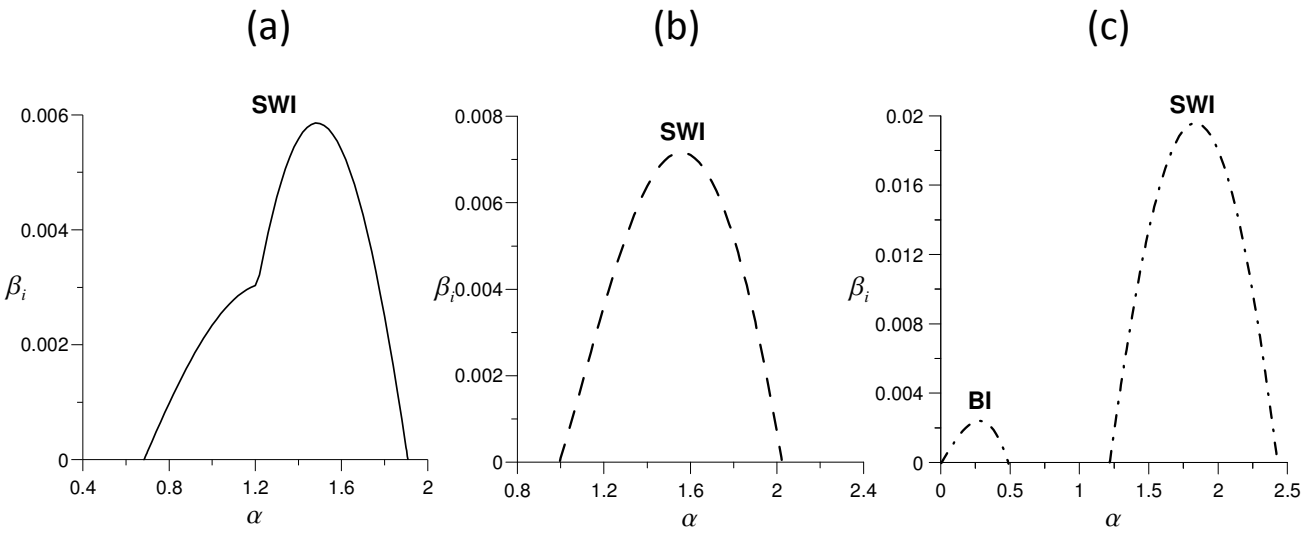

Fig. 4.7: Typical dispersion curves at Ha = 100, Re = 1e+06: (a) $Gr = 10^7$, (b) $Gr = 10^8$, and (c) $Gr = 10^9$.

The rate of growth of infinitesimal disturbances with time in the linear phase is best characterized with the parameter β_i. The effect of Gr, Re and Ha numbers on this parameter is illustrated in Fig. 4.8. As the Hartmann number is increased, the amplification rate always drops.

The Grashof number has the opposite effect: the higher *Gr*, the higher the amplification rate. The effect of the Reynolds number is more complex. For example for *Ha*=100 and *Gr*=10^8, β_i first increases with *Re*, then decreases to zero and after that starts increasing again. Such a complex behavior is related to changes in the instability type from BI to SWI. Finally, Fig. 4.9 shows the critical Hartmann number Ha_{cr} as a function of Grashof number at several *Re* numbers. For all *Ha* numbers greater than Ha_{cr}, the flow is linearly stable, whereas it is unstable if $Ha < Ha_{cr}$.

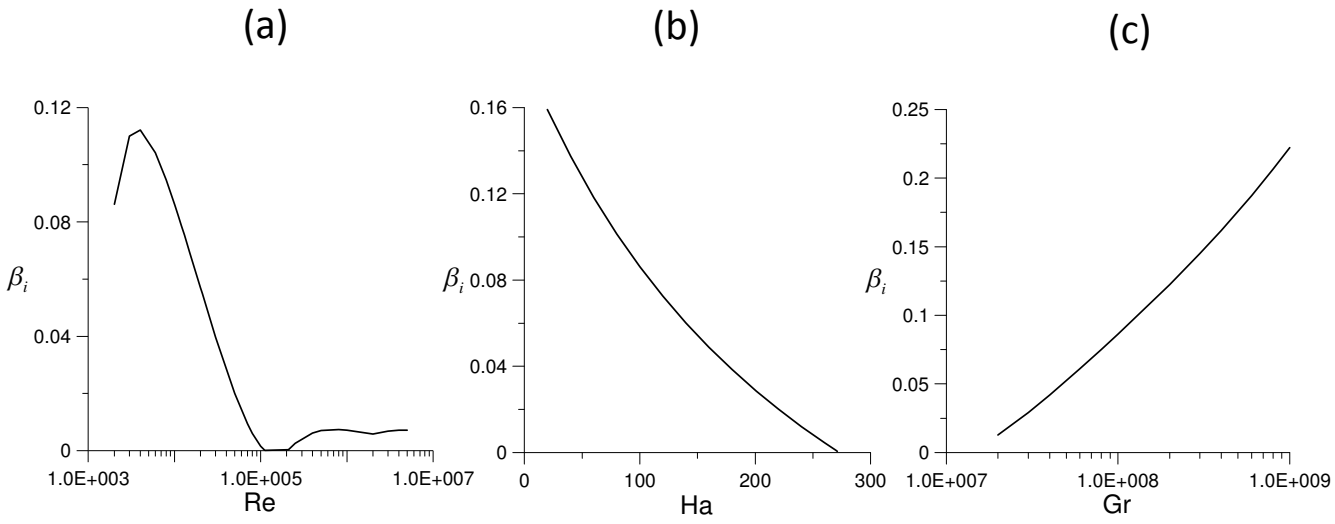

Fig. 4.8: Effect of the flow parameters on the amplification factor: (a) *Ha* =100, *Gr* = 10^8; (b) *Re* = 10,000, *Gr* = 10^8; and (c) *Ha* =100, *Re* = 10,000.

The obtained data for Ha_{cr} can be approximated with the following formula:

$$Ha_{cr} = P_1(\log Gr)^2 + P_2 \log Gr + P_3, \tag{4.24}$$

where

$$P_1 = -5.98\times10^{-8}\,Re^2 + 2.284\times10^{-3}\,Re + 2.308,$$
$$P_2 = 1.8277\times10^{-6}\,Re^2 - 7.3037\times10^{-2}\,Re - 22.787,$$
$$P_3 = -1.37\times10^{-5}\,Re^2 + 0.57516Re - 95.8.$$

Notice that applicability of this formula is guaranteed under specific conditions assumed in the present study, namely for 5000 < Re < 20,000 and Gr from 10^6 to 10^9.

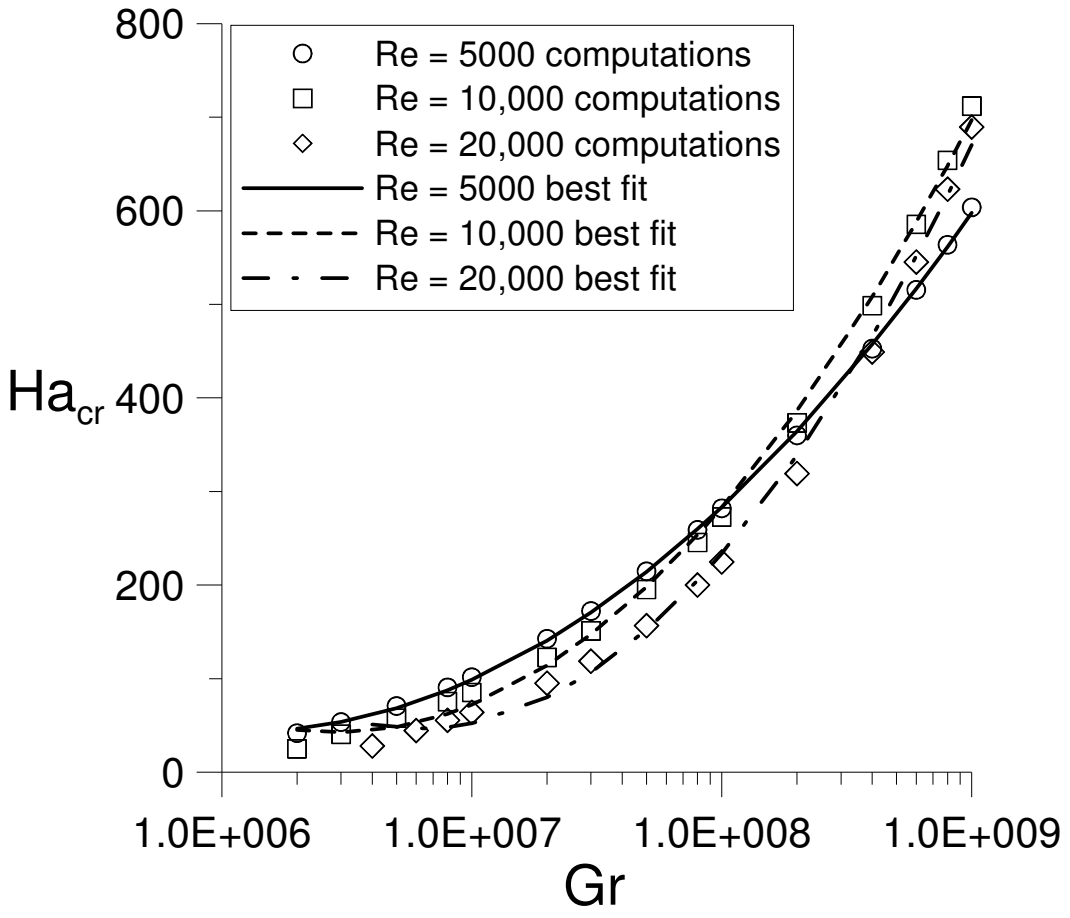

Fig. 4.9: Variation of the critical Hartmann number versus Grashof number at several *Re* numbers. Symbols stand for computations and lines for the best fit.

4.5 Nonlinear computations

Once the amplitude of perturbations becomes big enough, the nonlinear flow behavior often turns out to be very different from that predicted by the linear theory. To address nonlinear features we perform DNS-like computations by solving time-dependent Eqs. (4.16-4.18) over a long period of time and applying periodic boundary conditions at the flow inlet/outlet. A computer code, briefly described in sec. 3.3, extends a standard time-marching $\psi - \omega$ approach to the reference case to take into account MHD and buoyancy effects. The governing equations are approximated with finite-volume formulas on a mesh, which is uniform in the axial direction and non-uniform in the cross-axial direction. The mesh clusters points near the wall within the side-wall boundary layers. At least ten points are placed within each boundary layer. The discretization is of a second-order accuracy in time and space. Advancing in time is performed using an Adams-Bashforth scheme. Central-difference formulas are used for the discretization of the diffusive terms in the ω- , ψ- and θ-equations. For the convective terms, a conservative scheme proposed by Arakawa (Ref. [72]) is used. This scheme, which conserves the basic quadratic quantities, such as the mean kinetic energy and the mean enstrophy, allows for accurate computations of the nonlinear terms in 2D turbulent flows. Periodic boundary conditions are applied at the flow inlet and outlet, while no-slip and zero-heat-flux boundary conditions are used at the walls $y = \pm 1$. Using periodic boundary conditions when solving the elliptic equation for the streamfunction allows for implementation of a direct algorithm based on the Fast Fourier Transform (FFT), which is much faster and more accurate compared to most of the relaxation techniques.

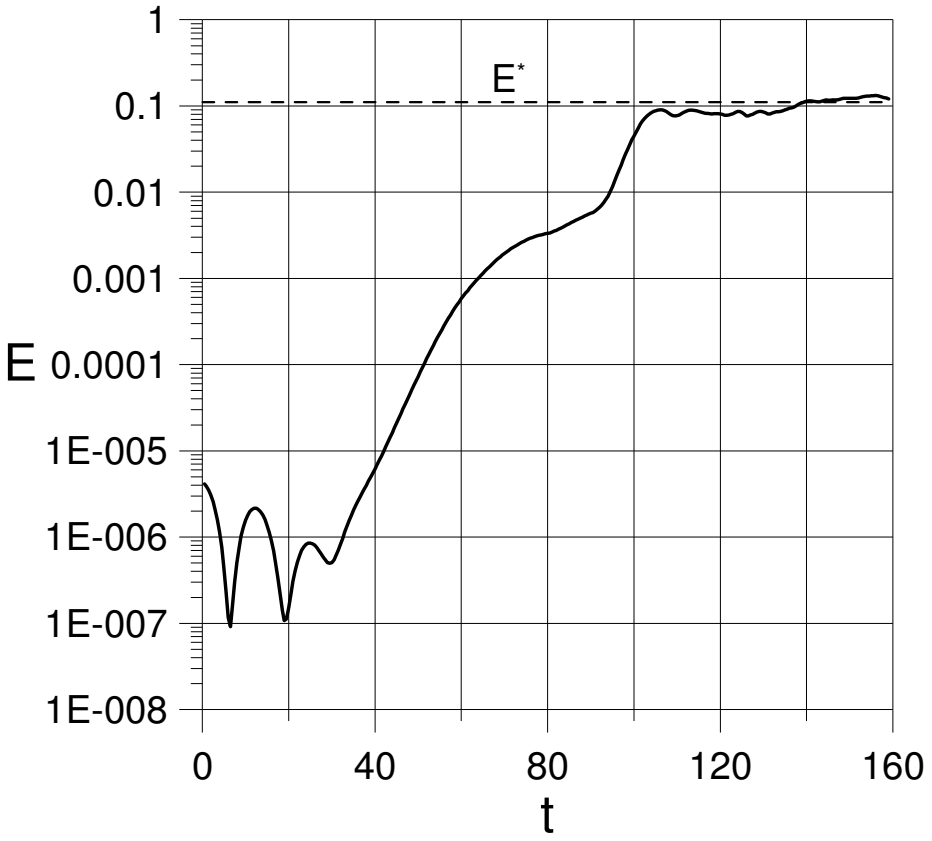

Fig. 4.10: Typical variation of the kinetic energy of the fluctuating flow versus time at $Ha = 50$, $Gr = 10^8$ and $Re = 5000$.

The nonlinear computations have been performed for $40 < Ha < 200$, $2000 < \mathrm{Re} < 10{,}000$ and $10^6 < Gr < 5\times10^8$ to address the effect of these parameters on the flow. For these parameters $D < 0$, suggesting basic velocity profiles with a distinctive high-velocity jet near the hot wall. These relatively low values of *Re*, *Ha* and especially *Gr* compared to those in fusion applications are explained by computational limitations, on the one hand and, on the other hand, by limitations of the Q2D model itself as discussed in Section 4.2. However, it seems to be appropriate to extrapolate observed tendencies in the flow to higher values relevant to blanket conditions, providing the major limitations of the Q2D theory are still met. In the computations,

the flow domain is as long as 60 length units, which is sufficiently large to accommodate many wavelengths as computed with the linear stability analysis for the most amplified modes. As a result of sensitivity tests, a mesh of 512 (along the flow) by 201 points (across the flow) and the integration time step $\Delta t = 0.0005$ were chosen. At the initial moment the flow is disturbed by small perturbations, random in space, which are imposed on the basic flow streamfunction, without disturbing the vorticity field. Typical changes of the mean kinetic energy of the whole flow defined as

$$E(t) = \frac{1}{2l}\int_0^l dx \int_{-1}^{1} 0.5\left[(U - U_m)^2 + V_1^2\right] dy \tag{4.25}$$

versus the computational time are shown in Fig. 4.10. During a short initial phase (t<30) the kinetic energy is small and fluctuating. The fluctuations in E seem to be related to the effect of the initial condition, where perturbation modes are randomly distributed. In the next phase (30<t<60), the flow demonstrates nearly linear behavior that corresponds to the exponential growth in time of the most amplified mode. This linear behavior is followed by a transitional phase (60<t<100), where nonlinear effects become more and more dominant, manifested for example by various vortex-vortex and vortex-wall interactions. Finally, as a result of intensive vortex formation and simultaneous energy dissipation, the flow reaches a nonlinear saturation phase (t>100), where the averaged energy E remains at about the same level E^*, whereas the flow demonstrates pulsating near-periodic behavior in both time and space. This regime can be considered as a new dynamic equilibrium state in which the averaged flow no longer varies. Examples of flows in the nonlinear saturation phase are given in Fig. 4.11, where the vorticity snapshots are shown at several Hartmann numbers

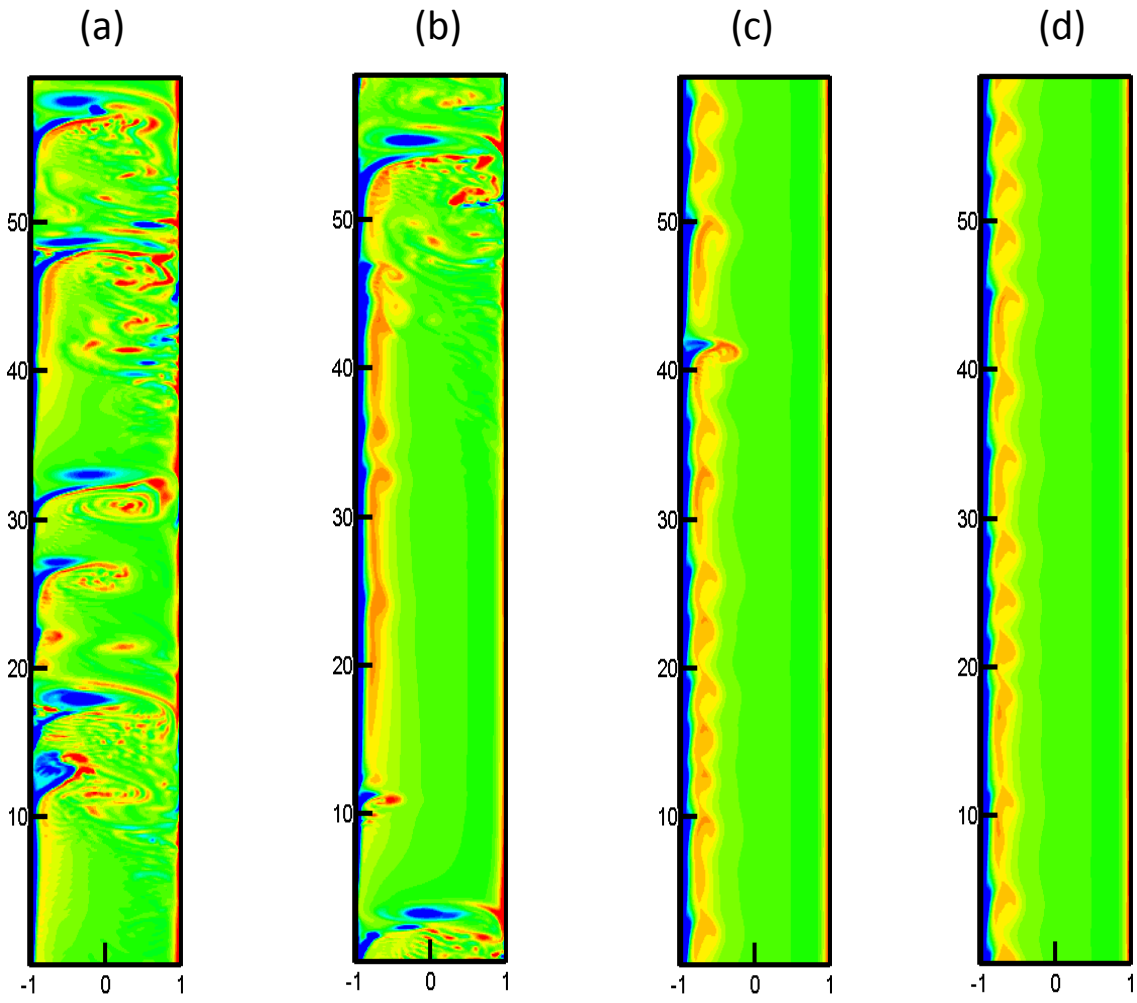

Fig. 4.11: Vorticity snapshots in the non-linear saturation phase showing the effect of *Ha* number at *Re* = 5000 and *Gr* = 1e+08: (a) *Ha* = 50, (b) *Ha* = 60, (c) *Ha* = 100, and (d) *Ha* = 120.

These and other similar snapshots in Figs. 4.12 and 4.13 clearly demonstrate two different turbulence regimes, which we call "*strong turbulence*" (ST, *e.g.*, Fig. 4.11a and b) and "*weak turbulence*" (WT, *e.g.*, Fig. 4.11c and d). In the WT regime, the vortices are mostly formed from the original shear layer in the bulk flow near the hot wall. They remain localized in the same near-wall area where the basic velocity profile has an inflection point. Some vortex-wall

interactions are clearly seen resulting in destabilization of the side-wall boundary layer, but neither separation of the boundary layer from the wall nor formation of isolated vortices can be seen. In the ST regime, the two characteristic features are intensive vortex-vortex and vortex-wall interactions.

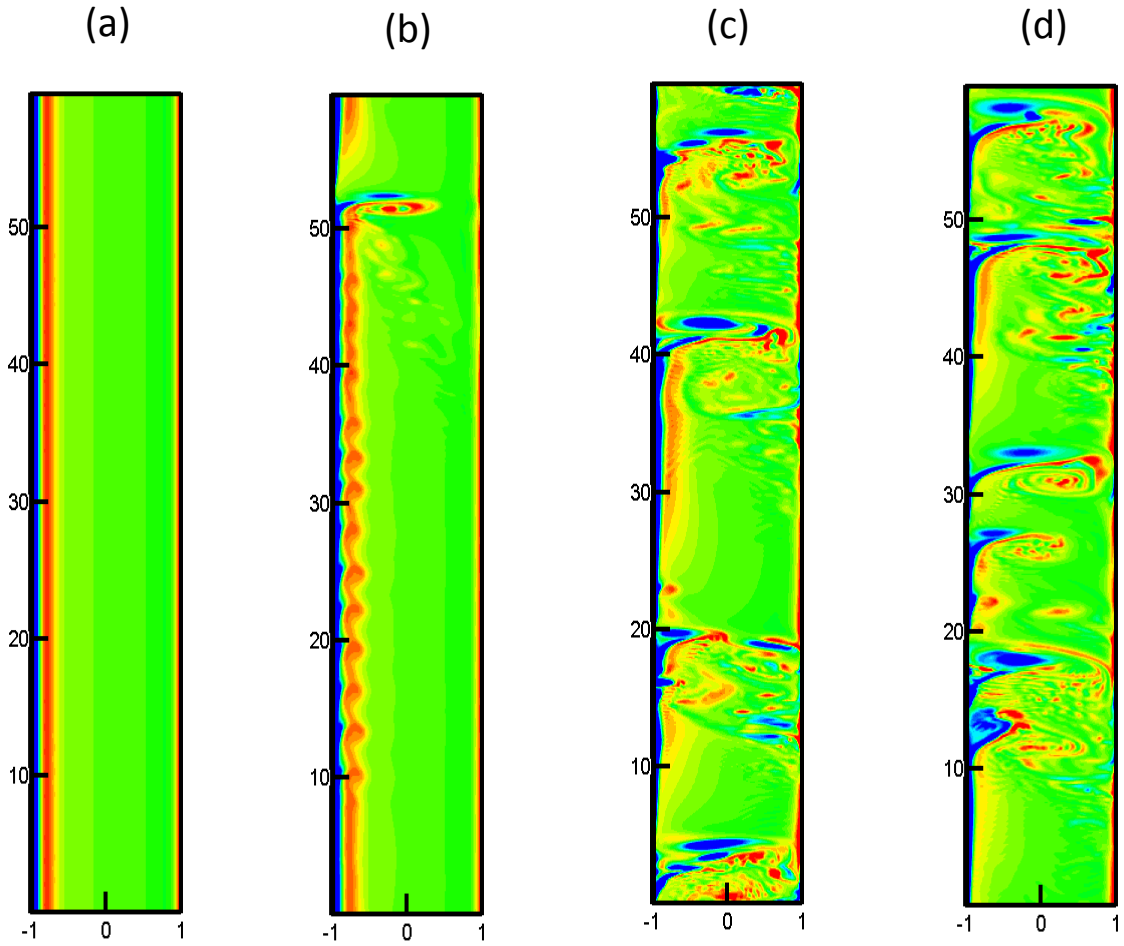

Fig. 4.12: Vorticity snapshots in the non-linear saturation phase showing the effect of *Re* number at *Ha* = 50 and *Gr* = 1e+08: (a) *Re* = 2000, (b) *Re* = 3000, (c) *Re* = 4000, and (d) *Re* = 5000.

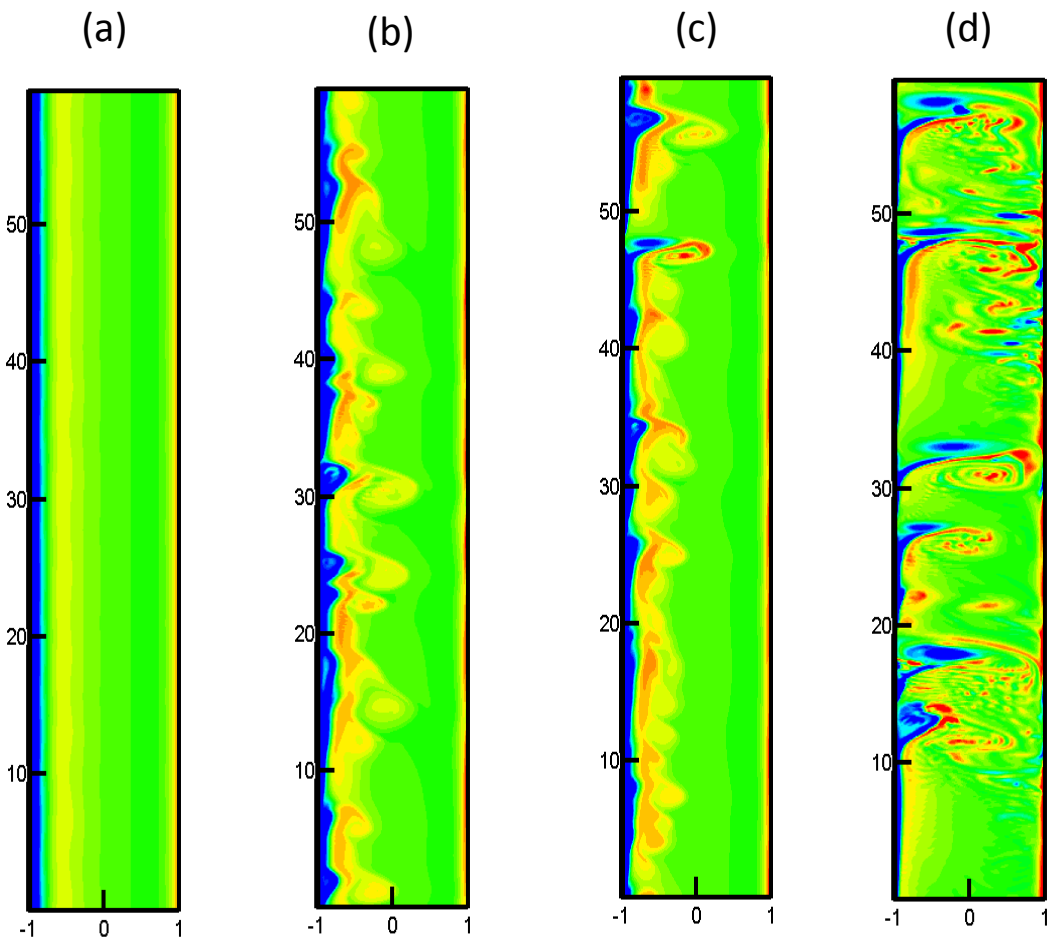

Fig. 4.13: Vorticity snapshots in the non-linear saturation phase showing the effect of *Gr* number at *Ha* = 50 and *Re* = 5000: (a) $Gr = 10^7$, (b) $Gr = 5\text{x}10^7$, (c) $Gr = 7\text{x}10^7$, and (d) $Gr = 10^8$.

The vortex-wall interactions occur between the primary bulk vortices and the near-wall liquid. These interactions cause destabilization of the boundary layer and eventually its detachment from the wall at several locations along the flow path. This process involves a few characteristic stages. It is initiated first by a local concentration of the vorticity field within the side-wall boundary layer as a single bulk vortex or a group of vortices move along the wall. This stimulates rapidly-rising thin spires (streaks) of fluid that ultimately interact strongly with the external flow. These structures typically contain concentrated vorticity and often roll up into

new, secondary, vortex structures. These newly-developed vortices can travel far from their original location reaching sometimes the opposite wall and destabilizing its boundary layer. The vortex-vortex interactions occur between various vortices, including primarily bulk vortices and secondary vortices, which are formed due to the destabilization of the side-wall boundary layer by the bulk vortices. These interactions are typical to Q2D turbulence as required by the inverse energy cascade and include pairing vortices of opposite signs and merging two or more vortices of the same sign into a bigger compound vortex structure, comparable in size with the duct width, as also seen in Figs. 4.11-4.13.

Changing the other two parameters, *Re* and *Gr* (Fig. 4.12 and 4.13), hasn't revealed any new peculiarities in the vorticity field in addition to those observed in Fig. 4.11. Depending on the 3 parameters either WT or ST regimes can be seen. However, increasing *Ha* always leads to the reduction of the kinetic energy, transition from strong to weak turbulence and finally to flow laminarization. Unlike the Hartmann number effect, increasing *Re* and *Gr* leads to more turbulent flows. Based on observations of the vorticity fields shown in Figs. 4.11-4.13, the turbulence can be considered as strong if $E > E_{cr} = 2\times10^{-2}$. This criterion is further used in order to characterize the effect of these parameters on the turbulent flow regime. Two flow maps are shown in Figs. 4.14 and 4.15, where regions corresponding to ST and WT regimes are shown in the *Ha*-*Re* plane for two Grashof numbers. Also, at the top of these two figures the critical Hartmann number Ha_{cr} calculated with Eq. (4.23) is shown. These figures clearly demonstrate that the linear theory significantly overpredicts the stability threshold. The tendency of the OR theory to overpredict critical parameters that characterize flow stability and poor agreement with experimental and numerical data are well known (see, *e.g.* Ref. [77]), so that the present

observation is fully consistent with previous conclusions. For illustrative purposes, the two flow maps are combined into one 3D figure, in Fig. 4.16.

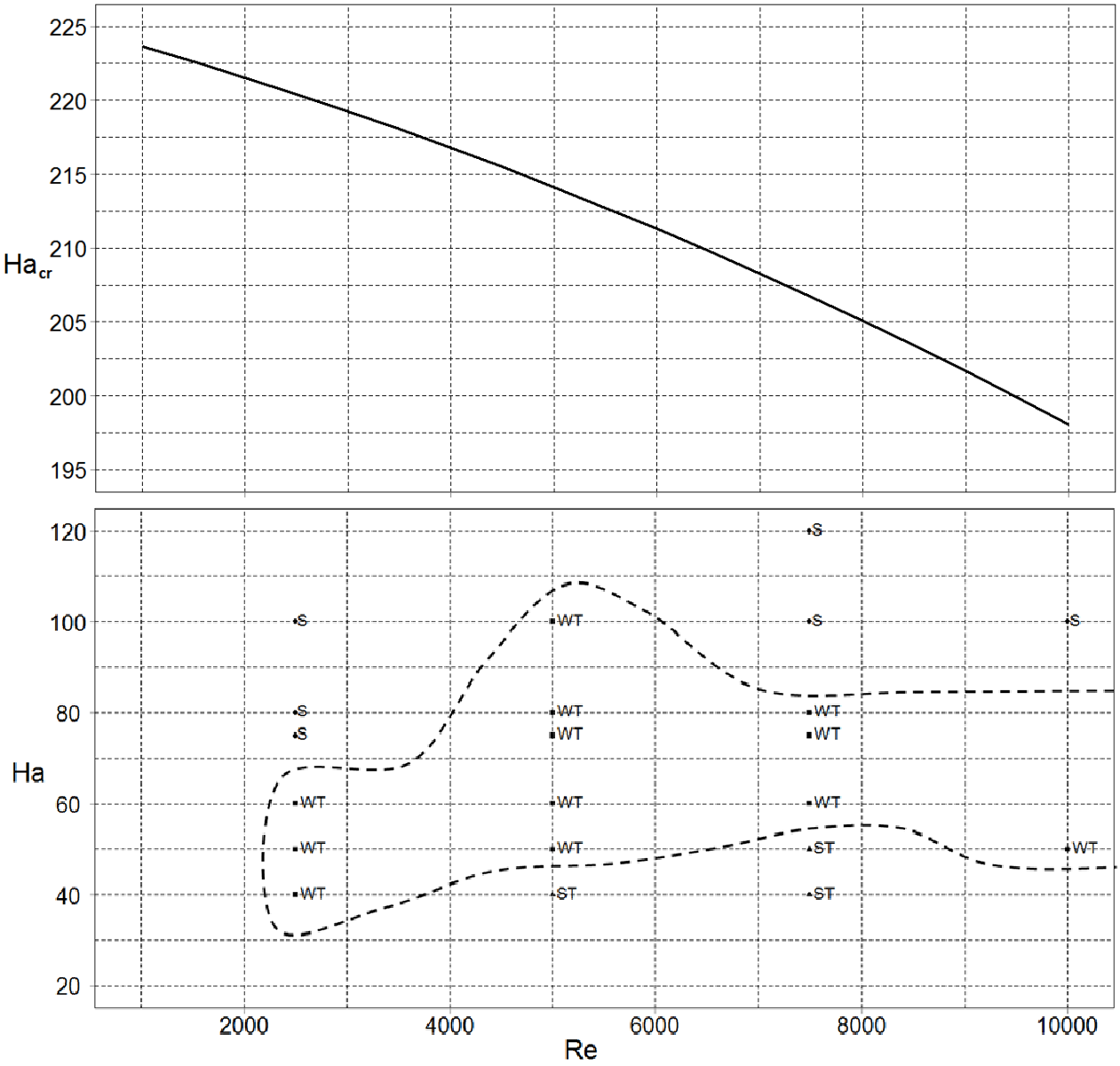

Fig. 4.14: Bottom: flow map showing laminar and two turbulent regimes in the *Ha* – *Re* plane for *Gr* = $5x10^7$. S –stable laminar flow, WT- weak turbulence, and ST – strong turbulence. Top: predictions of the critical Hartmann number with the linear theory.

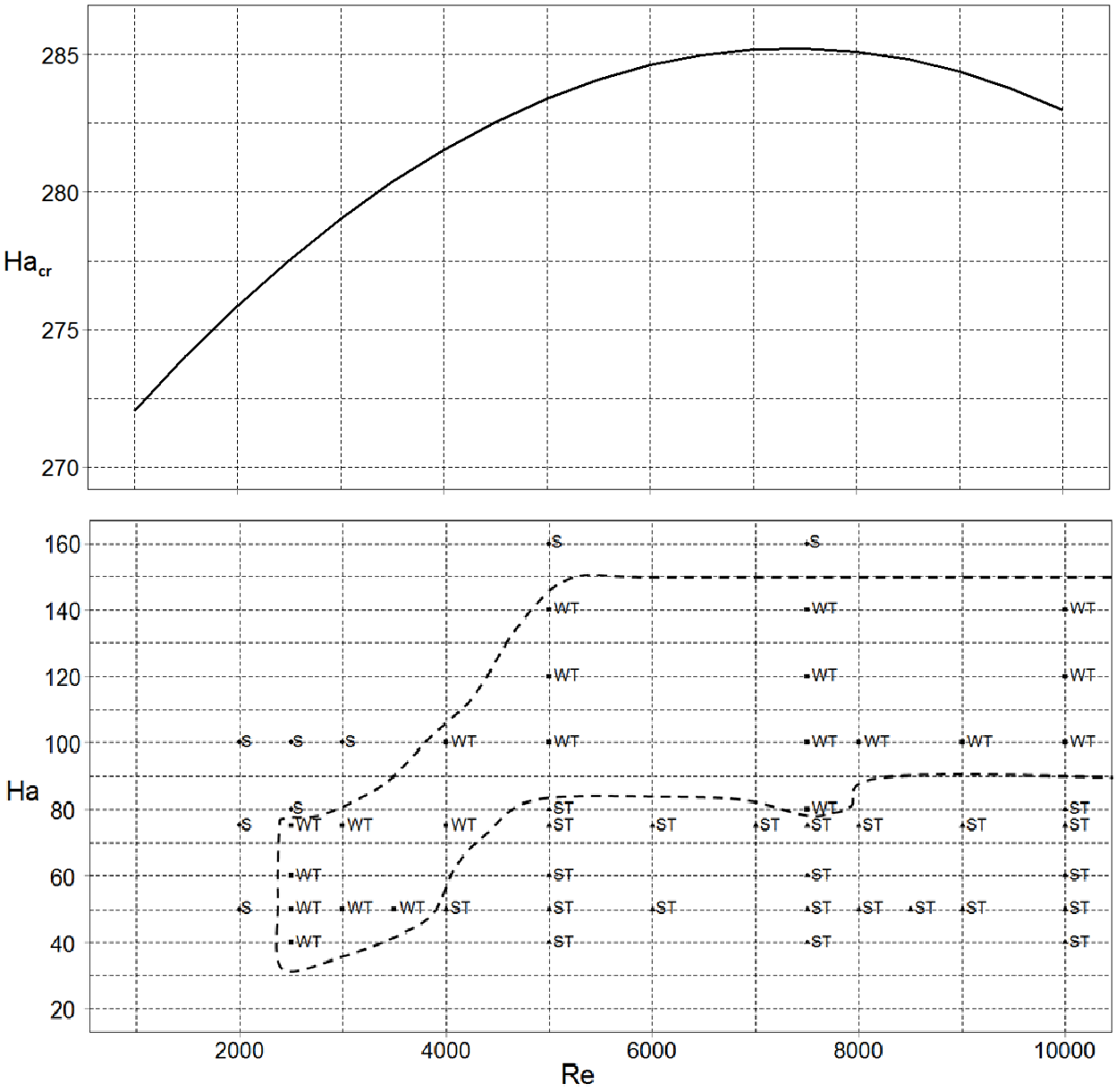

Fig. 4.15: Bottom: flow map showing laminar and two turbulence regimes in the *Ha* – *Re* plane for *Gr* = 10^8. Top: predictions of the critical Hartmann number with the linear theory. See also notations in Fig. 4.14 captions.

Figures 4.17, 4.18, and 4.19 illustrate changes in the kinetic energy E^* in the nonlinear saturation phase as a function of *Re*, *Gr* and *Ha*. As the Hartmann number is increased, the kinetic energy drops monotonically to zero (Fig. 4.17). The increase in *Re* leads to the kinetic energy growing until the saturation level is achieved, which depends on the other two parameters (Fig. 4.18). The kinetic energy also grows as the *Gr* number is increased; however, any saturation in E^* with *Gr* for Grashof numbers up to $3\text{x}10^8$ has not been observed (Fig. 4.19).

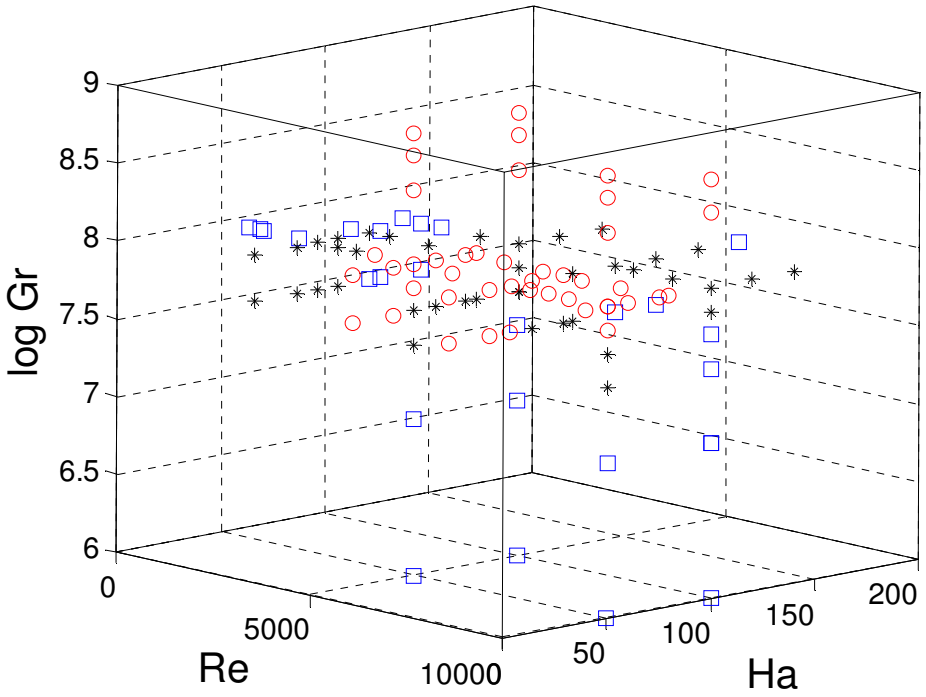

FIG. 4.16: 3D flow map in the *Ha–Gr–Re* space: □ - stable laminar flow, ✱ - weak turbulence, and ○ – strong turbulence.

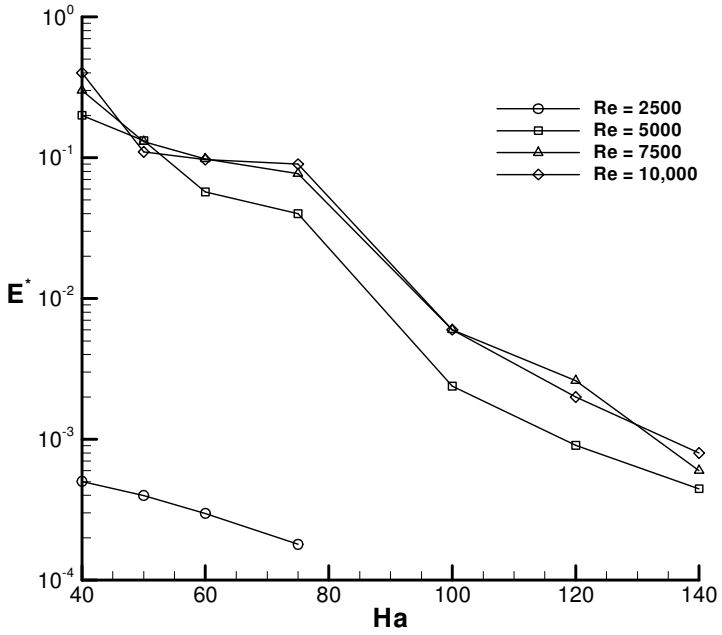

Fig. 4.17: Variation of the kinetic energy with *Ha* for different *Re* at $Gr = 10^8$.

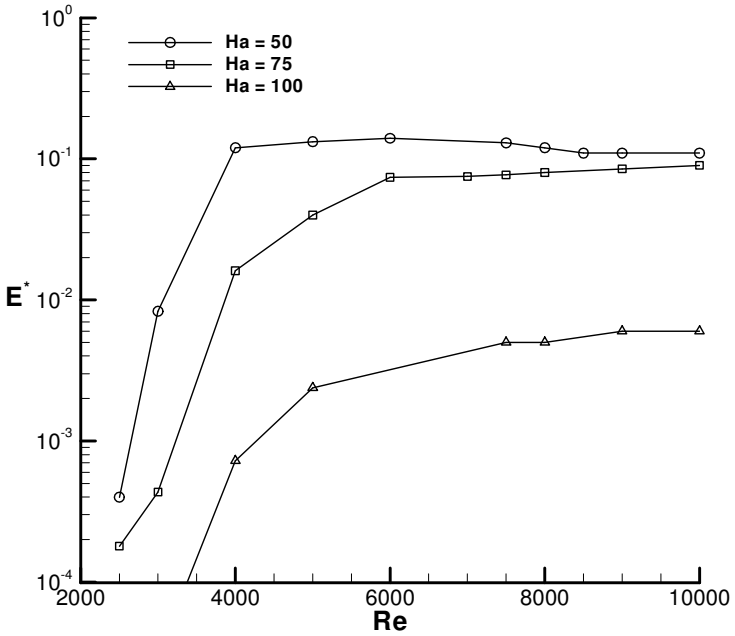

Fig. 4.18: Variation of the kinetic energy with *Re* for different *Ha* at $Gr = 10^8$.

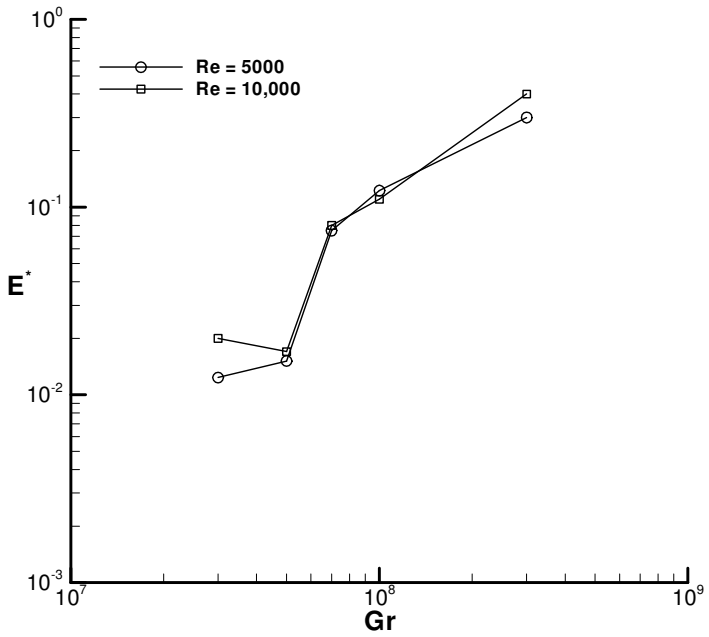

Fig. 4.19: Variation of the kinetic energy with *Gr* for different *Re* at *Ha* = 50.

Finally, Fig. 4.20 illustrates differences between the basic and turbulent flows where comparisons are shown for the velocity and temperature distributions. In the strong turbulence regime, such differences are much more pronounced compared to weak turbulence. In the weak turbulence regime, the changes in the velocity profile are mostly localized at the velocity peak associated with the near-wall jet, while in the strong turbulence regime the whole velocity profile is changed, not only near the hot wall but also in the bulk flow and at the cold wall. In both cases, turbulence results in a decrease of the maximum velocity near the hot wall.

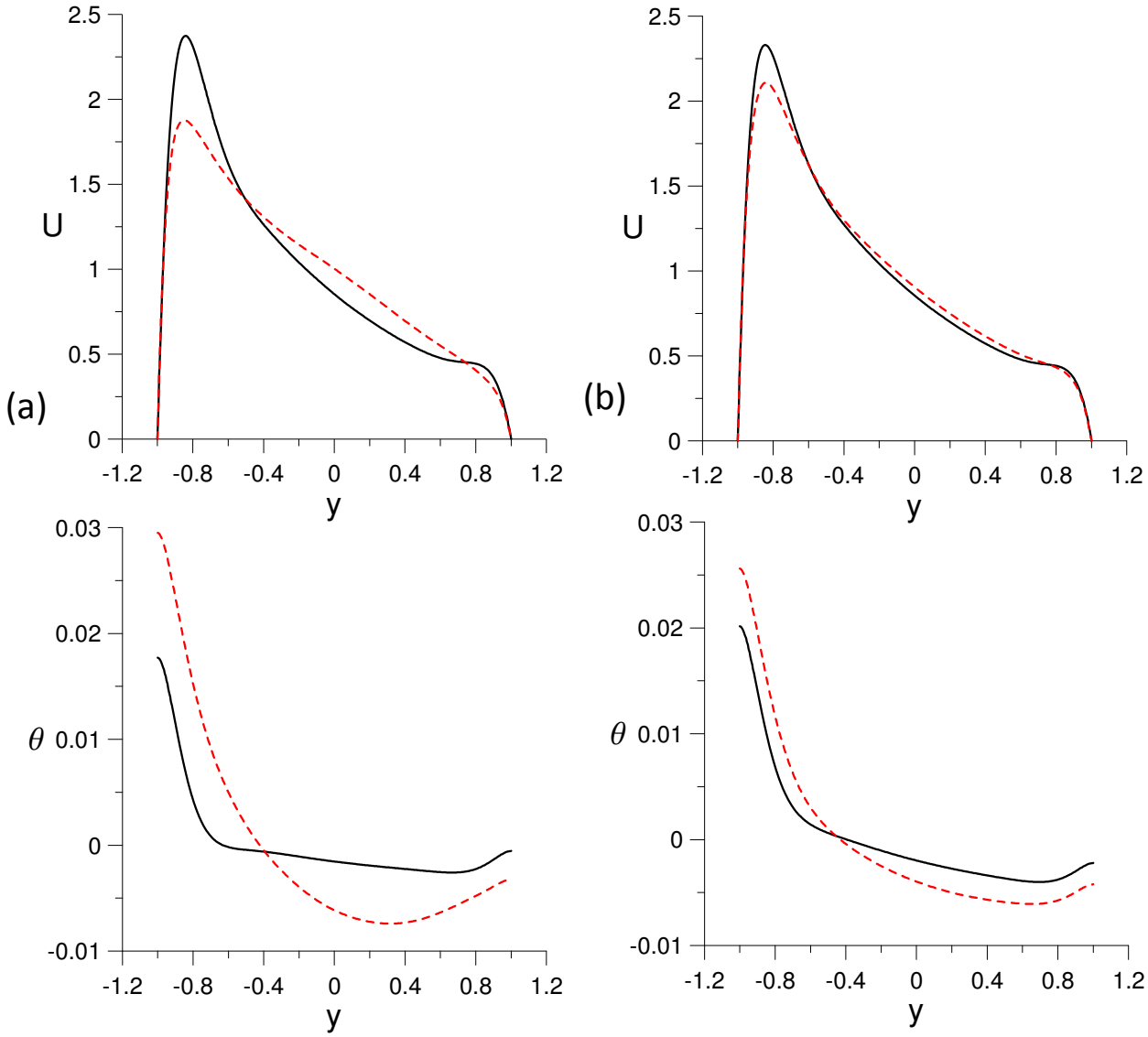

Fig. 4.20: Comparison of temperature and velocity profiles between basic (solid line) and turbulent (dotted line) flows: (a) strong turbulence at Ha=50, $Gr = 10^8$, Re = 5000; and (b) weak turbulence at Ha=100, $Gr = 10^8$, Re = 5000.

CHAPTER 5

Mixed convection flow in prototype blanket

5.1 Numerical modeling of flow in DCLL geometry

As discussed in chapter 1, huge values of the parameters (*Ha*, *Re* and *Gr*) and complex geometry of the blanket module are the main hurdles to begin a numerical study of the liquid metal flow in the fusion reactor blanket. In our work, we followed a stepwise approach to understand the liquid metal flow in the conditions similar to blanket. First, we simplified the geometry by considering only the poloidal section of the duct and carried out analytical, linear and non-linear studies of the flow in this geometry. Chapters 3 and 4 describe the basic features of the fully developed flow, different mechanisms of instability and various levels of turbulent interaction of vortices for the flow in this simple geometry. However, in the real blanket conditions the flow enters in radial direction, turns into poloidal direction and leaves in the radial direction. The next step is to study the flow of liquid metal in such geometry. A full 3D modeling of the flow is carried out using the MHD solver HIMAG. The following sections discuss about the solver, flow geometry and obtained results in more detail.

5.2 HIMAG-overview

HIMAG has been developed as an extension to the HyperComp electromagnetics code environment [78], and compressible MHD code development activities [79]. HMAG has

inherited a parallel, unstructured code environment from the electromagnetics software, and has essentially replaced the solver and code integration strategies. The major subroutines in HIMAG are the solver sub-routines, each of which has numerical models implemented within to solve for a particular physics. The solver sub-routines are written in FORTRAN. The main solver sub-routines include sub-routines to solve the Navier-Stokes equations, the energy equation, the MHD body force solver, the free surface evolution solver, the Poisson equation solver, the gradient calculator, boundary condition assignment sub-routine etc. The other sub-routines routines in HIMAG are the functional sub-routines which perform the task of dynamic memory allocation, parallel partitioning of the computational mesh, loading data inputs etc. Most of the functional sub-routines are written in the computer language C. HIMAG has inherited the parallel message passing environment (based on MPI protocol) from HyPerComp's suite of electromagnetics codes. Within each physical phase of the solution process, sub-iterations are performed and data is exchanged periodically across computer node boundaries. Apart from these sub-routines, there are in house utilities developed at HyPerComp which perform the task of mesh generation (or mesh format conversion from an external mesher), mesh partition, input and boundary conditions data partition and finally solution assembly and post processing. The code can be compiled on LINUX or Solaris based machines.

Now, we give a brief description of the mathematical equation sets that describe the incompressible MHD flow phenomenon and have been implemented in HIMAG. Each individual physical phenomenon is modeled separately and interacts through a weak coupling. The flow of fluid phenomenon is governed by the 3D Incompressible Navier-Stokes equations, which include the equation of continuity and the equations for the three components of fluid momentum. Additionally, the body force and surface forces action are included in the

momentum equation. The main body forces that influence the fluid flow are the $\mathbf{j}\times\mathbf{B}$ MHD drag and the force due to gravity. The system of Navier Stokes equation with the MHD body force (whose magnitude depends on the flow field) is solved using the projection method in a cell center based finite volume formulation, where the velocity components are advanced in time and then corrected by deriving the pressure gradient field, using a scheme that forces the conservation of mass. As discussed in chapter 2, there are several formulations that can be used to calculate the MHD effects in the modeling of incompressible MHD flow where the magnetic Reynolds number much smaller that unity. In HIMAG, the principal formulation for calculation of the MHD forces is the electric potential formulation. A formulation based on the magnetic induction equation is also in place but is seldom used. Modeling of incompressible MHD flows at high Hartmann number, using the electric potential formulation, requires some specialized techniques in which the electric current is numerically computed from the electric potential. In HIMAG all the solution quantities are based on an unstructured collocated mesh, i.e. at the cell center of the mesh elements. The electric current density is calculated on the cell faces using a consistent and conservative approach. A conservative interpolation technique has been developed by researchers at UCLA (see [55, 56]) to obtain the current density at the cell center from the current density fluxes on the cell faces. A conservative current density at the cell center leads to an accurate computation of the Lorentz force to be used in the momentum equation. The implementation of the Poisson solver is critical in HIMAG, as the solution to the pressure Poisson and the electric potential Poisson equations are the two processes that require the most computer time during a computational step. The solution to these elliptic equations is obtained by iterative schemes of either point wise relaxation or the conjugate gradient method. The numerical models implemented in HIMAG to solve 3D incompressible Navier Stokes quations,

Poisson equation for pressure and electric potential are briefly described in [50] and are omitted here.

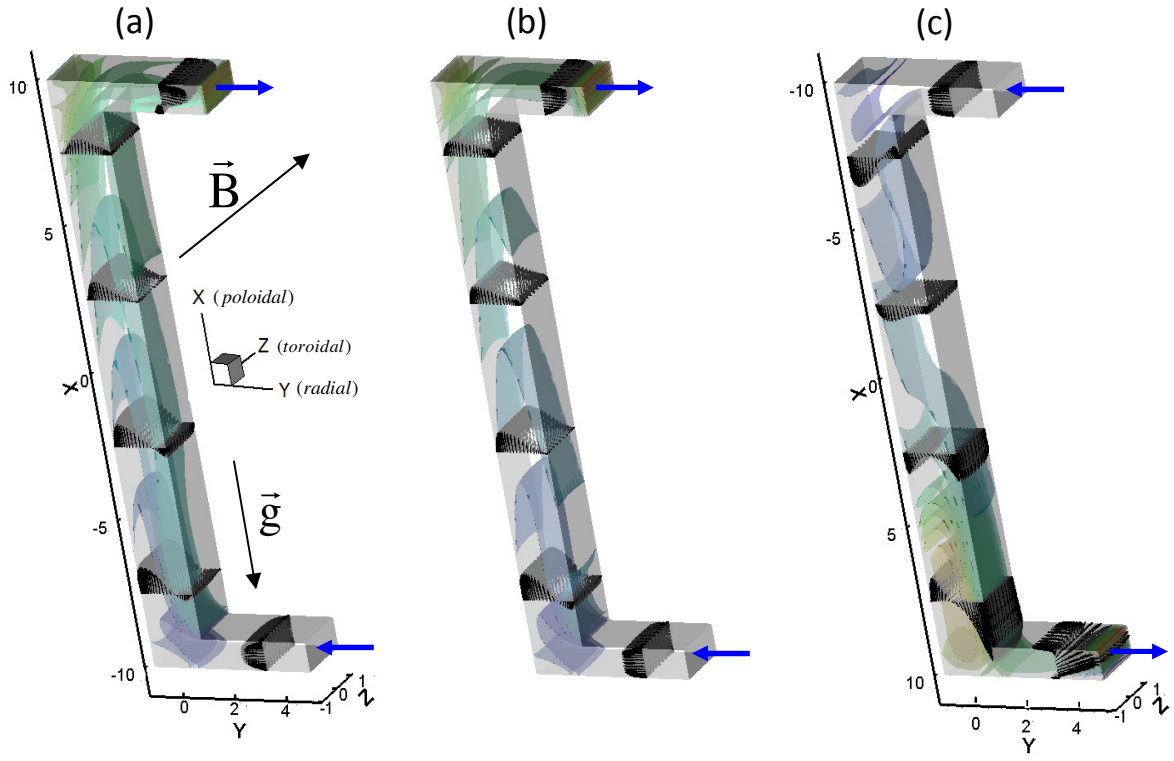

Fig. 5.1: 3D temperature contours and velocity vectors: (a) upward flow at *Ha*=100, *Re*=5000, $Gr=10^7$, (b) upward flow at *Ha*=400, *Re*=5000, $Gr=10^7$, (c) downward flow at *Ha*=400, *Re*=5000, $Gr=10^8$.

5.3 MHD flow in DCLL geometry

The duct consists of a long poloidal and two radial sections at the top and bottom as shown in Fig. 5.1. The radial sections are added for the similarity with the real blanket geometry. The flow starts either at the bottom (upward, buoyancy-assisted flow) or at the top (downward, buoyancy-

opposed flow). The full governing 3D Navier-Stokes/Maxwell/Energy equations are solved numerically with a 3D parallel MHD code HIMAG using the mathematical formulation based on the electric potential. The Hartmann and the side layers at the duct walls perpendicular and parallel to the applied magnetic are fully resolved. The calculations are performed for parameter range of: $100 < Ha < 1000$, $3000 < Re < 10000$, and $10^7 < Gr < 10^8$.

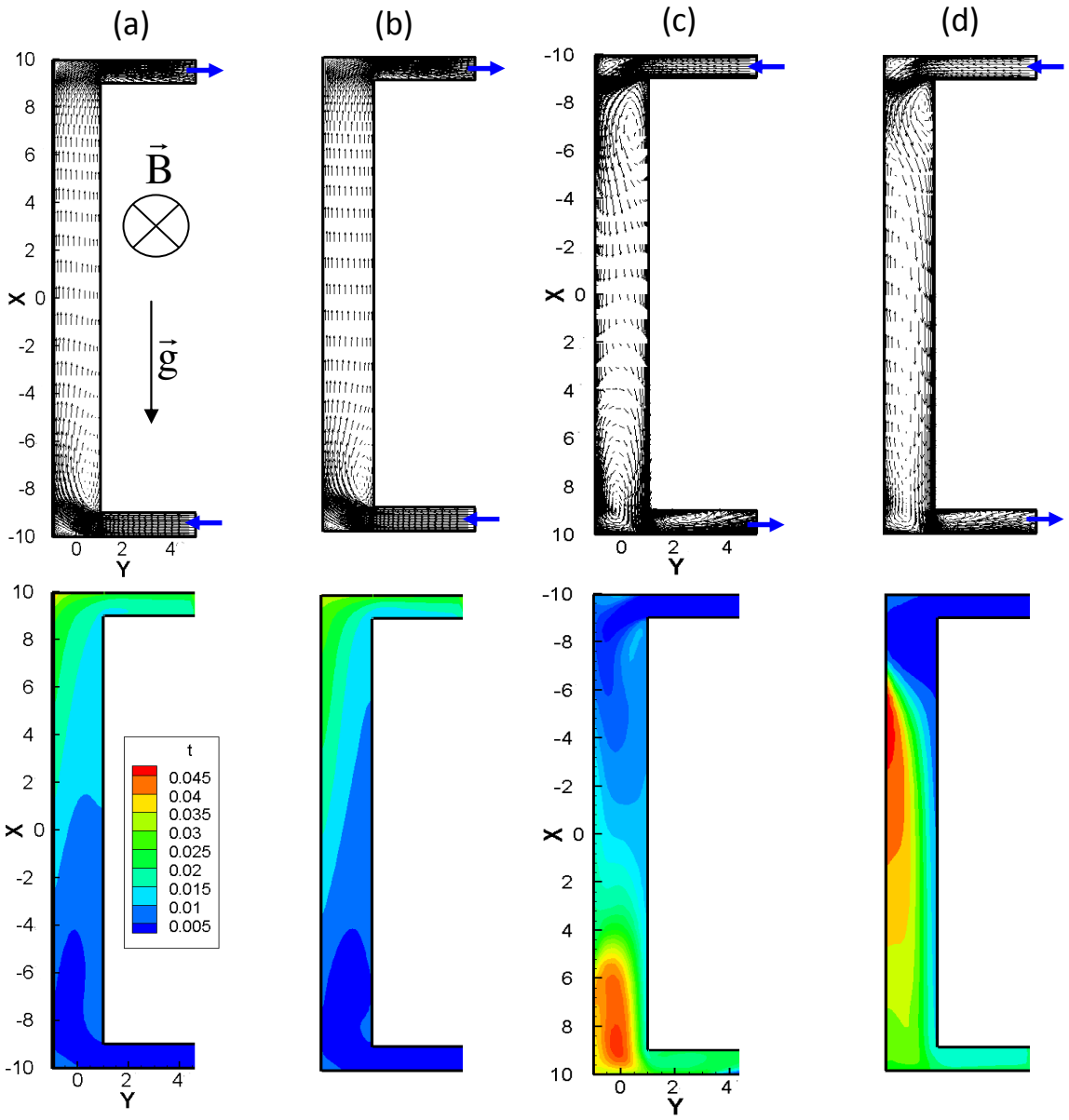

Fig. 5.2: Velocity vectors (upper) and temperature contours (lower) at the duct midplane z=0: (a) upward flow at Ha=700, Re=5000, Gr=10^7, (b) upward flow at Ha=1000, Re=5000, Gr=10^7, (c) downward flow at Ha=400, Re=5000, Gr=10^8, (d) downward flow at Ha=1000, Re=5000, Gr=10^8.

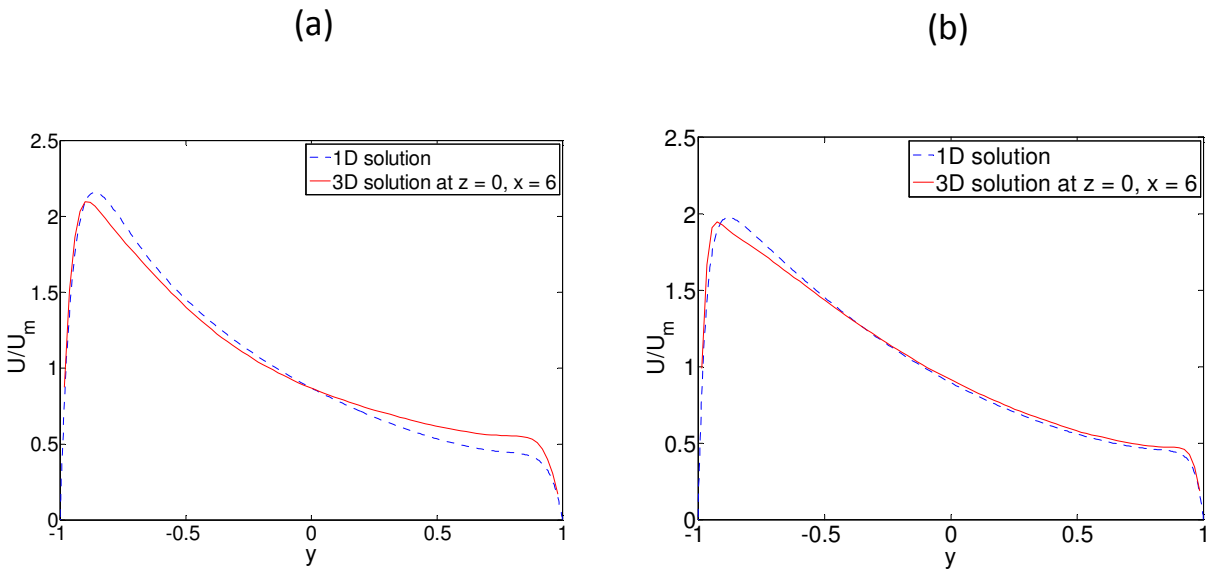

Fig 5.3: Comparison between the 1D and 3D solutions for the upward flows at Re = 5000, Gr = 10^8: (a) Ha = 400, (b) Ha = 1000.

The 3D results are shown in Fig 5.1. Regardless of the forced flow direction, both the flow and the temperature field have a tendency to two-dimensionalization as the Hartmann number is increased. In the case of upward flows at Re= 5000 and Gr =10^7 the flow becomes visually two-dimensional at Ha~100, while two-dimensionalization of the temperature field is accomplished at higher Ha of about 400. The downward flows demonstrate the same tendency to two-dimensionalization with the Hartmann number. The effects due to the flow development can be seen in Fig 5.2, which shows the velocity and temperature fields at the duct midplane z=0. At some locations, these effects manifest themselves in the form of high-velocity jets; at others, in the form of stagnant, recirculation or even reverse flows causing "hot spots" at the interface. A distinctive reverse flow near the "hot wall" and an associated hot spot can be seen in the case of downward, buoyancy-opposed flows at Ha=1000 (Fig 5.2d). In both cases, there is a well-

established fully developed flow in the middle section of the poloidal duct. The flow development effects are reduced and the proportion of the duct that is fully developed increases as the Hartmann number increases. In the case of downward flows, the formation of a fully developed flow seems to occur at higher Ha. The formation of relatively long zones where the flow is nearly fully developed allows for a simpler analysis based on the 2D and even 1D models. The analytical solution for the fully developed solution is provided in section 4.3. Fig 5.3 shows a comparison between the velocity profiles from the 1D approach with the 3D results. The good match between the velocity profiles shows that the Q2D assumption used for 1D analytical solution is valid.

Fig 5.4 shows the variation of axial velocity and temperature on a plane parallel to magnetic field for the upward flow case with $Re = 5000, Gr = 10^7$ at various Ha. The two-dimensionalization of the velocity and temperature fields with increasing Ha is evident from these contour plots. The velocity field appears to reach a Q2D state for $Ha > 200$. Therefore, use of any 2D model to study these kind of flows in this parameter range is justified if $Ha > 200$. The temperature field, on the other hand approaches the Q2D state at $Ha > 400$. For the case of pure natural convection with differential heating it was observed that the temperature field attains a Q2D state for $Ha \geq 200$ [22]. The deviation from this value can be explained by the insulating nature of the walls considered in the present case. The velocity and temperature fields in the downward flow also exhibit the same tendency towards two-dimensionalization.

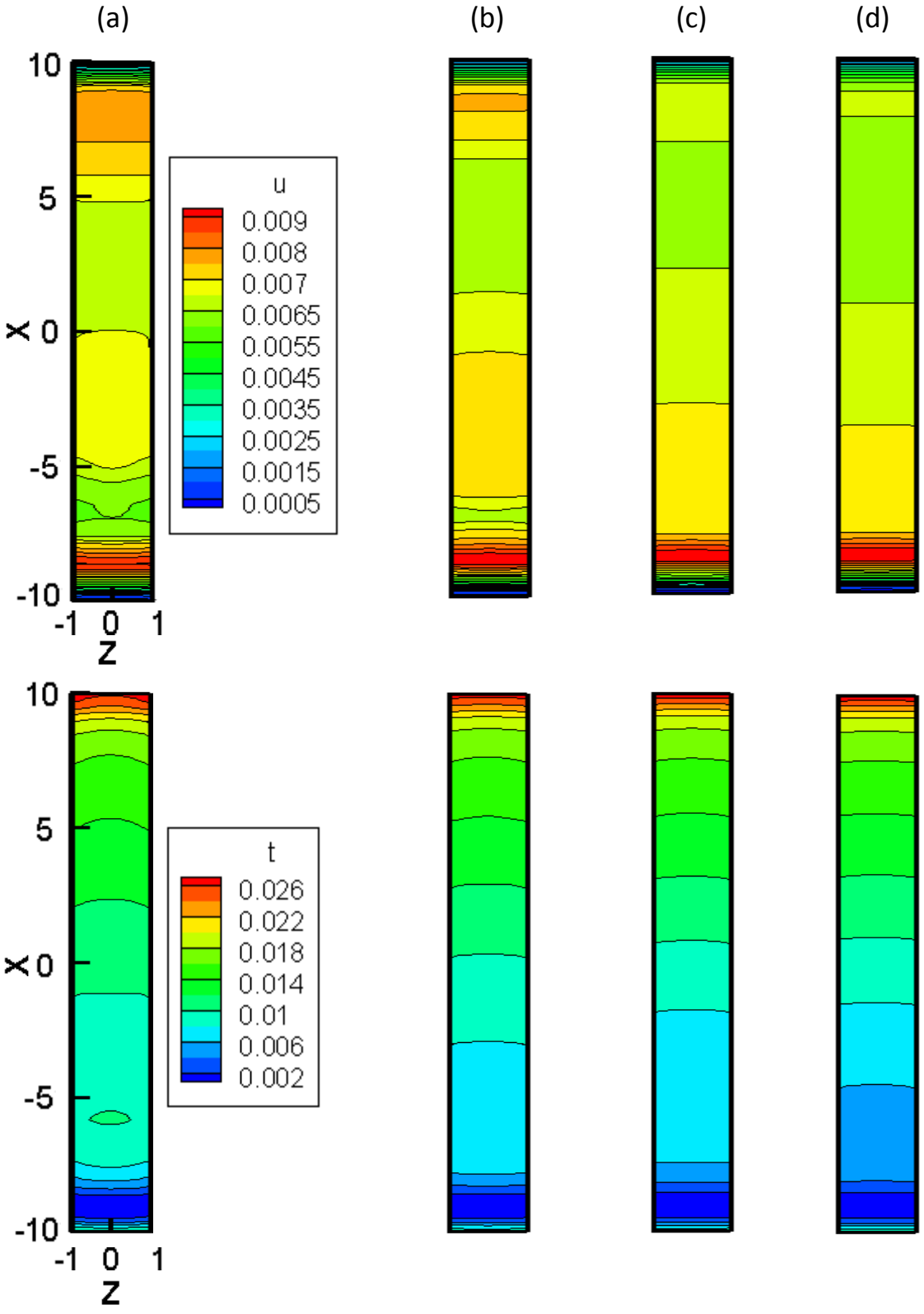

Fig 5.4: Contours of axial velocity (upper) and temperature (lower) at the plane $y = 0$ (plane parallel to the magnetic field), for the case of upward flow at $Re = 5000$, $Gr = 10^7$: (a) $Ha = 100$, (b) $Ha = 200$, (c) $Ha = 300$, (d) $Ha = 400$.

5.4 Perspectives

Understanding the flow behavior in the poloidal ducts is a critical step in the blanket design. This knowledge is essential to further understanding various phenomena such as heat losses to He, tritium transport through the liquid metal, thermal design of the FCI and corrosion of the duct walls, which collectively determine the blanket performance. Based on our analysis of liquid metal flow instabilities and mixed convection flow in a prototype blanket, here we try to predict the conditions in real blanket environment.

Using the linear stability analysis, we obtained an expression for Ha_{cr} as a function of Re and Gr which is given by Eq. 4.24. For Re = 20,000 a simple extrapolation of the critical values at Gr = 7 x 10^9 and 2 x 10^{12} yields Ha_{cr} = 1238 and 3923 respectively. Based on this, it can be predicted that the flow in the front ducts (see Fig. 1 .1) under ITER conditions is hydrodynamically stable and stays laminar far away from the entry and exit. As pointed out earlier Eq. 4.24 is applicable for 5000 < Re < 20,000 and Gr from 10^6 to 10^9. Therefore, the current extrapolation gives a rational estimate of the critical values under ITER conditions but may not be reasonable for DEMO conditions where Gr is three orders of magnitude larger. In addition, for ordinary hydrodynamic cases linear stability analysis is known to over predict the critical values for internal flows as compared to those observed in experiments. Taking into account all these facts, the flow in the front ducts under DEMO conditions can be hydrodynamically unstable and assume a Q2D turbulent state. The downward flows on the other hand can be turbulent and Q2D under both ITER and DEMO conditions. The numerical and experimental study to understand heat transfer in MHD buoyant flows in vertical channels with differential heating revealed that there is a 15-20% increase in the Nusselt number once the flow

transitions from a three dimensional to a two-dimensional state [22]. The increase in Nusselt number shows that the two-dimensional flow transfers heat more efficiently than the three dimensional flow. Therefore, Q2D flows in the blanket will improve the blanket performance.

In the real blanket flows, it was suggested that the liquid metal should flow upward in the front ducts and downward in the return ducts [80]. Present 3D simulations of the flow in a prototype blanket revealed that there are regions of stagnant and reverse flows (see Fig. 5.2) due to the buoyancy, entry and exit effects. Particularly in the case of downward flows, where the flow is observed to be unsteady these regions span the entire length of the duct and seem to grow larger with an increase in *Gr*. This is due to the fact that in the downward flows the buoyancy forces are acting opposite to the flow direction. These regions cause "hot spots" in the flow path and also trap tritium making its extraction more complex, this is a concern for the blanket design. As the volumetric heat generation decays exponentially in the radial direction (Fig 1.3), the buoyancy forces are larger in the front ducts as compared to the return ducts. To minimize the effects of reverse flows and stagnant regions on the blanket performance we reemphasize the suggestion made earlier that the forced flow should be directed upward in the front ducts and downward in the return ducts.

CHAPTER 6

Conclusions and future studies

6.1 MHD flows with M shaped velocity distribution

As discussed in chapter 3, the suggested model predicts many flow features observed in earlier experimental studies and also in recent 3D DNS for MHD flows with potentially unstable M-shaped velocity profiles, whose dynamics is essentially Q2D. Among these features are: two instability types associated with either bulk-side or wall-side of the near-wall jet, jump in the kinetic energy by orders of magnitude once the Reynolds number exceeds its critical value, *etc*. Under certain conditions, the near-wall jet becomes unstable and the whole flow transients to a turbulent state. As predicted with the present linear stability analysis, the dominating instability mechanism is the Kelvin-Helmholtz instability associated with the inflection point in the bulk-side leg of the jet. However, when the jet is weak enough, another instability type, the side-layer instability, associated with the wall-side leg of the jet and the growth of Tollmien–Schlichting waves can also be predicted. The side-layer instability typically occurs at much higher Reynolds numbers and exhibit longer wavelengths compared to the inflectional instability. In some range of the flow parameters, the linear theory also predicts a mixed instability mode when inflectional and side-layer instabilities can coexist. The nonlinear computations also point to flow instabilities and laminar-turbulent transitions but the nonlinear results are significantly different from the linear predictions.

The linear flow behavior can nevertheless be observed in full numerical computations either at relatively low Reynolds numbers, when nonlinear mechanisms don't develop, or at higher *Re* during the first flow development stages, when the flow perturbations are still small in amplitude. In these linear regimes, the bulk shear layers break down forming two rows of isolated vortices but all disturbances remain localized in the vicinities of the original shear layers. In the non-linear saturation phase, the perturbed flow structure becomes much more complex. Upon reaching this phase, two sorts of vortices are present: the primary vortices formed from the bulk-side shear layers and secondary vortices owing to detachment of the boundary layers from the wall. The associated vortical flow structure in the near-wall region, originally occupied by the jet, has a wavelength of several times larger than the wavelength of the most amplified instability mode predicted by the linear theory. Although the nonlinear flow demonstrates near-periodic behavior both in time and space, the whole flow domain is densely populated with many vortices of different sizes and opposite spin resulting in a chaotic, turbulent, flow. Detailed analysis of the flow snapshots has revealed the most important non-linear mechanisms that involve various vortex-wall and vortex-vortex interactions. The vortex-vortex interactions are typical to Q2D turbulent flows as required by the inverse energy cascade. Once two or more vortices of the same sign are brought together, they form a bigger compound vortical structure. Such interactions can occur between primary vortices, secondary vortices or between primary and secondary vortices. Of them, primary-primary vortex interactions in the bulk-side leg of the near-wall jet (that mostly occur in the form of vortex pairing) seem to have the strongest effect on the formation of a new wavelength. The vortex-wall interactions involve destabilization of the near-wall liquid when a single primary vortex or a group of vortices move downstream. Such interaction includes a few typical stages: local concentration of the vorticity

field within the boundary layer, formation of rapidly-rising thin spires of fluid, their interactions with the external flow, rolling up, and finally formation of new vortices that can travel far from their original location. This near-wall interactions result in a special effect of negative turbulence production, which also indicates that the eddy viscosity, defined in a standard way as the ratio between the Reynolds stress and the mean velocity gradient, is negative, unlike many 3D turbulent flows, where the eddy-viscosity concept is applicable.

The fact of negative eddy viscosity brings a practical question: to what degree eddy-viscosity based turbulence models can be applicable to this sort of turbulent flows? As shown in the recent past [81], a specially adjusted one-equation model can predict well Q2D turbulent flows in the MATUR experiment. In this experiment, however, the internal electrodes and thus the inflection point are located far enough from the wall such that the vortex-wall interactions are not essential. As shown here, vortex-wall interactions in the reference flow are not negligible even in the cases when the original bulk shear layer is far from the wall (*e.g.* when L=0.075). Therefore different types of turbulence models, beyond the Boussinesq approximation, may be needed.

In conclusion, we should mention that the obtained results along with other results for MHD flows in previous studies cited throughout this work give a better look into what is called “jet instability”. This instability cannot be considered as a single phenomenon but, in fact, it is an integrated phenomenon that involves different instability types and various mechanisms both linear and non-linear. It is remarkable that all these features can be predicted with a relatively simple Q2D model rather than using costly 3D DNS studies.

6.2 MHD flows with buoyancy forces

The linear theory predicts two instability modes: the bulk (inflectional) instability and the side-wall boundary layer instability. The instabilities mostly occur at the hot wall but in some cases also at the cold one. The instability mode is strongly dependent on the shape of the basic velocity profile, which can be characterized by parameters *D* and/or *r* introduced in Section III based on the analytical solution for the unperturbed flow. The side-wall boundary layer instability is more typical to high Reynolds number flows, where the basic velocity profile is just slightly distorted by the buoyancy forces. The observed instability is similar to the instability of the Shercliff layer in purely MHD flows. The bulk instability is more typical to MHD mixed-convection flows at relatively low Reynolds and high Grashof numbers such that the basic velocity profile demonstrates a high velocity jet near the hot wall and two or more inflection points. Typically, the bulk instability has a higher amplification rate than the side-wall instability (one order of magnitude higher) and smaller wavenumbers. In some cases, the linear theory suggests two instability modes can appear simultaneously. The bulk instability seems to be the most dominant linear instability type in the conditions of a fusion blanket. An important result from the linear stability analysis is Eq.4.24, which allows for predicting a critical Hartmann number as a function of *Gr* and *Re*, above which the flow is linearly stable. Notice that applicability of this equation is not guaranteed far beyond the parameter range introduced in Section 4.4.

The nonlinear DNS-type computations allowed for the turbulent flow analysis. Upon reaching the nonlinear saturation phase in time, the flow demonstrates features typical to Q2D turbulence. Depending on *Re*, *Ha* and *Gr* numbers, two characteristic turbulence regimes have been identified: (i) weak and (ii) strong turbulence. In the weak-turbulence regime, the vortices are

mostly formed from the original shear layer in the bulk flow near the hot wall. They remain localized in the same near-wall area where the basic velocity profile has an inflection point. Some vortex-wall interactions are clearly seen but the boundary layer remains weakly disturbed. In the strong-turbulence regime, the two characteristic features are intensive vortex-vortex and vortex-wall interactions. The vortex-wall interactions cause the boundary layer destabilization and eventually its detachment from the wall at several locations along the flow path. The detached boundary layer and its interaction with the outer flow stimulate further formation of secondary vortices, which can travel across the whole flow reaching the opposite wall. The vortex-vortex interactions occur between various vortices, including primarily bulk vortices and secondary vortices in the form of paring vortices of the opposite sign and merging two or more vortices of the same sign into a bigger compound vortex structure, comparable in size with the duct size. The transition from weak to strong turbulence can be characterized by the threshold kinetic energy [Eq. 4.25] of 2×10^{-2}.

The observed two turbulence regimes seem to be similar to two instability types previously observed in other studies of MHD flows with the inflectional basic velocity profile, including Refs. [19, 40-42, 76]. This suggests that the inflectional instability followed by the vortex-wall interactions are the two principal mechanisms in this type of MHD flow. However, the case of the mixed-convection flows demonstrates some differences from other studies, mostly due to a strong asymmetry in the velocity profile caused by the buoyancy forces and due to close proximity of the inflection point to the wall. This difference can be seen, for example, in the changes of the kinetic energy once one of the parameters associated with unstable behavior, either Reynolds or Grashof number, is increased. Even in a weak turbulence regime the perturbed flows seem to demonstrate non-linear behavior. In previous studies (Refs. [19, 40-42,

76]) the transition from one to another instability type occurred as a jump in the kinetic energy once the Reynolds number reached a critical value. This doesn't happen in the reference case, where the kinetic energy demonstrates sharp but continues changes.

6.3 Flow in a DCLL prototype

3D numerical modeling of liquid metal flow in the DCLL geometry using HIMAG revealed that as the Hartmann number is increased the flow shows a tendency towards two dimensionalization. Compared with the velocity field, the temperature field attainted a two dimensional state at relatively higher Hartmann numbers. The matching between the fully developed velocity profiles at the mid plane and the 1D solution shows that the Q2D assumption is valid. For the parameter range considered in the simulations, it was observed that the velocity field reaches a Q2D state for $Ha > 200$. Whereas the temperature field reaches a Q2D state for $Ha \geq 400$. This difference needs further explanation. Based on linear stability analysis, 2D and 3D simulations it is predicted that the upward flows in ITER conditions can be laminar, whereas they can be Q2D and turbulent in DEMO conditions. The downward flows on the other hand are predicted to be turbulent and need further understanding.

6.4 Recommendations for future research

As a first step in understanding the poloidal flows under blanket conditions, in this research we addressed various instability and transition mechanisms possible in these flows. We also performed 3D numerical simulations in a prototype DCLL geometry to get some fundamental

understanding of the flows in real blanket conditions. The task of completely understanding the flows under real blanket conditions was not fully completed by this work. However, this research should serve as an excellent starting point for any theoretical, numerical and experimental studies to further understand MHD duct flows in general and blanket flows in particular.

The parametric model considered in chapter 2 can serve as a mathematical description for a duct flow with embedded wall electrodes. To our best knowledge only one experiment, MATUR [66], has been done for this type of MHD flows, but the MATUR data are not comparable with our results because the experiment were done in a cylindrical cell. So far the model was validated against the available numerical studies of liquid metal flow in ducts only. It was also demonstrated that the instability and transition mechanisms observed in our model problem and buoyancy flows are similar. Therefore, an experiment based on the present model has been planned to attain further understanding of the flow dynamics. This experiment can be used to validate the model and at the same time study the effect of the location of the inflection point on the stability of the flow.

Linear stability analysis is known to over predict the critical values for internal flows. To further understand the instability mechanisms there is a need to extend the stability analysis to modal and energy stability studies. Linear stability gives an upper bound for the critical values above which any infinitesimal perturbation will grow in time, whereas energy stability gives a lower bound for the critical values below which the energy of any perturbation decay monotonically [82]. For the stability of side layers these bounds are given as $Re_{\mathrm{L}} = 48350\ Ha^{1/2}$ and $Re_{\mathrm{E}} = 65.3288\ Ha^{1/2}$. Where Re_L and Re_E are the critical values based on linear and energy stability analyses. For values of Re between those two stability bounds, Q2D perturbations

undergo some significant transient growth. A similar study has to be carried out for the case of buoyancy flows to get further understanding of the instability thresholds.

The interfacial slip has recently been identified as an important phenomenon in the duct flows of the DCLL blanket [83]. Recent experimental studies [84, 85] also suggest that slip phenomenon between the flowing liquid metal and the SiC insert in the blanket will likely occur. The classic "SM82" model for quasi-two-dimensional MHD flows is also modified to take into account the slip effect and it is observed that the flow demonstrates more irregular behavior as the slip length increases. A recent study [86] of the effect of slip on the stability of Hartmann flow demonstrated that the increase in slip length significantly increases the critical Reynolds number thus stabilizing the flow. The stability analysis for the buoyancy flows has to be extended by considering this hydrodynamic slip effect in order to emulate the blanket conditions.

The 3D numerical simulations of the liquid metal flow in DCLL geometry have to be carried out considering the thermal and electrical conductivity of the walls, poor wetting conditions between the liquid metal and the duct walls and heat losses to He. The code HIMAG at its present stage can only reach $Gr \sim 10^8$. Due to the small values of Gr the temperature gradient in the poloidal direction is negligible as compared to the radial direction. However, in the DEMO conditions ($Gr \sim 10^{12}$), this gradient in temperature in the poloidal direction can be substantial. An appropriate discretization and/or numerical technique have to be implemented to reach higher values of Gr and at the same time capture the small scale interactions.

APPENDIX A

Analytical solution for the basic flow

To derive an analytical solution for the basic flow $\mathbf{V}_0(U_0,0,0)$, the unsteady and convective terms in the momentum equation (3.2) are dropped, and then the equation is rewritten in another dimensionless form. The linear scale is still the duct dimension *a*, while the new velocity scale is defined through the pressure gradient as $\left(-\frac{dp}{dx}\right)\frac{a^2}{\rho v}$. The new equation is solved separately in the inner and outer domains. In the outer domain ($L < y < 1$), the equation takes the following form:

$$0 = \frac{d^2U_{01}}{dy^2} - MU_{01} + 1, \tag{A1}$$

where $M = Ha\left(\frac{a}{b}\right)^2$ is the modified Hartmann number. The solution satisfying the no-slip condition at the duct wall y = 1 is

$$U_{01} = \frac{1 - e^{\sqrt{M}(y-1)}}{M} + A\left(e^{-\sqrt{M}y} - e^{\sqrt{M}(y-2)}\right), \tag{A2}$$

where A is the integration constant. In the inner domain ($0 < y < L$),

$$0 = \frac{d^2 U_{02}}{dy^2} - M U_{02} + 1 - F, \tag{A3}$$

where $F = F_0 \Big/ \left(-\frac{1}{\rho}\frac{dP}{dx} \right)$. The solution satisfying the symmetry boundary condition at the duct centerline is

$$U_{02} = \frac{1-F}{M} + 2B + B\left(e^{-\sqrt{M}y} + e^{\sqrt{M}y} - 2 \right), \tag{A4}$$

The two integration constants A and B are found by matching solutions U_{01} and U_{02} at the inflection point $y = L$, which requires $U_{01} = U_{02}$ and $\frac{dU_{01}}{dy} = \frac{dU_{02}}{dy}$, as follows:

$$A = \frac{2e^{(-1+L)\sqrt{M}} - F\left(1 - e^{2L\sqrt{M}}\right)}{2\left(e^{(-2+L)\sqrt{M}} + e^{L\sqrt{M}}\right)M}, \quad B = \frac{-2e^{(-1+L)\sqrt{M}} + F\left(1 + e^{2\sqrt{M}(L-1)}\right)}{2\left(e^{(-2+L)\sqrt{M}} + e^{L\sqrt{M}}\right)M}. \tag{A5}$$

From the obtained solution, the thickness δ of the internal shear layer associated with the inflection point in the velocity profile is

$$\delta = \frac{2}{\sqrt{M}} \frac{e^{2L\sqrt{M}} - 1}{e^{2L\sqrt{M}} + 1}. \tag{A6}$$

REFERENCES

1) S. Smolentsev, R. Moreau, M. Abdou, Characterization of key magnetohydrodynamic phenomena in PbLi flows for the US DCLL blanket. *Fusion Eng. Des.* 83(5-6): 771-783, 2008.

2) L. Bühler, Liquid metal magnetohydrodynamics for fusion blankets, in: S. Molokov, R. Moreau, H. K. Moffat (eds.), *Magnetohydrodynamics: Historical Evolution and Trends*, Springer, 171-194, 2007.

3) G. Rampal, A. Li Puma, Y. Poitevin, E. Rigal, J. Szczepanski, C. Boudot, HCLL TBM for ITER-design studies. *Fusion Eng. Des.* 75-79: 917-922, 2005.

4) S. Malang, E. Bojarsky, L. Bühler, H. Deckers, U. Fischer, P. Norajitra, H. Reisser, Dual coolant liquid metal breeder blanket, in: Proceedings of the 17th Symposium on Fusion Technology, Rome, Italy, Spetember 14-18: 1424-1428, 1992.

5) D. L. Smith, C.C. Baker, D. K. Sze, G.D. Morgan, M. A. Abdou, S. J. Piet, S. R. Schultz, R. W. Moir, J. D. Gordon, Overview of the blanket comparison and selection study. *Fusion Technol.* 8(1): 10-113, 1985.

6) S. Molokov, R. Moreau, H. K. Moffat (eds.) *Magnetohydrodynamics: Historical Evolution and Trends*, Springer, 2007.

7) J. Reimann, G. Benamati, R. Moreau, MHD issues of the European self-cooled and water-cooled 83Pb-17Li blankets, in C. Varandas and F. Serra (eds). *Fusion Technology.* 1527, 1996.

8) I. R. Kirillov, C. B. Reed, L. Barleon, K. Miyazaki, present understanding of MHD and heat transfer phenomena for liquid metal blankets. *Fusion Eng. Des.* 27: 553-569, 1995.

9) N. Morely, S. Smolentsev, L. Barleon, I. Kirillov, M. Takahashi, Liquid magnetohydrodynamics- recent progress and future directions for fusion. *Fusion Eng. Des.* 51-52: 701-713, 2000.

10) N. Morley, S. Malang, I. Kirillov, Thermofluid magnetohydrodynamics issues for liquid breeders. *Fusion Sci. Technol.* 47: 488-501, 2005.

11) D. K. Sze, M. Tillack, L. El-Guebaly, Blanket systems selection for the ARIES-ST. *Fusion Eng. Des.* 48: 371-378, 2000.

12) C. P. C. Wong, S. Malang, M. Sawan, M. Dagher, S. Smolentsev, B. Merrill, M. Youssef, S. Reyes, D. K. Sze, N. B. Morely, S. Sharafat, P. Calderoni, G. Sviatoslavsky, R. Kurtz, P. Fogatry, S. Zinkle, M. Abdou, An overview of dual coolant Pb-17Li breeder first wall and blanket concept development for the US ITER-TBM design. *Fusion Eng. Des.* 81: 461-467, 2006.

13) C. P. C. Wong, S. Malang, M. Sawan, S. Smolentsev, S. Majumdar, B. Merrill, D. K. Sze, N. Morely, S. Sharafat, M. Dagher, P. Peterson, H. Zhao, S. J. Zinkle, M. Abdou, M. Youssef, Assessment of first wall and blanket options with the use of liquid breeder. *Fusion Sci. Technol.* 47: 502-509, 2005.

14) ARIES Team, M. S. Tillack, X. R. Wang, J. Pulsifer, S. Malamng, D. K. Sze, ARIES-ST breeding blanket design and analysis. *Fusion Eng. Des.* 49/50: 689-695, 2000.

15) S. Smolentsev, N. B. Morley, M. Abdou, MHD and thermal issues of the SiC_f/SiC flow channel insert. *Fusion Sci. Technol.* 50: 107-119, 2006.

16) H. Branover, *Magnetohydrodynamic Flows in Ducts*, Wiley, New York, 1978.

17) R. G. Lingwood, T. Alboussière, On the stability of the Hartmann layers. *Phys. Of Fluids* 11: 2058-2068, 1999.

18) J. Sommeria, R. Moreau, Why, How and When MHD Turbulence Becomes Two Dimensional?' *J. Fluid Mech*. 118: 507, 1982.

19) U. Bürr, L. Barleon, U. Müller, A. B. Tsinober, Turbulent transport of momentum and heat in magnetohydrodynamic rectangular duct flow with strong side wall jets. *J. Fluid. Mech.* 406: 247-279, 2000.

20) S. Smolentsev, R. Moreau. Modeling quasi-two-dimensional turbulence in MHD duct flows, in: proceedings of 7th international pamir conference on fundamental and applied MHD, Pesqu'Île de Giens, France: 857-861, 2008.

21) T. Tagawa, G. Authié, R. Moreau, Buoyant flow in long vertical enclosures in the presence of a strong horizontal magnetic field. Part 1. Fully-established flow. *Europ. J. Mech.* B 21: 383-398, 2002.

22) G. Authié, T. Tagawa, R. Moreau, Buoyant flow in long vertical enclosures in the presence of a strong horizontal magnetic field. Part 2. Finite enclosures. *Europ. J. Mech.* B 22: 203-220, 2003.

23) Ivan Di Piazza, Michele Ciofalo, MHD free convection in a liquid-metal filled cubic enclosure. I. Differential heating. *Int. J. heat and mass transfer*, 45: 1477-1492, 2002.

24) Ivan Di Piazza, Michele Ciofalo, MHD free convection in a liquid-metal filled cubic enclosure. I. Internal heating. *Int. J. heat and mass transfer*, 45: 1493-1511, 2002.

25) U. Burr, U. Müller, Rayleigh-Bénard convection in liquid metal layers under the influence of a vertical magnetic field. *Phy. Fluid.* 13(11): 3247-3257, 2001.

26) T. Alboussière, J. P. Garandet, R. Moreau, buoyancy-driven convection with a uniform magnetic field. Part 1. asymptotic analyisis. *J. Fluid Mech*. 253: 545-563, 1993.

27) L .Davoust, M. D. Cowley, R.Moreau, R. Bolcato, buoyancy-driven convection with a uniform magnetic field. Part 2. experimental investigation. *J. Fluid Mech*. 400: 59-90, 1999.

28) C. Karcher, Y. Kolesnikov, O. Andreev, A. Thess, Natural convection in a liquid metal heated from above and influenced by a magnetic field. *Eur. J. Mech. B/Fluids* 21: 75-90, 2002.

29) M. Takashima, The stability of natural convection in vertical layer of electrically conducting fluid in the presence of a transverse magnetic field. *Fluid Dyn. Res*. 14: 121, 1994.

30) L. Bühler, Laminar buoyant magnetohydrodynamic flow in vertical rectangular ducts. *Phys. Fluids*. 10(1): 223-236, 1998.

31) S. Smolentsev, R. Moreau, M. Abdou, Study of MHD Mixed Convection in the DCLL Blanket Conditions, 7th PAMIR Conference on Fundamental and Applied MHD, Giens, France, September 8-12, 2008.

32) E. Blums, Yu. Mikhailov, R. Ozols, *Heat and Mass Transfer in MHD Flows*, World Scientific, Singapore, 1987.

33) A. Pothérat, Quasi-two-dimensional perturbations in duct flows under transverse magnetic field. *Phys. Fluids*. 19: 074104, 2007.

34) T. L. Doligalski, C. R. Smith, J. D. A. Walker, Vortex interaction with walls. *Annu. Rev. Fluid Mech*. 26 (1994), 573-616.

35) Yen-Cho Chen, J. N. Chung, "The linear stability of mixed convection in a vertical channel flow", *J. Fluid Mech.* 325: 29, 1996.

36) U. Müller, L. Bühler, *Magnetohydrodynamics in Channels and Containers*, Springer, Berlin, 2001.

37) R. Moreau, *Magnetohydrodyanmics*, Kluwer, 1990.

38) L. Bühler, Instabilities in quasi-two-dimensional magnetohydrodynamic flows. *J. Fluid Mech.* 326: 125, 1996.

39) Y. B. Kolesnikov, Two-dimensional turbulent flow in a channel with inhomogeneous electrical conductivity of the walls. *Magnetohydrodynamics* 8: 308, 1972.

40) L. Bühler and S. Horanyi, Measurements of time-dependent liquid-metal magnetohydrodynamic flows in a flat rectangular duct. *Fusion Eng. Des.* 84: 518, 2009.

41) C. B. Reed and B. F. Picologlou, Sidewall flow instabilities in liquid metal MHD flows under blanket relevant conditions. *Fusion Tech.* 15: 705, 1989.

42) M. Kinet, B. Knaepen, and S. Molokov, Instabilities and transition in magnetohydrodynamic flows in ducts with electrically conducting walls. *Phys. Rev. Lett.* 103: 154501 (2009).

43) K. Fajimura, *Stability of MHD Flow Through a Square Duct.* UCLA-FNT-023, 1989.

44) A. L. Ting, J. S. Walker, T. J. Moon, C. B. Reed, and B. F. Picologlou, Linear stability analysis for high-velocity boundary layers in liquid-metal magnetohydrodynamic flows. *Int. J. Engng. Sci.* 29: 939, 1991.

45) J. Priede, S. Aleksandrova, and S. Molokov, Linear stability of Hunt's flow. *J. Fluid Mech.* 649: 115, 2010.

46) J. C. R. Hunt, Magnetohydrodynamic flow in rectangular ducts. *J. Fluid Mech.* 21: 577, 1965.

47) Yu. M. Gelfgat, V. S. Dorofeev, and E. V. Scherbinin, Experimental investigation of the velocity structure of an MHD flow in a rectangular channel. *Magnetohydrodynamics* 7: 26, 1971.

48) Y. B. Kolesnikov and A. B. Tsinober, Magnetohydrodynamic flow in the region of a jump in the conductivity at the wall. *Magnetohydrodynamics* 8: 70, 1972.

49) U. Burr, L. Barleon, U. Müller, and A. Tsinober, Turbulent transport of momentum and heat in magnetohydrodynamic rectangular duct flow with strong sidewall jets. *J. Fluid Mech.* 406: 247, 2000.

50) M. S. Narula, Experiments and numerical modeling of fast flowing liquid metal thin films under spatially varying magnetic field conditions, PhD thesis report, UCLA, 2008.

51) M. A. Abdou, et. al., On the exploration of innovative concepts for fusion chamber technology, *Fusion Eng. And Des.* 54-2: 181-247, 2001.

52) P. A. Davidson, An introduction to magnetohydrodynamics. Cambridge university press, 2001.

53) J. C. Tannehill, D. A. Anderson, and R. H. Pletcher, *Computational Fluid Mechanics and Heat Transfer,* Taylor & Francis, 1997.

54) A. Krawczyk, J. A. Tegopoulos, *Numerical modeling of eddy currents*, Clarendon press Oxford, 1993.

55) M. J. Ni, R. Munipalli, N. B. Morley, P. Huang, M. A. Abdou, Consistent and conservative schemes for incompressible MHD flow at a low magnetic Reynolds number, Part I: On a rectangular collocated grid system, *Journal of Comp. Phy.*, 227-1: 174, 2007.

56) M. J. Ni, R. Munipalli, N. B. Morley, P. Huang, M. A. Abdou, Consistent and conservative schemes for incompressible MHD flow at a low magnetic Reynolds number, Part II: On an arbitrary collocated grid system, *Journal of Comp. Phy.*, 227-1: 205, 2007.

57) I. V. Lavrent'ev, S. Yu. Molokov, S. I. Sidorenkov, A. R. Shishko, Stokes flow in a rectangular magnetohydrodynamic channel with non conducting walls within a non uniform magnetic field at large Hartmann numbers. *Magnetohydrodynamics,* 26: 328, 1990.

58) S. Smolentsev, Averaged model in MHD duct flow calculations. *Magnetohydrodynamics,* 33: 42, 1997.

59) S. Cuevas, S. Smolentsev, M. Abdou, On the flow past a magnetic Obstacle. *J. Fluid Mech.* 553: 227, 2006.

60) D. Krasnov, O. Zikanov, M. Rossi and T.. Boeck, Optimal linear growth in magnetohydrodynamic duct flow. *J. Fluid Mech.* 653: 273, 2010.

61) A. Pothérat, J. Sommeria, and R. Moreau, Numerical simulations of an effective two-dimensional model for flows with a transverse magnetic field. *J. Fluid Mech.* 534: 115, 2005.

62) R. Klein and A. Pothérat, Appearance of three dimensionality in wall-bounded MHD flows. *Phys. Rev. Lett.* 104: 034502, 2010.

63) A. Thess and O. Zikanov, Transition from two-dimensional to three-dimensional MHD turbulence. *J. Fluid Mech.* 579: 383, 2007.

64) R. Moreau, S. Smolentsev, and S. Cuevas, MHD flow in an insulating rectangular duct under a non-uniform magnetic field. *PMC Physics B*, 3, 2010.

65) T. N. Aitov, A. B. Ivanov, and A. V. Tananaev, Flow of liquid metal in a chute in a coplanar magnetic field. *Magnetohydrodynamics*, 23: 78, 1987.

66) K. Messadek and R. Moreau, An experimental investigation of MHD quasi-two-dimensional turbulent shear flows. *J. Fluid Mech.* 456: 137, 2002.

67) S. Smolentsev, N. Morely, and M. Abdou, Code development for analysis of MHD pressure drop reduction in a liquid metal blanket using insulation technique based on a fully developed flow model. *Fusion Eng. Des.* 73:83, 2005.

68) W. Huang and D. M. Sloan, The pseudospectral method for solving differential eigenvalue problems. J. Comput. Phys. 111: 399, 1994.

69) S. A. Orszag, Accurate solution of the Orr-Sommerfeld stability equation. *J. Fluid Mech.* 50: 689, 1971.

70) R. C. Lock, The stability of the flow of an electrically conducting fluid between parallel planes under a transverse magnetic field. *Proc. R. Soc. London*. Ser. A 233: 105, 1955.

71) A. Tsinober, *An Informal Introduction to Turbulence,* Kluwer, 2001.

72) A. Arakawa, Computational design for long-term numerical integration of the equations of fluid motion: Two-dimensional incompressible flow. Part I. *J. Comput. Phys.* 1: 119, 1966.

73) P. Moresco and T. Alboussière, Experimental study of the instability of the Hartmann layer. *J. Fluid Mech.* 504: 167, 2004.

74) S. Smolentsev, N. Vetcha, R. Moreau, MHD mixed convection in a rectangular duct: 3D, 2D and 1D solutions, Proc. 8th Int. PAMIR Conference on "Fundamental and Applied MHD," Borgo, Corsica, France, Sept. 5-9, 2011, p. 79.

75) S. Wolfram, Mathematica. A System for Doing Mathematics by Computer, 2d edition, 1991.

76) S. Smolentsev, N. Vetcha, R. Moreau, Study of instabilities and transitions for a family of quasi-two-dimensional magnetohydrodynamic flows based on a parametrical model, Phys. Fluids 24: 024101, 2012.

77) L. N. Trefethen, A. E. Trefethen, S. C. Reddy, and T. A. Driscoll, Hydrodynamic stability without eigenvalues, *Science* 261: 578, 1993.

78) V. Shankar, CFD-based higher order methods for broad band parallel applications in computational electromagnetic (CEM), ICCFD2, proceedings of the second international conference on CFD, Sydney, Australia, July 2002.

79) R, Munipalli, V. Shankar, Development of computational capabilities in real gas MHD simulations, AIAA paper 2001-0198, Presented at the 39th AIAA Aerospace Sciences Meeting and Exhibit, Reno, NV, January 2001.

80) S. Smolentsev, and R. Moreau, One equation model for quasi-two-dimensional turbulent magnetohydrodynamic flows, Phys. Fluids 19: 078101, 2007.

81) S. Smolentsev, and R. Moreau, One equation model for quasi-two-dimensional turbulent magnetohydrodynamic flows, *Phys. Fluids* 19: 078101, 2007.

82) P. G. Drazin, *Hydrodynamic stability*, Cambridge university press, 1982.

83) S. Smolentsev, MHD duct flows under hydrodynamic "slip" condition. *Theor. Comput. Fluid Dyn.* 23: 557-570, 2009.

84) B. A. Pint, K. L. More, H. M. Meyer, and J. R. Distefano, Recent progress addressing compatability issues relevant to fusion environments. *Fusion Sci. Technol.* 47: 851-855, 2005.

85) N. B. Morley, A. Medina, and M. A. Abdou, Measurements of specific electrical contact resistance between SiC and lead-lithium eutectic alloy, TOFE 18, San Francisco, September 28-October 2 (2008) Book of Abstracts, P2.66.

86) N. Vetcha, S. Smolentsev, and M. A. Abdou, Stability analysis for the Hartmann flow with interfacial slip, *Magnetohydrodyanmics*. 48(1): 3-11, 2012.